Failure of rigid-elastomer interface under complex loading

Pierre-Yves Corbel

COLLEGES SCIENCES
BRETAGNE POUR L'INGENIEUR
LOIRE ET LE NUMERIQUE

ENSTA BRETAGNE

THÈSE DE DOCTORAT DE

L'ECOLE NATIONALE SUPÉRIEURE
DE TECHNIQUES AVANCÉES BRETAGNE

ECOLE DOCTORALE N° 648
Sciences pour l'Ingénieur et le Numérique
Spécialité : Mécanique des Solides, des Matériaux, des Structures et des Surfaces

Par

Pierre-Yves CORBEL

« Rupture d'interface rigide-élastomère sous chargement complexe»

Thèse présentée et soutenue à Brest, le 24 septembre 2024
Unité de recherche : Institut de Recherche Dupuy de Lôme, UMR CNRS 6027, Brest

Rapporteurs avant soutenance :

Julie DIANI	Directrice de Recherche CNRS, LMS, Ecole Polytechnique
Raphael ESTEVEZ	Professeur des Universités, SIMaP, Université de Grenoble Alpes

Composition du Jury :

Président :	Constantino CRETON	Directeur de Recherche CNRS, SIMM, ESPCI
Examinateurs :	Véronique LAZARUS	Professeure de l'ENSTA Paris, IMSIA, ENSTA Paris
	Thierry REY	Docteur Ingénieur, Michelin
Dir. de thèse :	Julien JUMEL	Professeur de l'ENSTA Bretagne, IRDL, ENSTA Bretagne
Co-dir. de thèse :	Yann MARCO	Professeur des Universités, IRDL, ENSTA Bretagne
Encadrant de thèse :	Vincent LE SAUX	Professeur de l'ENSTA Bretagne, IRDL, ENSTA Bretagne

Remerciements

Ces travaux de thèse ont été financés par la Région Bretagne et par l'ENSTA Bretagne, que je remercie. Je tiens à exprimer ma gratitude à ma direction de thèse pour m'avoir permis de travailler sur un sujet aussi riche. Merci à Julien pour m'avoir offert autant de liberté autour du sujet pour explorer plein de pistes. Merci aussi à Armel et Thierry de chez Michelin, sans qui tout cela n'aurait pas été possible, pour leurs riches discussions et leur soutien industriel.

Au sein de l'IRDL à l'ENSTA Bretagne, je remercie l'équipe PTR2 Assemblage Multi-Matériaux pour leur accueil. Un grand merci aux membres de la plateforme d'essai : Frédéric, Raphaël, Cédric, Sébastien et tout particulièrement Éric, Christian et Didier pour la rigolade, de riches discussions (rarement de mécanique!), leurs enseignements et leur grande aide quand j'étais bien dans la mouise. Je pense que ce sera toujours du bricolage en L015, ne m'en voulez pas ! Je remercie beaucoup Nathalie pour sa patience et sa bonne humeur, surtout à l'approche de la soutenance. Je remercie aussi les membres de CMA, en particulier Nicolas, Jean-François et Jean-Louis pour leur accueil et leur conseil pour l'enseignement.

Au sein du SIMM à l'ESPCI, je remercie E. Barthel et M. Ciccotti pour leur confiance sur le projet des fronts de fissure "gondolo", le court séjour dans leur labo et la reprise des travaux de P. Fourton. Un beau travail finalement publié ! Je remercie aussi les doctorants du SIMM pour leur superbe accueil et les bonnes soirées passés ensemble !

Merci au doctorant de l'équipe PTR2 (Imad, Andrea, Gwladys, Tom, Cyril) pour la bonne ambiance et les bonnes soirées en vos compagnies! Également, merci à tous les stagiaires et post-docs qui sont passés par là (Juan Pablo, Jean-Baptiste, Samuel, Joseph, Jonathan, Jihen, Arthur, Korina, Katerina, Guillaume, Chloé, Amaury, Yosra, Dong) qui nous ont bien amusé et fait oublier la grisaille brestoise !

Ensuite, je tiens particulièrement à adresser mes remerciements à :

- Paulo pour tous ces bons moments, en L015, à rigoler en galérant sur ces fichus conditionneurs et cellules d'efforts. J'espère que tu te plairas bien avec ta famille au Brésil !

- Matthias, le grand surfeur de Tronoën, pour toutes ces bonnes sessions et de m'avoir fait tenir pendant la dernière année de thèse. J'espère que tu réussiras à monter ton projet pizza et que tu vas t'améliorer en choix de board !

- Thomas, co-bureau du D116 et maintenant ami. On aura tenu le cap jusqu'au bout et finis cette fichue thèse ! Je te souhaite de plein de réussite et de bonheur pour toi et ta p'tite famille : tu le mérites vraiment.

Je tiens à remercier l'équipe de l'IRDL côté Lorient à l'Université Bretagne Sud et à l'IUT GIM (P. Pilvin, E. Geslain, V. Keryvin, T. Loulou, J.-M. Cadou, C. Besnard...), pour leurs enseignements et encouragements ! À P. Rogeon, que je remercie encore de m'avoir permis d'entrer en stage au labo et de continuer en licence de mécanique, mais malheureusement qui ne m'aura pas vu terminer le doctorat. Je remercie également les enseignants croisés tout au long de ma scolarité qui croient en leurs élèves et qui m'ont finalement bien aiguillé malgré plusieurs sorties de route ! Je remercie aussi tous les collègues et camarades rencontrés durant mes stages, pas prof mais pareil, pour tous ces échanges qui m'ont apporté beaucoup plus qu'ils ne le croient. La thèse n'est pas un long fleuve tranquille, et ce bagage m'aura été bien plus utile que le bagage théorique finalement.

Enfin, je remercie mes amies de longue date ainsi que ma famille pour leur soutien lors de mes retours dans le Morbihan. Et je ne pourrais jamais suffisamment remercier mes parents, Yolande et Yann, pour leur amour, leur soutien et leurs encouragements, qui m'ont permis d'aller aussi loin dans la vie.

Contents

Introduction

The present thesis describes the developments of experimental methodologies to characterize and quantify the dissipated energy during the debonding of an interface between an elastomer and a rigid solid. This problem concerns a wide range of applications in the industry and multiple scientific interests from various domains. Here, the work focuses on the crack growth between a natural rubber reinforced by black carbon and a brass-coated steel wire cord. The metal reinforcement-rubber composite can be found in numerous applications, from car or air plane tires to conveyor belts. To ensure the structural integrity of the system, the adhesion between the reinforcement and the rubber must withstand the loads during the lifetime of the product. Extension of life, environment-friendly processes, and recycling obligations motivate new developments of elastomer material. To support these researches, an adherence test proposed recently by [Kane, 2020] is improved to understand and quantify the different dissipation sources. The objective of the thesis is to propose novel methodologies to characterize the resistance to crack growth of an elastomer-rigid interface.

The first chapter presents in detail the problem of elastomer-rigid fracture, applied to the case of rubber and brass-coated wire. Then, different observations and theories are presented to shed some insights on the dissipation mechanisms during crack growth at an interface between a soft and a rigid solid. Different classical adherence tests are presented, with the studied test in the end, the Rubber Cord Adhesion Inflation Test.

The second chapter presents our approach to the development of the test and organize the different scientific productions around our objective. The subsequent chapters (3 to 6) are reviewed and published articles, occasioning some repetitions and different notations.

The third chapter focuses on the development of metrology based on marker fol-

lowing. The goal is to control the validity of the kinematic predicted by an analytical model and identify the model directly from the experiment. Then, a more pragmatic approach based on a graphical analysis of experimental curves is proposed. The two approaches, based on different measures of the same series of tests, give the same result, proving the robustness of the RCAIT.

The fourth chapter presents a numerical analysis of crack onset and growth during a RCAIT experiment. The specific loading condition needs a numerical development based on cohesive zone modeling to tackle the instability in pressure. The analysis of the result further validates the steady-state crack growth hypothesis and highlights the difference between the strain-stress path during the onset regime and the propagation regime.

The fifth chapter tackles an experimental problem with experimental, analytical, and numerical developments. The friction effect between the specimen and the confinement can modify the crack onset regime in case of poor lubrication. The phenomenon agrees with an analytical model based on Coulomb friction and follows a scaling law with the Coulomb friction coefficient. The lubrication condition does not affect the crack propagation regime, confirmed by the finite element model, thanks to the initial gap between the specimen and the confinement tube.

The sixth chapter extends the RCAIT to mixed mode loading conditions. The analytical framework to compute the dissipated energy is developed and applied to a series of tests. The experiments show a dependence on the mixed load condition and a small numerical study advocates the influence of the macroscopic loading condition on the crack tip morphology.

The seventh chapter aims to inhibit the contribution of the Mullins effect (rate-independent hysteresis found in filled elastomer) from dissipation during interface crack growth. A novel methodology is presented and shows a diminution of the dissipated energy with the increase of softening. A hybrid numerical-analytical model is proposed to predict the interfacial fracture energy dependence on softening.

The eighth chapter presents the creep fracture test to study the interface crack growth at low and very low crack velocities. The evolution of the critical strain energy release rate with the crack velocity could indicate a viscous dissipation.

Finally, the conclusion and perspective of the present work ends the manuscript.

Bibliographic introduction to the problem 1

The first chapter presents the industrial and scientific context of the present work.

1.1 Industrial application

The outstanding properties of rubbers are of great interest in multiple industrial fields. Those materials are often bonded on or in between substrates of different material to create assemblies or composites. Even if the first goal is not structural bonding, the interface between the two materials must be strong enough to ensure interface integrity in normal working conditions throughout the system's entire lifetime.

1.1.1 Cord reinforced rubber composites

Rubber reinforced by cords is a common composite used in the industry for its damping properties, high friction, or high compliance. For instance, the reinforced rubber material can be found in air-spring [Torggler et al., 2023], car tire [Kane, 2020], transmission belt [Valantin, 2014], conveyor belt or piping (example of reinforcement illustrated in fig. 1.1). In the tire, the role of the reinforcement is to enhance the rigidity while keeping the damping properties. It is a balance between good road traction and damping of small road imperfections and fatigue resistance. If the rubber de-bonds from the reinforcement, the structural integrity of the tire is no longer guaranteed. Hence, the rubber-reinforcement adhesion must resist throughout the life of the product, under mechanical loadings and environment (temperature, humidity).

The studied system for this application is carbon black filled natural rubber bonded to a brass-coated steel wire. The steel wire is cold drawn, then coated with brass be-

a)

b)

Figure 1.1: Cross-section of a rubber composite applied to a) air spring [Torggler et al., 2023] b) car tire [Kim et al., 2019].

fore a last wet drawn. Previous tests were conducted on the whole tire assembly, with a peel-like load on the plies. However, the test does not measure local adherence property but the global structural strength of the tire. Recent problems of material recycling and environment-friendly processes[Sarkar and Bhowmick, 2018] motivate the research for an improvement, or substitute, to the rubber materials in tires. This problem motivates the need for a better understanding of interface failure between elastomer and rigid reinforcement, with an emphasis on delayed fracture and ageing. The goal of this research is to enhance and develop experiments and methodologies to characterize the intrinsic adherence of an elastomer reinforcement and support new material research and developments.

1.1.2 Carbon black reinforced natural rubber

The studied rubber material is based on natural latex, constituted of polyisoprene chain [Vilgis et al., 2009] (chain in fig. 1.2). To form rubber, the latex is vulcanized[1]: a cross-linking reaction occurs between a sulphur addition and the polymer to create a macromolecular network [Akiba and Hashim, 1997, Coran, 2003]. The process involves high temperature and pressure. After the reaction, the liquid-like latex becomes an amorphous solid thanks to the created covalent connection between polymer chains [Treloar, 1975] (network in fig. 1.2). The chains are linked together and stay entangled. The cross-linking reaction must be precisely controlled, by adding either retardant or accelerator, to get the desired macromolecular architecture and material homogeneity [Coran, 2003]. The morphology of the network involves the type of sulphur connection, the length of the polymer chains, and the distance between bridges that determine the

[1] Other cross-linking system exist...

material macroscopic properties [Coran, 2003]. The rubber material is typically used in the rubbery state, above the glass transition temperature.

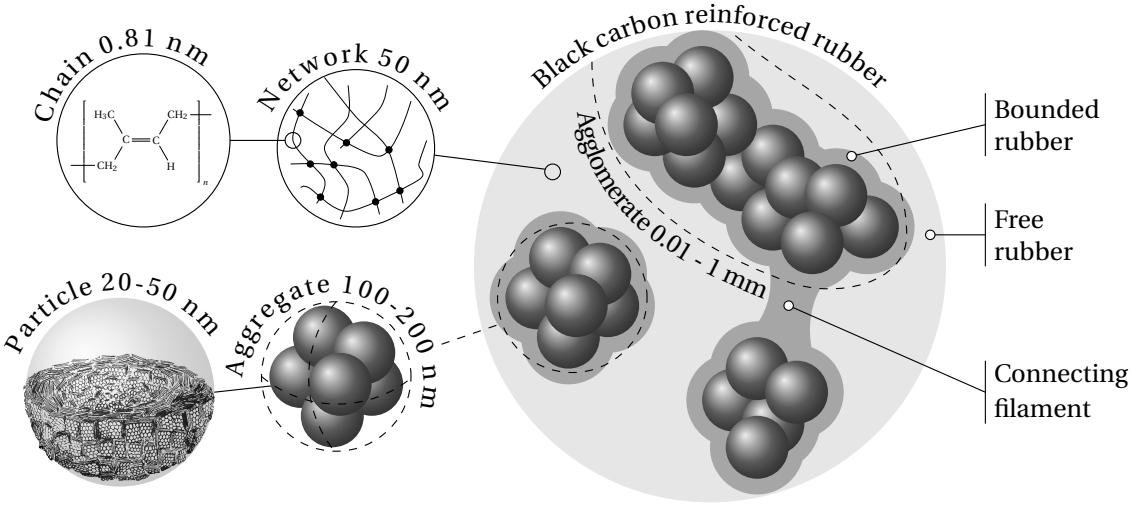

Figure 1.2: Constituents of the natural rubber reinforced by carbon black with their respective scales (adapted from [Heidenreich et al., 1968, Vilgis et al., 2009, Gabriel et al., 2016, Takenaka, 2012]).

At ambient temperature, the polymer network of rubber stretches up to 400% under stress while recovering the deformation almost entirely. This exceptional behavior is attributed principally to the motion of polymer chains [Treloar, 1975]. Without stress, the polymer chain is a flexible *random coil* with a random angle between each monomer. The effective length of the chain can be described by statistical mechanic models [de Gennes, 1979]. Then when mechanically loaded, the polymer rearranges itself to a straight chain, therefore varying the entropy of the system [Meyer and Ferri, 1935] (also a relatively minor temperature change [Anthony et al., 1942]). At the network scale, the total recovery of the initial state requires an interlocking of molecules, enforced by the cross-linking [Treloar, 1975].

At a larger scale, carbon black reinforces the polymer network. The carbon black particle is an onion-like structure of carbon plates [Heidenreich et al., 1968] (particle in fig. 1.2). The particle exists only in aggregates and agglomerates. The rubber bonds to the carbon black with strong covalent bonds that surrounds the agglomerate. The typical size of the polymer coil is at the same scale that the particles, resulting in an interaction in-between [Vilgis et al., 2009]. The interphase between the carbon black and the rubber consists of a layer of low mobility rubber bounded to the carbon black surface [Vilgis et al., 2009, Dannenberg, 1975]. Filaments of bounded rubber can link

two aggregates, constraining the chains during elongation [Dannenberg, 1975] (see fig. 1.2). [Takenaka, 2012] measures the local difference of viscous moduli between the two rubber phases, traducing the chain mobility heterogeneity at the reinforcement scale. Other additives can modify the mechanical response of the material (addition of plasticizer to ease the manufacturing) or aging resistance (protection agents).

The typical consequence of the addition of filler is an increasing strength (to a limit) and a rate-independent like hysteresis, known as softening or Mullins effect [Bouasse and Carrière, 1903, Mullins, 1948]. At a macroscopic scale, the rubber presents a highly non-linear behavior illustrated on a multi-level cyclic tensile test in Fig. 1.3. The largest hysteresis corresponds to the Mullins effect: the material softens for a given stress after the unloading and subsequent loading. If the stress level exceed the previous maximum stress, we retrieve the elastic behavior. The softening also modifies the initial material isotropy and creates directional anisotropy along the loading direction [Machado et al., 2012, Denora and Marano, 2024]. The smaller hysteresis comes from other phenomena such as material viscosity or strain-induced crystallization. The physical origin of the Mullins effect is still debatable in the literature [Denora and Marano, 2024]. The origin is imputed on matrix-filler de-bonding, chain breakage [Clough et al., 2016], and the interaction between bounded and free rubber or molecular slippage in connecting filaments [Dannenberg, 1975]. The softening is partially recoverable after a certain time, accelerated by temperature or swelling by a solvent [Mullins, 1948, Diani et al., 2009, Denora and Marano, 2024].

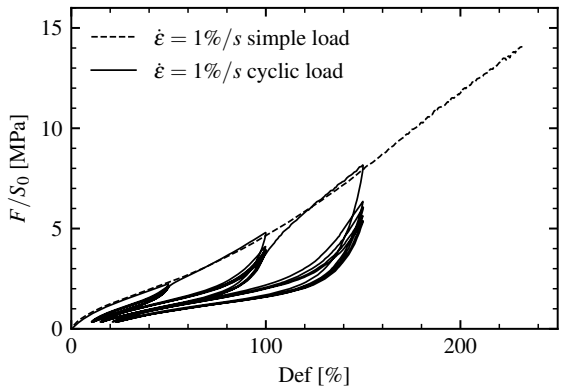

Figure 1.3: Evolution of nominal stress with true strain of in a cyclic tension test result on a black carbon reinforced rubber.

1.1.3 Rubber to brass adhesion

The vulcanization and brass-rubber bonding happen during the same manufacturing process. The brass coating on the metal wire also creates a dendritic copper sulphide structure with the rubber (see fig. 1.4). As the reaction occurs inside the rubber during the process, the rubber and the dendrites are interlocked. It is supposed that a part of the sulphur from the rubber creates covalent bonds on one side with the polymer network and on the other side with the copper from the brass coating [van Ooij et al., 2009, Crowther, 2001, Ozawa and Mase, 2016]. The dendrite size (500 nm) exists at the same scale as the rubber network (see fig. 1.2). Hence, the rubber and dendrites interact as a mechanical interlocking, participating in the macroscopic adhesion [van Ooij, 1984]. The adhesion strength between each metallic layer is of most importance. The sulphide type and dendrite morphology are dependent on rubber formulation (sulphur percentage, accelerator, additives such as cobalt...) [Crowther, 2001].

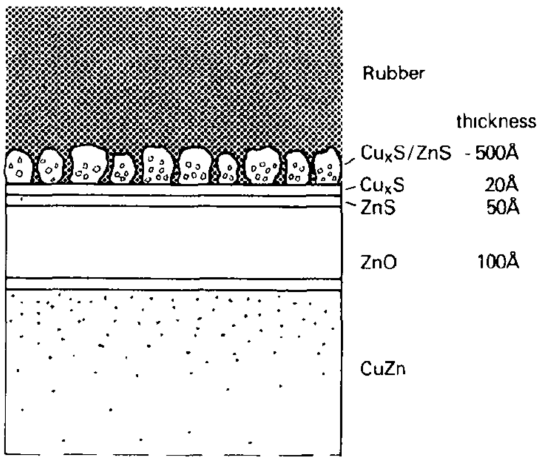

Figure 1.4: Structure of the rubber - brass interface after vulcanization (extracted from [van Ooij, 1984])

The aging of the interface formed between the rubber and the brass is caused by cathodic corrosion, accelerated by water [van Ooij, 1984]. The corrosion forms a zinc oxide layer and weakens the interfacial strength (fig. 1.5). The rubber matrix is supposed to prevent the water from coming into contact with the interface, but can only slow down the process. Practically, the cord can come directly into contact with water in the case of a nail piercing through the tire plies.

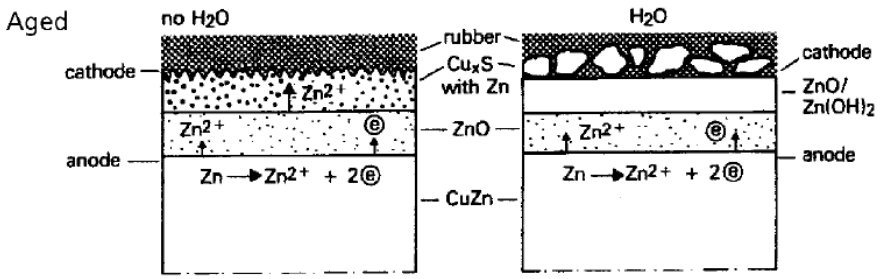

Figure 1.5: Effect of ageing condition on the ageing of the rubber-brass interface (extracted from [van Ooij, 1984])

1.2 Rubber behaviour modelling

1.2.1 Finite strain formulation

To define a constitutive model, we must verify the objectivity condition. The response must be independent of the coordinate system and rigid body motions [Holzapfel, 2000, Lemaitre et al., 2020]. Considering the transformation of a vector from initial configuration $\vec{X}$ to a deformed configuration $\vec{x}$, the deformation gradient is defined as $\underset{\sim}{\boldsymbol{F}} = \partial\vec{x}/\partial\vec{X}$. The polar decomposition of $\underset{\sim}{\boldsymbol{F}}$ allows the separation of deformation components from the rigid body rotation $\underset{\sim}{\boldsymbol{R}}$:

$$\underset{\sim}{\boldsymbol{F}} = \underset{\sim}{\boldsymbol{R}}.\underset{\sim}{\boldsymbol{U}} = \underset{\sim}{\boldsymbol{V}}.\underset{\sim}{\boldsymbol{R}} \tag{1.1}$$

with $\underset{\sim}{\boldsymbol{U}}$ and $\underset{\sim}{\boldsymbol{V}}$ the right and left pure deformation tensors. Two subsequent deformation metrics are derived from the pure deformation tensors, either in the reference configuration (eq. 1.2) or deformed configuration (eq. 1.3).

$$\underset{\sim}{\boldsymbol{C}} = \underset{\sim}{\boldsymbol{F}}^T\underset{\sim}{\boldsymbol{F}} = \underset{\sim}{\boldsymbol{U}}^2 \tag{1.2}$$

$$\underset{\sim}{\boldsymbol{B}} = \underset{\sim}{\boldsymbol{F}}\underset{\sim}{\boldsymbol{F}}^T = \underset{\sim}{\boldsymbol{V}}^2 \tag{1.3}$$

$\underset{\sim}{\boldsymbol{B}}$ is the Cauchy-Green left tensor and $\underset{\sim}{\boldsymbol{C}}$ is the Cauchy-Green right tensor.

The formulation of the mechanical behavior model must respect the objectivity principle. The resulting strain energy density $w(\underset{\sim}{\boldsymbol{F}})$ must be independent of any rigid body displacement or rotation $\underset{\sim}{\boldsymbol{Q}}$ [Lemaitre et al., 2020]. Hence, the behavior uses a deformation metric based on the polar decomposition of $\underset{\sim}{\boldsymbol{F}}$. Most strain potentials are either defined by the principal stretch λ_i or by the invariant of $\underset{\sim}{\boldsymbol{B}}$ defined in eq. 1.4. The principal stretches λ_i can be computed as the square root of the eigenvalues of $\underset{\sim}{\boldsymbol{B}}$ or

the eigenvalues of $\underset{\sim}{\boldsymbol{V}}$. In the following, only the invariant base potential is presented. The invariant $I_3(\underset{\sim}{\boldsymbol{B}})$ (or $J(\underset{\sim}{\boldsymbol{F}})$) concerns the volume variation.

$$I_1 = \mathrm{tr}\underset{\sim}{\boldsymbol{B}} \quad \text{and} \quad I_2 = \frac{1}{2}\left(\left(\mathrm{tr}\underset{\sim}{\boldsymbol{B}}\right)^2 - \mathrm{tr}\underset{\sim}{\boldsymbol{B}}^2\right) \quad \text{and} \quad I_3 = \det\underset{\sim}{\boldsymbol{B}} \tag{1.4}$$

The equivalence between the invariant of $\underset{\sim}{\boldsymbol{B}}$ and $\underset{\sim}{\boldsymbol{C}}$ is retrieved in the case of isotropic materials, only case of interest in the following.

The hyperelastic strain energy density W definition is derived from the Helmotz free energy ψ:

$$\rho_0\psi = w(\underset{\sim}{\boldsymbol{F}}) = w_B(\underset{\sim}{\boldsymbol{B}}) = W \tag{1.5}$$

with ρ_0 the material density in the reference configuration. Introducing the invariant of $\underset{\sim}{\boldsymbol{B}}$ as deformation metric, the hyperelastic strain energy density adopts the form :

$$W = W(I_1, I_2) - \frac{1}{2}\sigma_h(I_3 - 1) \tag{1.6}$$

with σ_h the hydrostatic pressure, a Lagrangian multiplier to enforce the isochoric deformation condition in analytical solutions. Then, the Cauchy stress is derived from the hyperelastic potential by the equation 1.7 assuming an isochoric deformation ($I_3 = 1$) [Lemaitre et al., 2020].

$$\underset{\sim}{\boldsymbol{\sigma}} = \left.\frac{\partial w_B}{\partial \underset{\sim}{\boldsymbol{B}}}\right|_{I_3=1} = 2\frac{\partial W}{\partial I_1}\frac{\partial I_1}{\partial \underset{\sim}{\boldsymbol{B}}}.\underset{\sim}{\boldsymbol{B}} + 2\frac{\partial W}{\partial I_2}\frac{\partial I_2}{\partial \underset{\sim}{\boldsymbol{B}}}.\underset{\sim}{\boldsymbol{B}} - \sigma_h\underset{\sim}{\mathbf{1}} \tag{1.7}$$

By using the principal stretches λ_i, it simplifies to:

$$\sigma_i = \lambda_i\frac{\partial W}{\partial \lambda_i} - \sigma_h \tag{1.8}$$

Employing a deformation metric in reference or intermediate configuration would lead to other stress metrics such as first and second Piola-Kirchhoff stress tensors [Lemaitre et al., 2020].

1.2.2 Strain potentials

Various strain potentials based on hyperelasticity exist to describe the non-linear elastic behavior of an elastomer [Marckmann and Verron, 2006]. Some simple forms based on invariants are in the table 1.1.

The strain potentials are either phenomenological or physically based [Marckmann and Verron, 2006]. The Mooney-Rivlin expansion potential [Rivlin and Rideal, 1948] is based solely on mathematical consideration. Meanwhile, the material parameter

Neo-Hookean:	$W = \frac{\boldsymbol{\mu}}{2}(I_1 - 3)$
Generalized Neo-Hookean:	$W = \frac{\boldsymbol{\mu}}{2\boldsymbol{b}}\left\{\left[1 + \frac{\boldsymbol{b}}{\boldsymbol{n}}(I_1 - 3)\right]^{\boldsymbol{n}} - 1\right\}$
Mooney-Rivlin:	$W = \sum_{m,n} \mathbf{c}_{mn}(I_1 - 3)^m (I_2 - 3)^n$
Exp-Ln:	$W = \mathbf{A}\left[\frac{1}{\mathbf{a}}\exp(\mathbf{a}(I_1 - 3)) + \mathbf{b}(I_1 - 2)(1 - \ln(I_1 - 2)) - \frac{1}{\mathbf{a}} - \mathbf{b}\right]$

Table 1.1: Some strain potentials with the material parameters in bold.

μ from the Neo-Hookean model can be defined by $\nu_{ch}\kappa_B T$ [2] based on the Gaussian deployment of the polymer chains[Treloar, 1943]. Nonetheless, it is limited to small to moderate strain because the strain stiffening visible in rubber is not modeled. The Generalized Neo-Hookean can model the large strain stiffening [Qi et al., 2018]. An alternative is the Exp-Ln model [Khajehsaeid et al., 2013] that models accurately both the moderate and large strain. This potential gave good results [Kane et al., 2021] and is used in the rest of the work.

1.2.3 Mullins Dissipation

The various energy dissipation observed during the cyclic loading of rubber are possible sources of dissipation during crack growth. It is necessary to model this behavior for a qualitative partitioning of the dissipative mechanism during the rubber interface fracture. Here, we focus only on the softening modeling. The other dissipations are not the focus of the developments.

The hysteresis observable only on the first loading cycle corresponds to a softening of the material. To model the increase of compliance, multiple paradigms exist in the literature [Diani et al., 2009]. The pseudo-elastic approach proposed by [Ogden and Roxburgh, 1999] proposes to alter the strain energy potential W by a factor η. This simple approach is readily available in commercial finite element code Abaqus and is chosen for the present work. The modified strain energy should be rewritten as follow :

$$\tilde{W}(I_1, I_2, \eta) = \eta W(I_1, I_2) + \phi(\eta) \tag{1.9}$$

η remains equal to 1 during initial loading and decrease to η_{min} during unloading. The

[2] ν_{ch} is the number of chains, T the absolute temperature and κ_B the Boltzmann constant

original formulation [Ogden and Roxburgh, 1999] for η is :

$$\eta = 1 - \frac{1}{r}\text{erf}\left(\frac{W_{max} - W}{m + \beta W_{max}}\right) \tag{1.10}$$

with m, β, and r the material parameters and W_{max} the maximum strain energy experienced by the material. Under uniaxial loading, the prediction can reproduce the rubber material's cyclic behavior. To introduce an induced anisotropy and a residual strain, [Dorfmann and Ogden, 2004] later added a secondary strain potential that activates during unloading and leaves a residual strain.

A second approach treats the softening as a damage mechanism such as $(1-D)W$ [Diani et al., 2015]. A further extension to a directional dependence is proposed to model an induced anisotropy [Diani et al., 2015, Machado et al., 2014]. [Diani et al., 2015] notes that a directional model can naturally reproduce the residual strain. Besides, [Cantournet et al., 2009] relies upon a molecular slippage origin of the Mullins effect to build a constitutive law of hysteresis and stress decrease under multiple cycles.

The pseudo-elastic approach of [Ogden and Roxburgh, 1999] does not respect the energy conservation law of the thermodynamic, but can be adapted [Qi et al., 2018]. The damage approach is built in the thermodynamic framework [Diani et al., 2015]. The choice of history parameter ($\sqrt{2W}$,W, I_1, I_2...) used by the variable to alter the elastic strain potential could be disregarded on uniaxial loading. However, particular attention is necessary to predict correctly a multiaxial loading [Machado et al., 2012].

Other dissipations are responsible for the smaller hysteresis in figure 1.3 are typically modeled based on time-dependent behavior, and remain out of the scope of the present work.

1.3 Fracture of soft-rigid interface

The fracture of the interface involves the failure of the interface itself, failure of the interphase, or failure of the bulk. In all cases, the bonded materials dissipate energy. Here, we focus on bonding, an irreversible case of adhesion, and adherence energy, developed during the failure of such bonding. [Griffith and Taylor, 1921] propose an energetic argument to describe the propagation of a crack. The strain energy release rate (SERR) metric G is introduced as the dissipation D necessary to create a new surface S. In an elastic system that can store energy, the dissipation D is equal to the

release of potential energy E_{el} and exterior work provided to the system W_{ext}:

$$G = -\frac{\partial D}{\partial S} = -\frac{\partial (E_{el} - W_{ext})}{\partial S} \tag{1.11}$$

The condition of crack propagation is met when G reaches a critical value noted G_C. The critical strain energy release rate G_C is often presented as an intrinsic mechanical property of a material or an interface. The concept of SERR permits the reduction of the effect of geometry or loading condition, as an intrinsic material property to qualify the resistance to crack growth of a solid. The following discussion is limited to rubber-like material and crack growth. Crack onset and toughness measurement are not in the scope of the work. To clarify the notation, we chose to mark the SERR at G (possible or potential or available SERR) and the SERR value leading to crack propagation G_C. Some authors mark the critical SERR value Γ instead of G_C.

1.3.1 Crack growth in a soft solid

As a first step to understanding the origin of dissipation during crack growth at the interface, we discard the interface to focus only on the soft solid crack. The literature is prolific on crack growth and the subsequent section gives a non-exhaustive listing of possible dissipation. The selected behavior will provide only the necessary understanding for our study.

Experimental observations

The fracture behavior of soft material has been an extensive research field since the first study of [Rivlin and Thomas, 1953]. The resulting strain energy release rate was reported much higher than the theoretical energy. The fracture, when creating a new surface, is supposed to correspond to the energy dissipated by the breakage of the polymer chains. It corresponds to a dissipation typically around 10^{-3} to $10^{-2}\mathrm{J/m^2}$, much lower than typical G values observed on rubber reaching 1 to $10\mathrm{kJ/m^2}$ [Rivlin and Thomas, 1953]. Therefore, other mechanisms than purely the chain breakage are dissipating during crack growth, related to the dissipative macroscopic behavior of the material.

[Knauss, 1973] reported a significant variation of G_C with crack velocity and temperature, correlated to the glass transition of the material. This is typical of viscous dissipation during crack growth [Persson et al., 2005, Creton and Ciccotti, 2016] leading to higher dissipation at high crack velocity and/or low temperature. [Qi et al., 2024]

were able to compute the dissipated energy during crack growth of a viscous solid at large strain. On the other hand, an initial loading of the rubber material decreases the global dissipation. This decrease corresponds to a decrease of Mullins dissipation available for dissipation during crack growth [Roucou et al., 2020, Roucou, 2020, Qi et al., 2018, Diani et al., 2015, Mai et al., 2021].

At the scale of the local dissipation and processes of fracture, [Slootman et al., 2020] observe the chain breakage at the crack tip in dual network hydrogels, revealing a diffuse damage zone not limited to the direct vicinity of the crack. In the case of filled rubber, [Xiang et al., 2022] observes both cavitation and crystallization at the crack tip, varying with the filler ratio.

Fracture process modelling

A crack in an elastic (or hyperelastic) solid is a material discontinuity. It also creates a discontinuity of displacement and stress fields but also singular stress fields in the vicinity of the crack tip [Lemaitre et al., 2020]. The asymptotic stress distribution has no physical meaning but can be regularized in a region called the process zone, where a failure process (damage, cleavage, crazing, cavitation) occurs to propagate the crack surface.

Using a global energetic approach with the SERR, [Griffith and Taylor, 1921] permits us to circumvent the problem. In case of dissipation occurring both in the process zone and in a larger region of the material, the global SERR G is related to the process zone dissipation G_0 and the outer dissipation G_D by a sum [de Gennes, 1996].

Local treatment of this non-linear region uses the cohesive zone modeling (CZM) approach based on the pioneering work of [Dugdale, 1960] and [Barenblatt, 1962]. The CZM allows us to model both the crack onset and propagation by introducing a critical stress and a critical SERR, with an implicit process zone length, in a plane of the solid continuum. Various traction-separation shapes exist [Alfano, 2006], the most common being the triangular law. A natural extension of this approach is the phase-field fracture, where the regularization is no longer restricted to the crack surface. The process zone region becomes diffuse inside the solid [Talamini et al., 2018].

Viscous dissipation modelling

The modeling of a steady-state crack growth in a small-strain visco-elastic solid has been an extended research field since the work of [Knauss, 1973]. Multiple approaches

emerged with purely global [de Gennes, 1996] or with local approach [Hui et al., 2022]. [Kroon, 2011] studies the extension to visco-hyperelasticity. The majority of these works can be resumed as an increasing global SERR with an increasing crack velocity. Furthermore, the additive decomposition $G = G_0 + G_D$ leads to a multiplicative dependence between G and G_0 [de Gennes, 1996].

Mullins dissipation modelling

The recent studies [Zhang et al., 2015, Long and Hui, 2016, Qi et al., 2018] on the crack growth in hydrogel use the Mullins effect to model their exceptional SERR. [Qi et al., 2018] proposes a model for the steady-state crack growth with a Neo-Hookean solid with a pseudo-elasticity based on [Ogden and Roxburgh, 1999] and a cohesive zone. The model is consistent with the thermodynamic framework, unlike the earlier work of [Zhang et al., 2015] on the same solid based on empirical consideration. [Qi et al., 2018] choses an additive separation of the global G between the cohesive zone contribution G_0 and the material hysteresis contribution G_D. A result is the diminution of G with the pre-softening, as part of the possible dissipated energy was already used during the pre-softening step (see fig. 1.6). Furthermore, the additive decomposition ends up in a multiplicative relation between the G and G_0 as G_D is dependent on G_0 (similar to the viscous dissipation during crack growth).

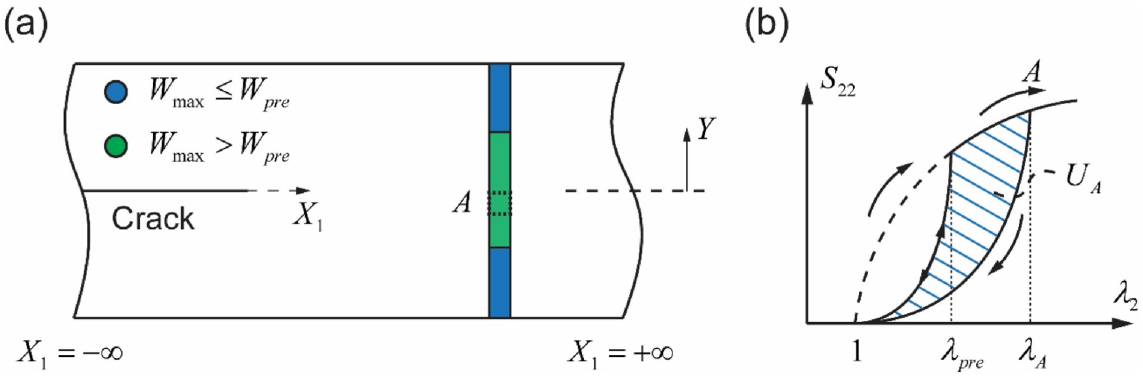

Figure 1.6: Crack growth in a elastomer softened up to W_{pre} / λ_{pre}. Repartition of the dissipative region (in green $W_{max} > W_{pre}$) in a) and the available hysteresis dissipation U_A of material points A from the green region when loaded-unloaded by the passing crack growth b) (extracted from [Qi et al., 2018]).

It should be noted that the anisotropy induced by softening [Diani et al., 2009] has not yet been accounted for in these different analyses and modeling. Furthermore,

the recovery is not addressed as those works focus on quasi-static crack growth, not delayed crack growth.

1.3.2 Crack growth at a soft - rigid solid interface

In this work, the focus is on the interface between a deformable solid and a rigid substrate. In the rubber cord case, the hypothesis of rigidity is based on the difference of moduli between the metal cord and the rubber and that the chosen test induces negligible strain in the substrate. The simplification eases the analysis and permits to focus only on the soft solid dissipation.

Experimental observations

With a dissimilar material interface, the crack growth shape becomes dependent on the macroscopic loading conditions, introducing the concept of crack mode. In figure 1.7, the global deformation and crack opening profile are different depending on the load condition. The opening mode in Fig. 1.7b shows a large crack blunted crack. The negative shear mode in Fig. 1.7 results in a sharp crack while a negative shear mode in Fig. 1.7c gives a very wide opening [Liechti and Wu, 2001]. The modification of the fields around the crack tips results in a different global dissipation [Cook et al., 1997, Liechti and Wu, 2001, Liechti et al., 1989, Neggers et al., 2015].

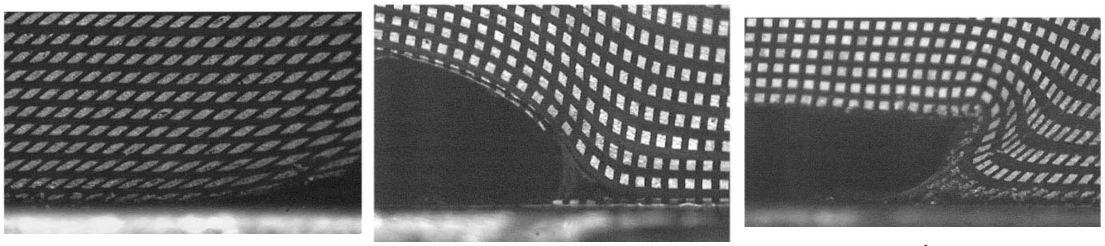

a) b) c)

Figure 1.7: Rubber interface crack growth under a) negative shear b) opening and c) positive shear mode (adapted from [Liechti and Wu, 2001])

Different mechanisms are observed in the vicinity of the crack during propagation. Firstly, if the fracture is cohesive with a substantial elastomer residue, the damage process should share similarities with bulk crack growth. Secondly, if the fracture is adhesive with a surface with little to no rubber residue, other damage processes could appear such as fibrillation [Neggers et al., 2015] (see fig. 1.8).

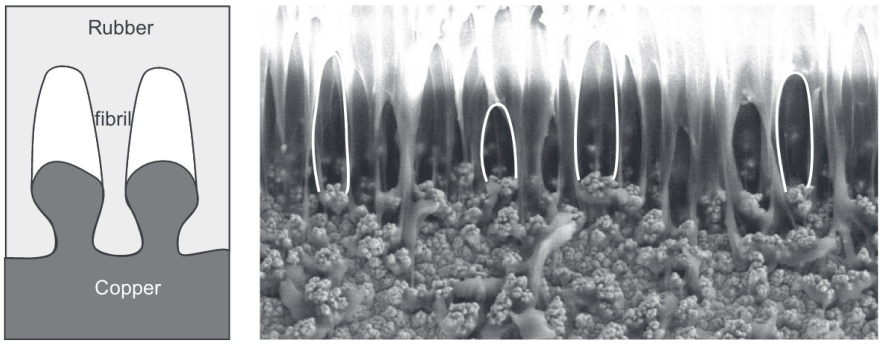

Figure 1.8: Fibrillation mechanism (left) and observation (right) in the process zone during an interface crack growth between silicone rubber and a copper substrate (extracted from [Neggers et al., 2015]).

Fracture process modelling

Multiple authors in the literature use the cohesive zone approach to model the interface crack growth [Neggers et al., 2015, Liechti and Wu, 2001, Meng and Chang, 2020, Mukherjee et al., 2016, Yang et al., 2020, van den Bosch et al., 2008, Elzière, 2016, Cao et al., 2016, Gilormini and Diani, 2015, Pandey et al., 2020]. The main difference with the application in homogenous solid is the addition of a mode-mixity dependence. The dissipated energy G is separated in the opening G_I and shear components G_{II}.

The deformed shape of the process zone can correspond to the apparent fibrillation region [Liechti and Wu, 2001], visible in figure 1.7 when accounting for both CZM and material dissipation. Nonetheless, [Neggers et al., 2015] notes that the cohesive zone overestimates the size of fibrillation when it is considered that the CZM concentrates all dissipated energy during the crack propagation process. Hence, the CZM approach, while respecting the balance of energy during crack growth $G_C = G_C^{\text{CZM}}$, is not necessarily enough to model the process zone shape.

Viscous dissipation modelling

The previous visco-elastic modeling of crack growth in solid is still applicable to interface supposing small-strain, leading to similar conclusion [de Gennes, 1996]. With numerical modeling, [Liechti and Wu, 2001] successfully reproduced the interface fracture both on dissipation and strain field based on a viscous mode mixed CZM and viscous material, proving the viability of an approach combining CZM and material dissipation.

1.4 Mechanical tests

1.4.1 Behaviour tests

To characterize the intrinsic mechanical behaviour of a material, the structure effect must be discarded by applying a homogenous strain field.

Uniaxial tension

The transformation gradient $\underset{\sim}{\boldsymbol{F}}$ and the left Cauchy-Green strain tensor $\underset{\sim}{\boldsymbol{B}}$ for a uniaxial load along $\vec{x}$ corresponds to the eq. 1.12. The resulting invariant of $\underset{\sim}{\boldsymbol{B}}$ are $I_1^B = \lambda^2 + 2\lambda^{-1}$ and $I_2^B = 2\lambda + \lambda^{-2}$. Then, applying eq. 1.8 with a strain potential gives the stress tensor.

$$\underset{\sim}{\boldsymbol{F}} = \begin{bmatrix} \lambda & 0 & 0 \\ 0 & \lambda^{-1/2} & 0 \\ 0 & 0 & \lambda^{-1/2} \end{bmatrix} \quad \text{and} \quad \underset{\sim}{\boldsymbol{B}} = \begin{bmatrix} \lambda^2 & 0 & 0 \\ 0 & \lambda^{-1} & 0 \\ 0 & 0 & \lambda^{-1} \end{bmatrix} \tag{1.12}$$

Thick-walled rubber tube inflation

The inflation of a thick-walled rubber cylinder can be fully described with an analytical model. The first solution is proposed by [Skala, 1970] to study the inflation of the rubber model. Assuming the hypothesis of axisymmetry and incompressibility, equations are proposed to model the free inflation of a thick-walled rubber cylinder tests with a Neo-Hookean and a Mooney strain potential. The main difference between thin and thick-walled cylinder inflation is the radial distribution of strain, typically neglected for a thin-walled cylinder. The choice of potential influences directly the predicted kinematic of inflation and the finite strain instability in pressure [Skala, 1970].

[Holzapfel et al., 2001] generalizes the framework to inflation, tension, and torsion load. Furthermore, the derived model can include layered cylinder wall materials, anisotropy, and pre-stress (fig. 1.9). The application is the inflation of arterial [Holzapfel, 2004, Schulze-Bauer et al., 2002].

In the following, the analytical model allows the computation of the stored strain energy during the adherence test [Kane et al., 2019]. The equations of the model correspond to the original development of [Skala, 1970] with the addition of a confined inflation boundary condition.

The material's assumptions are hyperelasticity and incompressibility $\lambda_r \lambda_\theta \lambda_z = 1$. The deformation is supposed axisymmetric, thus the coordinates are cylindrical $\vec{r}\vec{\theta}\vec{z}$.

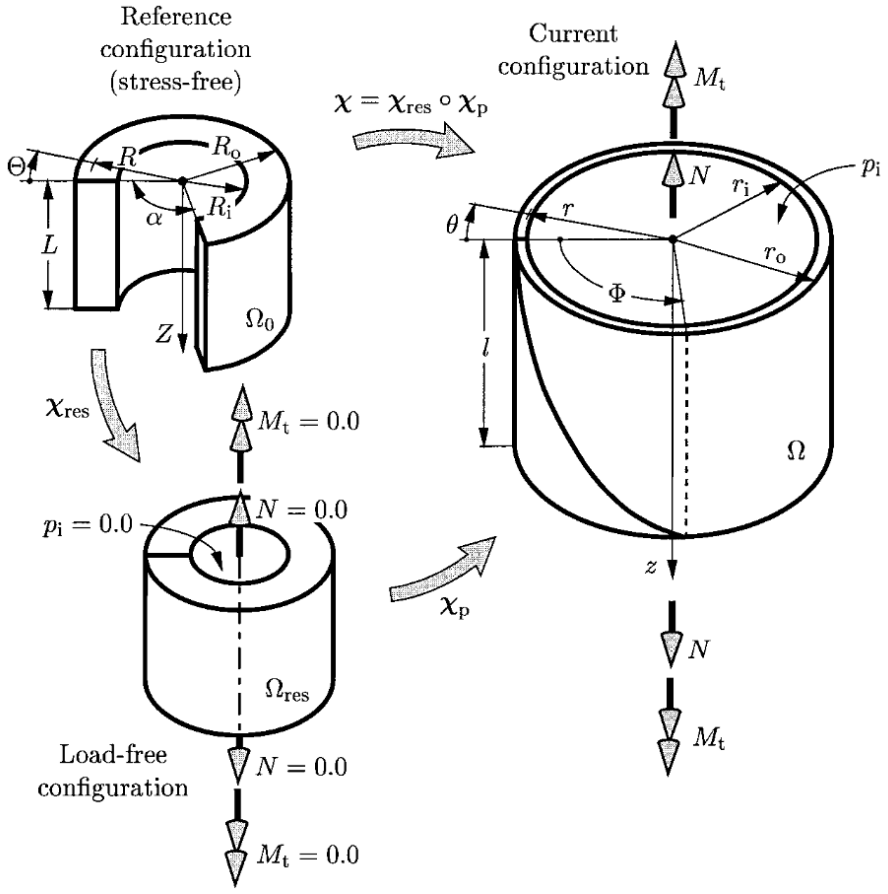

Figure 1.9: Pre-stressed thick walled tube under combined inflation, tension and torsion (extracted from [Holzapfel et al., 2001])

The axial elongation λ_z is supposed constant along z. The radial and circumferential stretches vary along the radius. The stretches are defined in eq. 1.13.

$$\underset{\sim}{\boldsymbol{F}} = \begin{bmatrix} \lambda_r = \dfrac{\mathrm{d}r}{\mathrm{d}R} & 0 & 0 \\ 0 & \lambda_\theta = \dfrac{r}{R} & 0 \\ 0 & 0 & \lambda_z = \dfrac{z}{Z} \end{bmatrix} \tag{1.13}$$

Combining the definition of λ_r and λ_θ gives :

$$\lambda_r = R\frac{\mathrm{d}\lambda_\theta}{\mathrm{d}R} + \lambda_\theta \tag{1.14}$$

Then the incompressibility conditions gives

$$\frac{\mathrm{d}R}{R} = -\lambda_\theta \frac{\mathrm{d}\lambda_\theta}{\lambda_\theta^2 - \lambda_z^{-1}} \tag{1.15}$$

The last equation can be integrated to give :

$$\lambda_\theta^2 = \lambda_z^{-1} + (cR^2)^{-1} \tag{1.16}$$

with c being the integration constant (computed later with the boundary conditions). Note that λ_z is treated as a constant during integration. To use the deformed radius r rather than the initial radius R as control parameter, the eq. and the definition of λ_θ are combined to give :

$$r = \sqrt{R^2/\lambda_z + c^{-1}} \tag{1.17}$$

Then eq. 1.16 is rearranged with the eq. 1.17 to give explicit forms of the circumferential stretch:

$$\lambda_\theta^2(r) = \frac{1}{\lambda_z}\left[\frac{cr^2}{cr^2-1}\right] \tag{1.18}$$

And similarly for the radial stretch :

$$\lambda_r^2(r) = \frac{1}{\lambda_z}\left[\frac{cr^2-1}{cr^2}\right] \tag{1.19}$$

Those two last equations are continuity equations for isochoric and radially-symmetric large deformations [Skala, 1970]. Then, to accommodate any strain potential form, we continue with the development presented in [Kane et al., 2021] based on a numerical computation of the solution. The model varies the inner radius of the tube and computes the stresses and the stretches based on the boundary conditions. In both cases, the tube is supposed to be closed at both ends and the inner radius radial stress is equal to the inflation pressure. The unconfined cases give the condition of a free surface on the external radius (Unconfined Inflation Solution UIS). The confined cases fix the external radius position at the radius of confinement R_{conf} (Confined Inflation Solution CIS), assuming frictionless contact between the exterior radius and the confinement.

We fix an inner radius position r_{int} and try an exterior radius position r_{ext}. The explicit relation between the inner and outer radius with the axial elongation λ_z and the integration constant c are presented in eq.1.20 and eq.1.21.

$$\lambda_z = \frac{R_{ext}^2 - R_{int}^2}{r_{ext}^2 - r_{int}^2} \tag{1.20}$$

$$c^{-1} = \frac{r_{int}^2 R_{ext}^2 - r_{ext}^2 R_{int}^2}{R_{ext}^2 - R_{int}^2} \tag{1.21}$$

The radial and circumferential stretches are computed with eq. 1.19 and eq. 1.18. The stretch distribution along the radius is known and the deviatoric stress is computed. As

the problem is formulated in principal stretches only, the Cauchy stress σ corresponds to eq. 1.8 where the spheric part is the pressure σ_h and the deviatoric part is derived from the strain potential :

$$s_i = \sigma_i + \sigma_h = \lambda_i \frac{\partial W}{\partial \lambda_i} \tag{1.22}$$

The static equilibrium equations in cylindrical coordinates correspond to eq. 1.23.

$$\frac{\mathrm{d}\sigma_r}{\mathrm{d}r} + \frac{\sigma_r - \sigma_\theta}{r} = 0 \tag{1.23}$$

Using the spheric-deviatoric decomposition of eq. 1.22 and eq. 1.23, the hydrostatic pressure distribution along the radius is :

$$\frac{\mathrm{d}\sigma_h}{\mathrm{d}r} = \frac{\mathrm{d}s_r}{\mathrm{d}r} + \frac{s_r - s_\theta}{r} \tag{1.24}$$

Then, in integral form :

$$\sigma_h(r) = s_r(r) - s_r(r = r_{int}) + \int_{r_{int}}^{r_{ext}} \frac{s_r(u) - s_\theta(u)}{u} \mathrm{d}u + \sigma_h(r = r_{int}) \tag{1.25}$$

The hydrostatic distribution corresponds to constant $\sigma_h(r = r_{int})$ plus a radial distribution $\mathscr{P}(r)$ determined by trapezoidal integration.

$$\sigma_h(r) = \mathscr{P}(r) + \sigma_h(r = r_{int}) \tag{1.26}$$

The hydrostatic constant must be determined with the boundary condition. The closed-end condition gives the relation between the inflation pressure P and the axial Cauchy stress σ_z in eq. 1.27.

$$2\pi \int_{r_{int}}^{r_{ext}} \sigma_z(u) u \mathrm{d}u = P\pi r_{int}^2 \tag{1.27}$$

And the inner radius radial Cauchy stress $\sigma_r(r_{int})$ corresponds to the resultant of the inflation pressure P :

$$\sigma_r(r = r_{int}) = -P \tag{1.28}$$

Hence, combining the eq. 1.25 and the boundary condition described in eq. 1.27 gives :

$$P\pi r_{int}^2 = -\sigma_h(r_{int})\pi(r_{ext}^2 - r_{int}^2) + 2\pi \int_{r_{int}}^{r_{ext}} [s_z(u) - \mathscr{P}(u)]\, u \mathrm{d}u \tag{1.29}$$

Using the expression of the inflation pressure in eq. 1.28, the eq. 1.29 becomes the eq. 1.30, solved by trapezoidal integration.

$$\sigma_h(r_{int}) = \frac{r_{int}^2}{r_{ext}^2} s_r(r_{int}) + \frac{2}{r_{ext}^2} \int_{r_{int}}^{r_{ext}} [s_z(u) - \mathscr{P}(u)]\, u \mathrm{d}u \tag{1.30}$$

Now, in an unconfined regime, the r_{ext} value is adjusted iteratively by a Newton-Raphson algorithm to find the solution that matches the boundary condition $\sigma_r(r = r_{ext}) = 0$. The confined regime imposes the exterior radius, hence the iterative loop for r_{ext} is not necessary. Note that both solutions are computed over a full range of $r_{int} = [R_{int}{:}6R_{int}]$ but their validity condition is not always fulfilled. The condition to choose either UIS or CIS comes from the value of the deformed external radius below the confinement radius $r_{ext} < R_{conf}$, giving the mixed inflation solution (UIS+CIS=MIS). An example is presented in Fig 1.10.

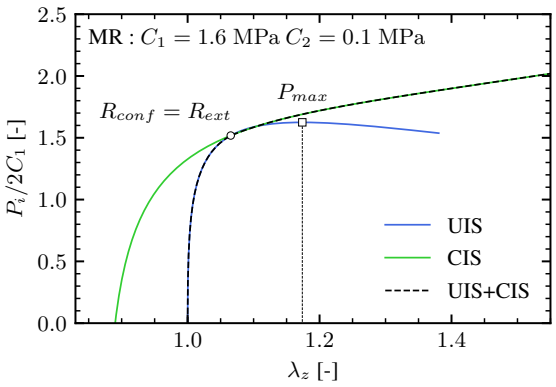

Figure 1.10: Evolution of the inflation pressure with the axial elongation of the thick tube for a Mooney-Rivlin solid ($R_{conf} = 5\,$mm, $R_{int} = 0.65\,$mm and $R_{ext} = 4.7\,$mm)

The extension of this framework to unconfined/confined inflation-tension is presented in chapter 5, to contact friction in chapter 4, and to a softening material under cyclic inflation in chapter 6.

1.4.2 Adherence tests

In the following, various adherence tests are presented and their relevance to the wire-rubber configuration is discussed.

Peel tests

The peel test exists in a wide range of geometry [Bartlett et al., 2023] for each application. Multiple standards present the varying angle peel test [ASTM D3330, 2018], the T-peel test [ASTM D1876, 2015], or the climbing drum peel test [ASTM D1781, 2012]. Various authors use peel test to qualify elastomer-rigid adhesion [Cook et al., 1997, Neggers et al., 2015, Toulemonde et al., 2018, Gent and Hamed, 1977a, Gent and

Hamed, 1977b]. The classical geometry is the peeling of the adherent at a fixed peel angle θ (fig. 1.11) and the peel force is measured to compute the adherence.

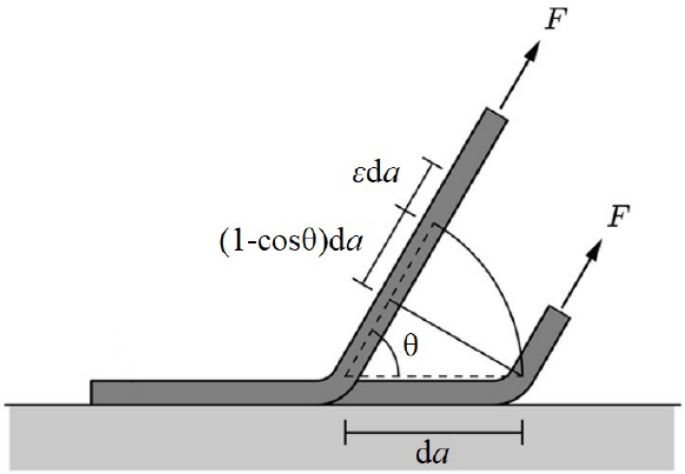

Figure 1.11: General peel test geometry with the substrate in light gray and the membrane in dark gray before and after a crack propagation increment δa (extracted from [Sauer, 2011]).

The peel force is related to the strain energy release rate in a perfectly inextensible membrane. The dissipation produced by fracture of the surface is directly related to the applied external work, leading to eq. 1.31 [ASTM D3330, 2018]. However, if the membrane stores (elasticity, see fig. 1.11) or dissipates (plasticity) some energy, the SERR computed with an in-extensibility hypothesis will be strongly thickness-dependent and adherent dependent [Bartlett et al., 2023, Gent and Hamed, 1977b]. An experimental trick is to add an inextensible backing on the membrane to agree with the solution of eq. 1.31. However, the backing addition is cumbersome and discarded in some cases. The sample preparation needs a better adhesion with the backing than with the substrate, else the wrong interface is tested. In an artificial ageing study, the backing will block diffusion.

$$G = \frac{F}{w}\left[1 - \cos\left(\theta\right)\right] \tag{1.31}$$

In the case of a hyperelastic adherent, the membrane extensibility enforces the computation of the stored elastic energy in the membrane. As an example, the SERR of the peel test is computed following the seminal approach of [Rivlin and Thomas, 1953] (yielding a similar result to [Sauer, 2011]). An energy balance compares the state of the system after a virtual crack advances δa.

The energy balance is :

$$\delta W_{ext} = \delta E_{el} + G\delta S \tag{1.32}$$

After a crack advance for a 90° peeling, a section of material $\delta S = w\delta a$ is detached from the substrate and stretched up to ε under a tension load F. The variation of exterior work corresponds to:

$$\delta W_{ext} = F\varepsilon\delta a \tag{1.33}$$

If we consider a different peel angle θ, a contribution of rotation appears in the exterior work :

$$\delta W_{ext} = F\left[1 + \varepsilon - \cos(\theta)\right]\delta a \tag{1.34}$$

with $1 + \varepsilon = \lambda$:

$$\delta W_{ext} = F\left[\lambda - \cos(\theta)\right]\delta a \tag{1.35}$$

The strain energy corresponds to the uniaxial tension (eq. 1.12) of a volume $w \times t \times \delta a$ of hyperelastic material:

$$\delta E_{el} = W(I_1, I_2)\, w\, t\, \delta a \tag{1.36}$$

with w the width and t the thickness of the adherent. Hence :

$$G = \frac{F}{w}\left[\lambda - \cos(\theta)\right] - tW(I_1, I_2) \tag{1.37}$$

The evolution of G from eq.1.37 with a Neo-Hookean strain potential is presented in Fig. 1.12, compared to the inextensible computation of G. Taking an equal G_C between a rigid and compliant system leads to a different critical peel force. The stretch and the strain energy are computed from the applied peel force with a Newton-Raphson algorithm applied to the eq. 1.38.

$$0 = \frac{\partial W(I_1, I_2)}{\partial \lambda} - \frac{F}{w.t} \tag{1.38}$$

The peel angle variation offers a wide range of possible crack mode mixity and a test to study the mode mixity effect on G [Cook et al., 1997]. The crack velocity is proportional to the displacement of the detached adherent, allowing a study of the dependence of G on the crack velocity. However, the peel test configuration is limited to testing only flat surfaces. The application to a cord or wire geometry will introduce a strong structural effect (i.e. peeling of a ply of cord). Alternatively, a flat brass substitute could not mimic the surface morphology of a brass-coated wire.

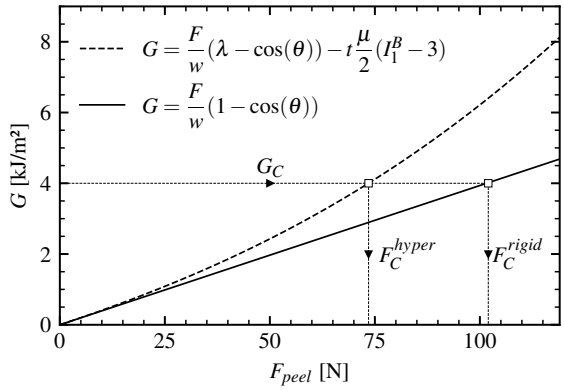

Figure 1.12: Evolution of the strain energy release rate with the peel force with inextensible and hyperelastic (Neo-Hookean) hypothesis ($w = 25.4\,\text{mm}$, $t = 3\,\text{mm}$, $\theta = \pi/2$, $\mu = 0.3\,\text{MPa}$)

Pull-out tests

The ubiquitous testing method to qualify the bonding between a reinforcement and an elastomer matrix is the pull-out test [Rey et al., 2014, Meng and Chang, 2020, Gent et al., 1981, Chandra et al., 1996, Fielding-Russell et al., 1979, Jamshidi et al., 2005]. Different standards focus either on metal cord [ASTM D2229, 2014], metal wire [ASTM D1871, 2014], or non-metallic reinforcement [ASTM D4776, 2004]. Generally, the reinforcement is the pull-out of a block of matrix (fig. 1.13a), and the pull-out force is the only measure used to characterize the adherence. Some empirical equations are proposed to compute the SERR assuming linear elasticity [Gent et al., 1981].

A modification of [Ellul and Emerson, 1988] is supposed to cancel the matrix contraction during the pull loading and minimize the friction effect between the detached cord and the rubber (see 1.13b). [Meng and Chang, 2020] use a similar setup to test the adhesion of a copper wire to PDMS advocating the tubular shell is necessary if the elastomer reaches high deformation during the test (see fig. 1.14). Nonetheless, after the initial force peak corresponding to crack onset, the propagation regime dissipation is shared between interface fracture and crack faces friction (while the fracture surface is adhesive with little to no elastomer residue).

To tackle the same problem, [Gent and Yeoh, 1982] uses a pressurized gas injected into the cord to cancel the friction effect (but needs a hollow cord). Unlike the peel test, the crack mode mixity is not tunable. Meanwhile, a class of tests uses only a pressurized fluid for adhesion testing.

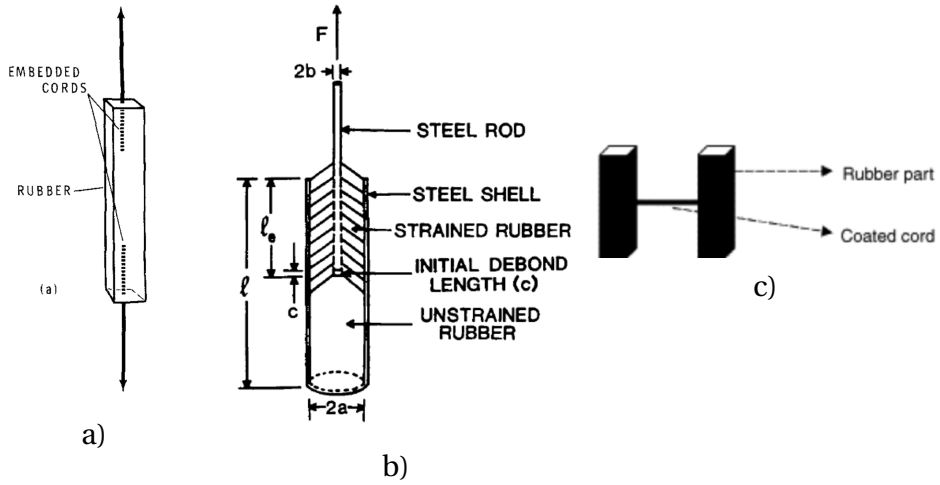

Figure 1.13: H-test geometry in a) (extracted from [Gent et al., 1981]), modified in b) (extracted from [Ellul and Emerson, 1988]) and H-test (extracted from [Jamshidi et al., 2005]).

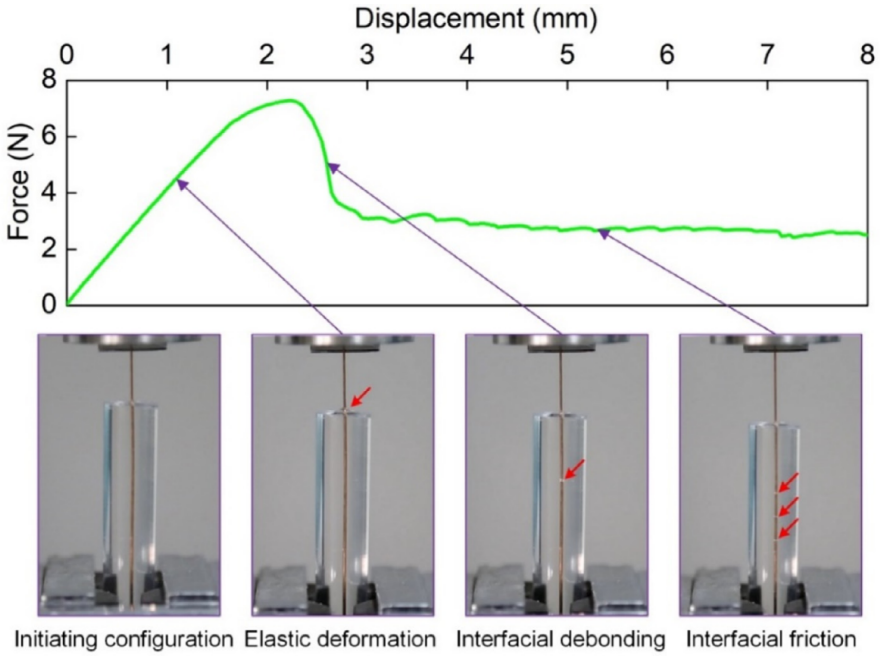

Figure 1.14: Pull-out experiment between a PDMS and a copper wire (extracted from [Meng and Chang, 2020]).

Blister tests

The blister adhesion tests are presented—the basic principle in the propagation of a crack/delamination front with a pressurized fluid. From 1961 to 2019, multiple geometries of inflation tests have emerged [Bartlett et al., 2023].

The first adhesion test using inflation is the oblong blister test proposed by [Dannenberg, 1961]. The principle is the creation and the propagation of a blister with a pressurized fluid. Liquid mercury under pressure propagates the crack. An oblong-shaped constraint enforces the propagation along one direction. Meanwhile, confinement blocks the expansion of the delaminated film. The result of the experiment is a constant pressure during propagation. The dissipated energy during propagation corresponds to the area under the inflation curve minus the area under the deflation curve. Then, the critical strain energy release rate is equal to dissipated energy divided by the surface created by the crack propagation. Analytical models based on linear elastic plate kinematic are proposed later to compute the SERR and mode mixity [Williams, 1997, Jensen, 1998], applied mainly to flat axisymmetric geometries [Chang et al., 1989, Jensen, 1991, Chang and Peng, 1992]. For confined blister tests, the SERR is proportional to the inflation pressure P and the gap between the membrane and the confinement h. A geometrical factor α, varying between 0 and 1, is supposed to represent a geometric effect.

$$G = \alpha P h \tag{1.39}$$

Compared to a peel test, the blister tests are not standard and rarely used because a pressurized fluid circuit is less common than a tensile test machine in most laboratories [Bartlett et al., 2023]. The peel angle must stay low and depends on the test geometry (the de-bonded radius or the height between the film and the confinement).

Rubber Cord Adhesion Inflation Test

[Kane, 2020] originally proposed the RCAIT to assess the interface adhesion between a rubber envelope and a metal cord. The test shares similarities with the confined blister test [Dannenberg, 1961, Chang et al., 1989], however in a tubular geometry. A thick elastomer membrane encompasses a rigid cord, which lies on the axis of revolution (see fig. 1.15).

A pressurized liquid is injected to force a crack to propagate between the two components at a constant pressure (see fig. 1.16). Thanks to the axisymmetric configuration around the fiber, the fiber can translate freely along the specimen's longitudinal direction during the inflation. An anti-adhering coating or tape is deposited on top of the fiber along half the specimen length to initiate an artificial crack. The pre-cracked side of the specimen is enlarged to clamp the specimen to the fluid injection system and ensure water tightness leaving the metal cord free to move axially. To avoid rubber

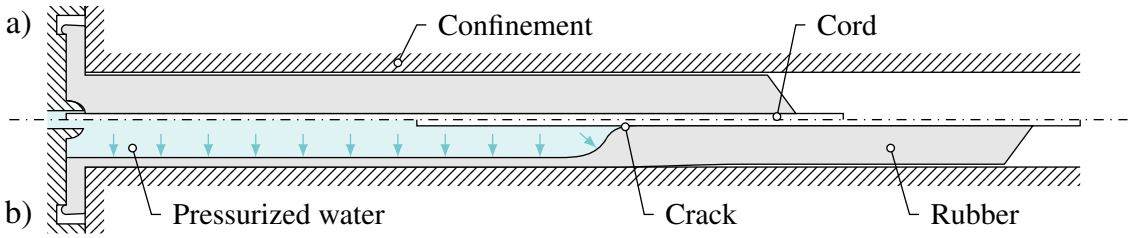

Figure 1.15: Rubber Cord Adhesion Inflation Test in a) initial configuration and b) pre-crack length inflation regime.

failure due to an aneurysm, a 5 mm inner diameter glass tube is fitted to the specimen fixture. The instability of pressure (see P_{max} in fig. 1.10) at high stretch is avoided with the confinement. RCAIT analysis assumes free longitudinal expansion of the specimen. To prevent any significant friction between the glass confinement tube and specimen rubber, silicon grease is deposited on the tube and specimen surface. The friction between the rubber and the glass tube may limit the longitudinal expansion of the specimen and consequently induce some discrepancy between the thick rubber tube model and the test condition. However, several lubricants have been tested so as to maximize the rubber longitudinal expansion [Kane, 2020].

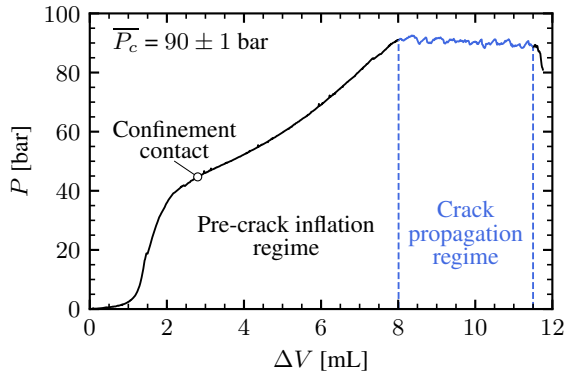

Figure 1.16: Typical inflation curve during a RCAIT experiment

Rubber sample manufacturing takes place in the Michelin research center at Ladoux. The metal cord with brass coating has a nominal diameter of 1.3mm. The cord is stored on a wire bundle, thus having a permanent curvature. The cord is straightened by a screw at each end of the specimen mold (black parts with 5 screws mold in fig. 1.17). Appropriate cleaning removes the oil from the cord. The mold itself is coated with a green anti-adhesive coating to ease sample unmolding. Crude rubber is deposited inside each cavity. All 5 cavities communicate by a rectangular cavity, where the ven-

Figure 1.17: Specimens' mold at Michelin (top), a RCAIT sample (middle) and a wire fracture surface after testing (bottom).

tilation holes are. The mold is then closed. Vulcanization happens in a hot press, with both pressure and temperature controlled. The exact rubber composition and vulcanization process parameters are not disclosed. After the test, a residual layer of rubber is typically observed on the wire.

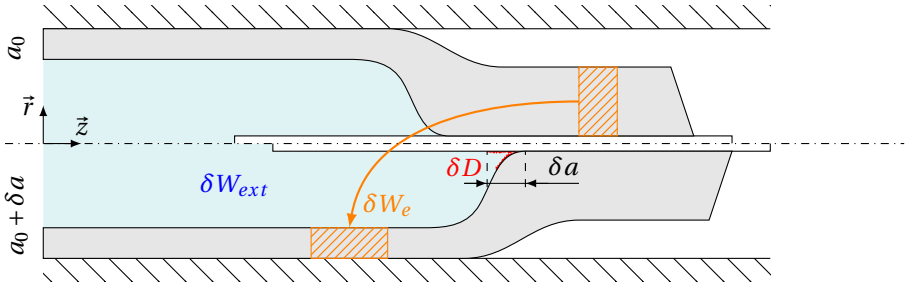

Figure 1.18: Illustration of the energy variation after a virtual crack advance.

During the test, the pressurized fluid delaminates the cord from the envelope at a constant pressure P_C. The pressure P is directly related to the strain energy release rate with an energy balance analysis (see fig. 1.18) [Kane et al., 2019] similar to the previous example on peel test. The variation of exterior work after a crack advance δa is defined in eq. 1.40 as the added volume under pressure. The volume is a hollow cylinder with an internal radius equal to the cord radius R_{cord} and an outer radius equal to the inner radius of the deformed rubber envelope r_{int}.

$$\delta W_{ext} = P\delta V = P\pi(r_{int}^2 - R_{cord}^2)\lambda_z \delta a \tag{1.40}$$

The stored strain energy corresponds to the energy stored in the section (computed from the thick tube model presented in section 1.4.1) of the detached tube of length δa :

$$\delta W_e = \int_{r_{int}}^{r_{ext}} W(r) 2\pi r \mathrm{d}r \lambda_z \delta a \tag{1.41}$$

Applying the same energy balance from section 1.4.2 gives the relation between dissipation during fracture and the energies :

$$\delta W_{ext}(\lambda_z, r_{int}, P) = \delta W_e(\lambda_i) + \delta D \tag{1.42}$$

The crack surface is cylindrical, the SERR corresponds to:

$$G = \frac{\delta D}{\delta S} = \frac{\delta D}{2\pi.\delta a.R_{cord}} \tag{1.43}$$

The contribution for the water compressibility used previously [Kane, 2020] is negligible. The resulting analytical model can predict the SERR for any given inflation pressure. With the critical pressure to propagation P_C, the critical SERR of the sample is computed (fig. 1.19)[Kane et al., 2019]. The strain energy used in the thick tube model [Skala, 1970] can have an influence on the resulting SERR if identified from standard tensile test on dumbbell specimens for instance. However, identification of the pre-inflation regime of the RCAIT with the thick tube inflation model reduces the discrepancy between strain energy forms [Kane et al., 2021].

1.5 Synthesis on the dependence of rubber-brass adhesion

The adherence between a soft elastomer and a rigid substrate is widely present in the industry. But the precise characterization of the adherence between the components is

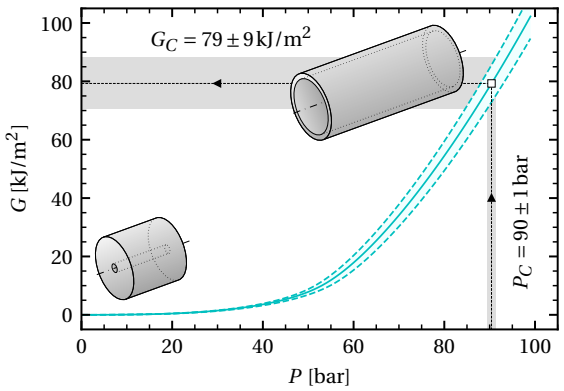

Figure 1.19: Determination of the critical strain energy release rate from the critical pressure plateau (blue shade corresponds to the standard deviation of the strain potential and grey shade corresponds to the standard deviation of the critical pressure)

still a complex task. Multiple effects are concurrent during the fracture of the interface between a rubber and a rigid substrate, difficult to deconvoluate. Given a constant interface, the main effects that can influence the apparent global dissipation during the interface crack growth between rubber and brass are :

- Crack velocity from material viscosity.
- Pre-softening from Mullins effect.
- Mode mixity from interface configuration.

The tests available to study these effects on a small radius configuration, here a steel wire cable, are not ideal. The specimen effect is difficult to suppress (pull-out) or the configuration is not feasible (peel test). The RCAIT is a singular case of blister testing, designed specifically to study the adherence of rubber to wire reinforcement. The RCAIT appears to have many advantages over the pull-out test (absence of friction, computation of G with a hyperelastic behavior) and development possibilities. In the following, multiple aspects of the test are developed to validate and demonstrate the robustness of the RCAIT results. Furthermore, the dependency of G of the rubber-brass interface is studied under different mixed-mode conditions, after pre-softening and under creep crack growth.

1.6 Proposed approach

The approach around the RCAIT presented hereafter first consolidates the previous development. The different hypotheses are validated and the methodology is improved. Then, we use the RCAIT to characterize the SERR and its variation during interface crack growth. The variation is observed under different crack mode mixity, crack velocities, or softening levels to evaluate the role of each dissipation mechanism on the global dissipation.

Improving the methodology

The first part of the work is to improve and validate the means of computation of the global G during crack growth. Early work of [Kane et al., 2019, Kane et al., 2020, Kane et al., 2021] pave much of the initial analyses, and further development is built upon. The chapter 2 improves the SERR computation robustness and reliability with marker tracking and crack growth monitoring. The marker displacements and the measure of axial stretch is then used in all further analyses. The stored strain energy during the propagation is now identified directly during the test, in a homogenous region without boundary or system compliance effects. The addition of a measure of contact pressure between the rubber envelope and the confinement tube (in chapter 4) gives a validation of the identification. Furthermore, a simpler graphical method is proposed and corresponds well with the improved analytical method.

Verifying the hypothesises

A finite element (FE) analysis is conducted to verify the analytical model and the hypothesis used in the energy balance in chapter 3. The FE model is predictive and allows the validation of the analytical energy balance. The FE model also allows for verification of the reliability of the transition zone measurement, given by the marker tracking technique. An obstacle to further analysis is the control of friction between the sample and the confinement. Experimental, analytical, and numerical works permit validation of the lubrication condition in the chapter 4. The predictive FE model reproduces the experiments and proves the robustness of the steady-state crack growth hypothesis and inflation tube hypothesis. With the validation of the basic computation of SERR in the classic RCAIT, further developments are possible.

Quantifying the different dissipations

The literature on the crack growth interface fracture shows that the main dissipative mechanisms are rate dependent and their relative contributions depend on the mode mixity condition and, from the earlier studies on rubber solids, the pre-softening.

To study the effect of crack mode-mixity on dissipation, a novel experimental setup is developed with a dual actuator, presented in chapter 5. The analytical model to compute the SERR is extended to the inflation-tension condition. The experimental results exhibit a strong dependence on the mode mixity resulting in loading conditions. A first numerical model tries to correlate the macroscopic mixed load to the crack tip morphology and a parallel is drawn with the peel angle. Investigating the effect of pre-softening on the adhesive performance of a soft-rigid system is challenging and has not been reported in the literature. A novel method is proposed to soften the elastomer before conducting the adherence test in Chapter 6. An energy balance analysis is proposed to confirm the softening of the sample and to model the effect of softening on the global G. Further works on viscous dissipation are started with the slow crack growth bench in the chapter 7. A first evolution of the strain energy release rate with crack velocity is reported. With the different results of the 3 methods (mixed-load, pre-softening, and delayed fracture), the variation range of the global SERR permits a first idea of a possible partitioning of the dissipation during interface crack growth.

Refined metrology 2

P.-Y. Corbel, J. Jumel, K. Kane, A. Mbiakop-Ngassa
"Refined crack propagation methodology and energy balance analysis in the Rubber Cord Adhesion Inflation Test"
published in International Journal of Adhesion and Adhesives, vol. 119 (2022) 103243

The Rubber Cord Adhesion Inflation Test (RCAIT) has been recently introduced to characterize the bond quality between coated steel wires and rubber as used in tire applications. In this experiment, a pressurized fluid is used to initiate and propagate a delamination along the reinforcement. A constant pressure is measured during the crack propagation regime so that using adequate energy balance analysis, the critical Strain Energy Release Rate (SERR) can be determined. Due to the axisymmetric nature of the specimen, the crack tip is not visible nor is there other information that would ease the analysis of the fracture process. Then, new experimental developments and experimental data reduction techniques are introduced to demonstrate the reliability of the RCAIT.

2.1 Introduction

Ensuring strong adhesion between elastomers and metal parts is a key issue in many applications such as structural bonding, anti-vibration dampers, sealing, pipes, or tires. A large variety of geometrical configurations and products can be found whether the elastomer is reinforced with fiber, cable, or fabric is used to join two solids parts. In either case, reproducible and durable metal/elastomer interface properties are crucial to guarantee the reliable mechanical performance of the system. Depending on the application and adhesive system, various bonding processes are used involving

a combination of physical, chemical, or mechanical adhesion mechanisms. The development of new bonding procedures with optimized performances and compatible new sustainability and environmental regulations is then a complex and costly task due in particular to the need for an extensive characterization campaign.

Numerous test configurations have been proposed for characterizing adhesion between soft and rigid materials. Butt joints, TAST, or DCB specimens are generally used to evaluate the overall mechanical performances of adhesive joints whether they are hyperelastic or not. A large variety of peel [ASTM D1781, 2012, ASTM D429, 2014, Cook et al., 1997] and blister [Dannenberg, 1961, Williams, 1997] tests are available to characterize the adhesion between very flexible coating, layers or adherent bonded to rigid or flexible substrates in planar configuration. However, fewer test configurations are applicable to characterize the adhesion between elastomer and their reinforcements. For fiber, cable, and wire they are derived from pull-out configurations commonly used for fiber matrix adhesion characterization in composite materials or metal rods in concrete or timber. For tire applications rubber, cord adhesion is evaluated using the standard procedures [ASTM D1871, 2014, ASTM D2229, 2014] as initially proposed by A. Gent [Gent et al., 1981]. The test implementation is straightforward but its rigorous analysis may be rather tedious. Indeed, the fiber/rubber interface loading condition depends on specimen geometry, components' mechanical properties, and other experimental conditions. Recently an alternative adhesion test protocol has been proposed [Kane et al., 2019, Kane et al., 2020] derived from the confined pressurized blister test [Chang et al., 1989], for measuring the critical Strain Energy Release Rate (SERR) needed to separate metal cords from rubber. During this experiment, referred to as the Rubber Cord Adhesion Inflation Test (RCAIT) a pressurized fluid is injected between the cord and its cylindrical rubber envelope leading to progressive decohesion and stable crack propagation. The specimen is installed in a confinement tube to prevent rubber failure due to aneurysms and force the crack to propagate along the specimen axis. For a quantitative evaluation of the fracture energy of the system, a global energy balance analysis is proposed which is very similar to the one performed for more conventional peel tests. Then using simple experimental estimates of the crack propagation length, measured fluid pressure and analytical modelling of Thick Rubber Tube Inflation [Kane et al., 2019, Kane et al., 2020, Kane et al., 2021] the critical SERR can be determined.

In this paper, a marker tracking technique is exploited to achieve a more reliable

evaluation of the crack propagation and rubber inflation conditions. Using this additional information, the self-similar nature of the crack propagation can be assessed as other experimental conditions. In particular, additional experimental data are obtained to validate the analytical model proposed previously for sizing the specimen and analyzing the experimental results. Using the marker monitoring technique, the longitudinal expansion can be monitored together with the inflation pressure and inner volume expansion in the pre-crack region of the specimen. These experimental data are fitted with the thick inflation rubber tube model. An alternative experimental data reduction technique is proposed to evaluate the critical SERR. RCAIT tests are then performed on a set of 5 specimens having common experimental conditions. This series of tests and comparison of data reduction techniques clearly demonstrate the reliability of the RCAIT for measuring quantitatively the rubber /metal cord interface adhesion. Both methods lead to very similar results despite they are funded on distinct assumptions approaches. Consistency between Linear Elastic Fracture Mechanics and Global energy balance suggests confined/reduced plastic/damage zone is developing ahead of the crack tip. The analytical and the alternative model shows similar results while having one different hypothesis on the propagation. It demonstrates the validity of the virtual crack extension of the analytical model and may indicate a small damage dissipation during propagation.

2.2 Presentation of the RCAIT

The RCAIT has been proposed to assess the adhesion strength between a rigid fiber and an elastomeric matrix. Similarly to the blister test [Dannenberg, 1961, Williams, 1997], a pressurized liquid is injected to force a crack to propagate in between the two components (Fig. 2.1). Thanks to the axisymmetric configuration around the fiber, the fiber can translate freely along the specimen's longitudinal direction during the inflation. An anti-adhering coating or tape is deposited on top of the fiber along half the specimen length to initiate an artificial pre-crack. The pre-cracked side of the specimen is enlarged to clamp the specimen to the fluid injection system and ensure water tightness leaving the metal cord free to move axially. To avoid rubber failure due to an aneurysm, a 5 mm inner diameter glass tube is fitted to the specimen fixture. RCAIT analysis assumes free longitudinal expansion of the specimen. To prevent any significant friction between the glass confinement tube and specimen rubber, silicon grease

is deposited on the tube and specimen surface. The friction between the rubber and the glass tube may limit the longitudinal expansion of the specimen and consequently induce some discrepancy between the thick rubber tube model and the test condition. However, several lubricants have been tested to maximize the rubber longitudinal expansion. The measured elongation and inner volume expansion values agree with the model which tends to validate the current assumption. However, some further investigations should be conducted to further investigate crack propagation conditions in case of more pronounced friction or adherent contact.

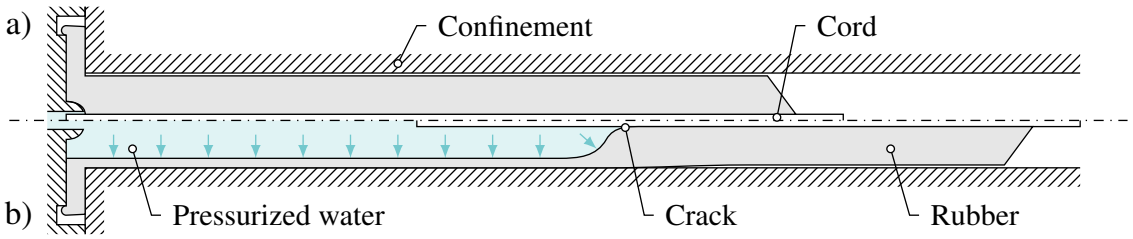

Figure 2.1: Rubber Cord Adhesion Inflation Test in a) initial configuration and b) pre-crack length inflation regime.

The rest of the test setup (Fig. 2.2) consists of a hydraulic circuit connecting the specimen fixture to a syringe used to inject the fluid at a constant volume rate. The syringe plunger is fitted to a tensile test machine driven at a constant traverse displacement rate. The volume of fluid injected into the gap is calculated from the crosshead displacement of the tensile test machine and plunger radius. The compliance of the whole system is negligible compared to that of the specimen, making this calculation acceptable. At the same time, the fluid pressure is measured using a Swagelok® Model S Transducer. Ball valves are installed in the circuit to purge any trapped air in the pipes and fill it with the injection fluid. For all the experiments presented in this work, tap water was used as the injection fluid.

Fig. 2.3 presents a typical pressure evolution recorded during an RCAIT using a 2 ml/min injection rate. The curve can be divided into three regimes. In the first regime, a marked nonlinear pressure-volume evolution is observed, corresponding to the inflation of the pre-cracked part of the rubber. In this regime, the specimen first expands radially and axially until it touches the confinement tube (Confinement contact). Once the confinement contact is achieved, radial expansion of the rubber tube is restricted at the outer circumference. The specimen therefore expands axially, and radially from the inside only. The second regime starts when a critical pressure is reached, the inter-

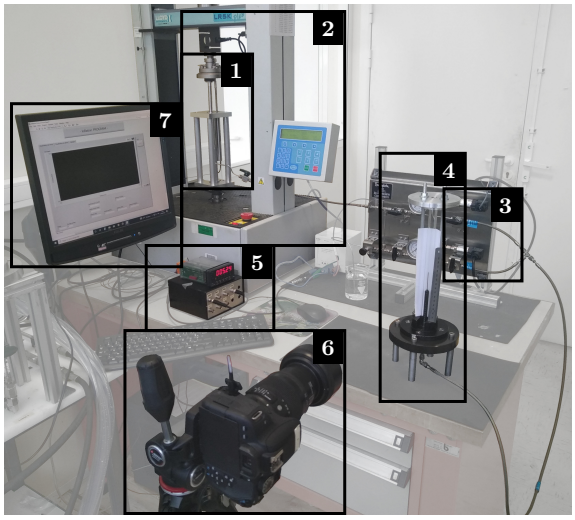

Figure 2.2: Picture of the experimental setup. 1) 20 ml stainless steel high-pressure syringe beside a 50 mm LVDT displacement sensor; 2) 5 kN tensile test machine; 3) hydraulic circuit with manometers and pressure transducers (16 bar and 250 bar); 4) RCAIT; 5) data acquisition device; 6) reflex camera; 7) data acquisition system.

facial separation initiates (ΔV =8. ml) and propagates along the cord. A stationary pressure during propagation, bar, is recorded while the fluid is injected. Specimen shape at the crack tip vicinity remains the same so that self-similar crack propagation regime seems a reasonable assumption for later analysis. At last, a significant decrease in pressure correlates with the crack approaching the specimen end (ΔV =11.5 ml). Dynamic propagation is finally observed with the cord being projected out of the rubber envelope leading to total specimen failure.

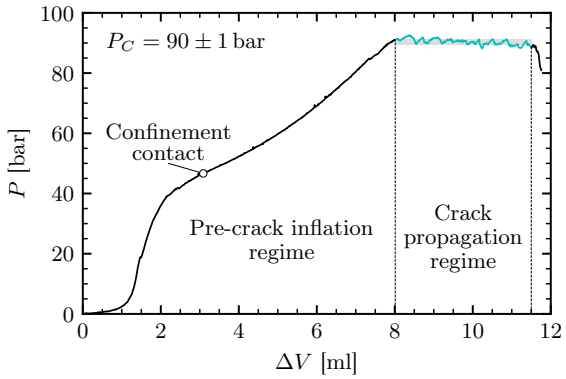

Figure 2.3: Typical fluid pressure versus injected fluid volume evolution during RCAIT.

In the experiments presented hereafter, the specimens are obtained by placing crude rubber mix around a 0.65 mm radius steel cord in a mold. Natural rubber filled with

60 phr of carbon black and 7 phr of sulfur is used and will be referred to as Mix A. After curing, cylindrical specimens having w_0 =4.7 mm outer radius and 100 mm length are obtained with the cord being coincident with the cylinder axis. Details of the rubber curing time and temperature are not mentioned here since they are subject to confidentiality. The steel cord is obtained after multiple wire-drawing steps to get the final diameter. A brass coating is deposited before the last drawing step. During the vulcanization process, a strong rubber-metal interface is obtained attributed mainly to the formation of CuxS covalent bonds [van Ooij, 1977]. 50% of the steel cord length is covered with a PTFE tape before rubber deposition to prevent adhesion, thus forming a 50 mm long artificial de-cohesion length a_0.

In previous contributions, the critical SERR driving the crack propagation has been determined by balancing the work provided to the system through pressurized fluid injection, and the energy stored in the inflating the rubber tube and assuming self-similar propagation regime [Kane et al., 2019, Kane et al., 2020, Kane et al., 2021]. Analytical modeling of thick hyperelastic tube inflation is needed to evaluate the elastic potential energy. However, using additional experimental data, alternative evaluation of critical SERR can be derived and compared.

2.3 Implementation of marker tracking technique

In the following section, a simple marker tracking monitoring technique is implemented for measuring the rubber longitudinal extension, λ_z, and monitoring the crack propagation during the test.

Several silver dots are drawn every ca. 5 mm along the specimen length using Schmidt® 700 Silver pen (Fig. 2.4). Markers are visible through the confinement tube and lubricant and are both transparent. Optical distortion is considered negligible here considering the required precision and overall dimensions. A CANON EOS 800D Camera is used to acquire images of the specimen. Picture acquisition is triggered by the tensile testing by machine so that pressure and traverse measurements data are synchronized.

A Python script using image processing algorithms from the SciKit Image library is used to determine the markers' position in each image. Then the algorithm determines their relative displacement with respect to their initial location along the cylinder axis in pixels. Keeping the marker intact during the test is rather difficult due to the

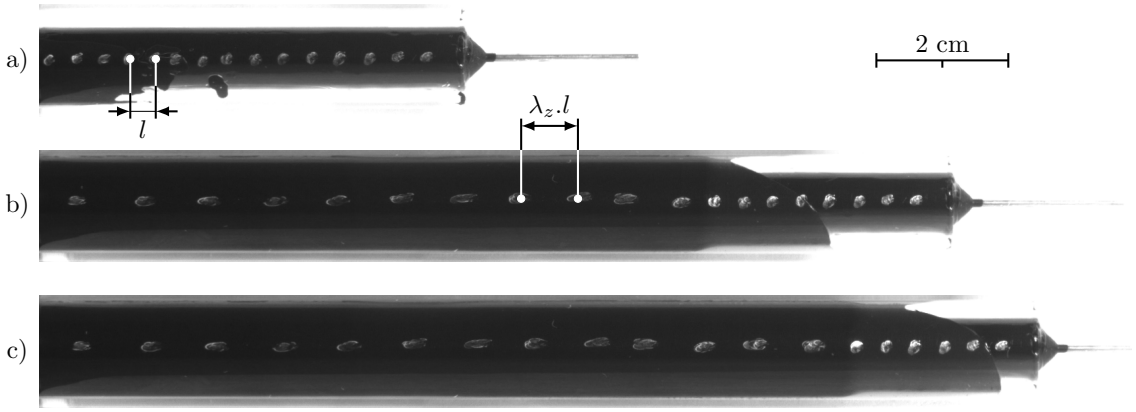

Figure 2.4: Sequence of images showing the silver markers displacement on the rubber sample at three stages of the inflation test: a) initial b) inflation regime and c) crack propagation regime.

experimental conditions. Then the marker tracking algorithm needs more effort. Indeed, bubbles, reflection and marker fading increase the difficulty of finding the proper marker position, motivating the development of an improved version of the marker tracking algorithm.

Firstly, to mitigate the effect of exposition and marker fading, the picture of the whole specimen is segmented into multiple sub-pictures, each one containing only one marker. Image processing is then locally applied to each sub-picture. As the marker position is not known a priori, the segmentation is based on the previous marker position. After the visual assessment, results are found satisfying providing the picture acquisition rate is sufficient to keep each marker in the control window.

Secondly, the image processing mainly uses morphological filtering [van der Walt et al., 2014] (erosion, dilation, opening). Working with marker morphology instead of brightness increases the robustness of bubbles and grease refraction. Nonetheless, if a marker is not detected in a sub-picture, the image processing parameters can be manually adjusted.

A ruler is placed aside from the tube before the experiment to convert pixel data into millimeter values. From the evolution of the position between markers divided by their initial distance, the rubber longitudinal elongation λ_z during the test is obtained.

2.3.1 Rubber behaviour identification

For accurate determination of the critical SERR the hyperelastic tube inflation response should be properly described whether analytical /numerical modeling is involved or it

is based on only experimental data. Indeed, a major part of the energy supplied by fluid injection is stored and dissipated by the tube inflation itself rather than by interface de-cohesion. The first regime of the RCAIT, prior crack propagation, can be used to analyze the tube inflation response. Indeed, as seen in Fig. 2.4, several markers are visible along the pre-cracked part of the specimen. The inflation process can then be represented either in terms of $P(\Delta V)$ or $P(\lambda_z)$ evolution the latter being less susceptible to imprecision since the elongation is directly measured on the specimen far from the crack tip position and specimen attachment end while ΔV is a global quantity whose measure could be imprecise due to overall system compliance and possible air entrapped in the hydraulic circuit. The discrepancy between these two quantities should be evaluated for proper critical SERR determination. Considering incompressible rubber behavior, the inner radius of the rubber envelope during the confined expansion regime can be determined from initial specimen geometry and longitudinal elongation to be correlated with experimental ΔV measurement. The measured axial elongation λ_z, the radial and angular elongation can be fully described across the rubber wall thickness using the previously developed analytical model [Kane et al., 2019]. Using developments of D.P. Skala [Skala, 1970], assuming incompressible material behavior ($\lambda_r \lambda_\theta \lambda_z = 1$) and axisymmetric configuration, the circumferential elongations are given by equation 2.1.

$$\lambda_\theta = \frac{r}{r_0} = \sqrt{\frac{\lambda_z^{-1} c r^2}{c r^2 - 1}} \tag{2.1}$$

r is the radial position in the deformed configuration r_0 is the radial position in the initial configuration and c is an integration constant which can be determined from the boundary conditions. During the confined regime, once the contact between the rubber envelope and the glass tube is established, the outer rubber tube radius is known and is equal to the inner radius of the confinement tube R_{conf}, resulting in equation 2.2 [Kane et al., 2019].

$$c = \frac{\lambda_z}{\lambda_z R_{conf}^2 - w_0^2} \tag{2.2}$$

with w_0 being the initial outer radius of the rubber envelope. Then, analytical expression of the variation of inner radius r_i, during the confinement stage is obtained on equation 2.3 [Skala, 1970].

$$r_i = \sqrt{\frac{v_0^2}{\lambda_z} + \frac{1}{c}} = \sqrt{\frac{\lambda_z R_{conf}^2 + v_0^2 - w_0^2}{\lambda_z}} \tag{2.3}$$

with v_0 is the initial inner radius. Finally, the variation of the inner volume of the tube occupied by the pressurized fluid is determined on equation 2.4.

$$\Delta V(\lambda_z) = \pi(r_i^2 - v_0^2)a_0\lambda_z = \pi a_0\left(\lambda_z R_{conf}^2 + v_0^2(1-\lambda_z) - w_0^2\right) \tag{2.4}$$

where a_0 corresponds to the length of the artificial pre-crack.

The comparison between the analytical evaluation of ΔV and the experimental measurements are presented in Fig. 2.5. The comparison is valid only during the confined regime, therefore the initial evolution is not relevant here. Additionally, as was mentioned before, uncertainties due to entrapped air and improper boundary conditions are expected especially during the unconfined inflation stage. Thus, the analytical curve is translated along the ΔV axis to match the observed inflation curve. After this correction is performed, the evolutions are found very similar. Thus, the transition between the unconfined and confined regimes becomes identifiable thanks to the evolution shape given by the analytical solution. The volume injected to reach the confinement contact is between 2.5 and 3 ml.

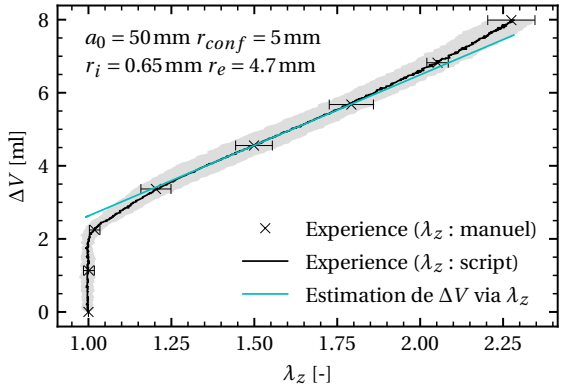

Figure 2.5: Comparison of the evolution of injected volume with axial elongation measured experimentally and estimated with axial elongation by analytical solution.

The $P(\Delta V)$ and/or $P(\lambda_z)$ evolutions recorded during the inflation regime prior to crack propagation onset can be used to identify the rubber behavior by fitting the experimental evolution with the results obtained with the thick wall cylinder inflation model solution [9,10,12,15]. To make the elongation measurements more robust, 5 elongations are measured along the pre-crack length making use of 6 markers observed in this area. Mean and standard deviation are computed at a given pressure level and are shown in Fig 2.6a. The computed elongations are similar whether they are computed by picking manually the maker position on images or using an auto-

matic marker tracking procedure. As discussed before the initial $P(\Delta V)$ evolution is truncated to cope with imprecise ΔV evaluation prior to inverse identification.

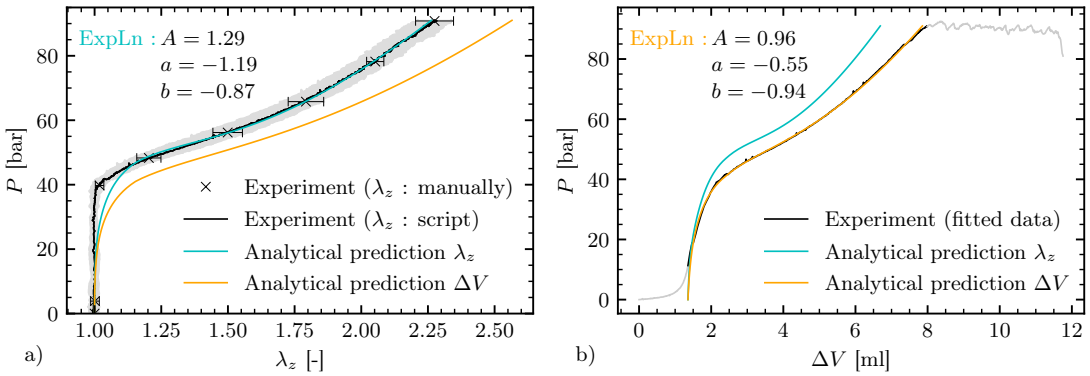

Figure 2.6: Comparison of experimental and analytical predictions fitted on axial stretch-pressure evolution on a) and on volumetric-pressure evolution on b).

The least-square minimization procedure is used to identify the rubber behavior using the standard Levenberg-Marquart algorithm. The cost function minimizes the square difference between analytical prediction and experimental data. The Exp-Ln strain energy [Khajehsaeid et al., 2013] presented in equation 2.5 is used here to describe the rubber hyper-elastic behavior.

$$W = A\left[\frac{1}{a}\exp(a(I_1-3)) + b(I_1-2)(1-\ln(I_1-2)) - \frac{1}{a} - b\right] \tag{2.5}$$

A, a and b are the material parameters and I_1 the first stretch invariant. Results of both inverse identification procedures using $P(\Delta V)$ and $P(\lambda_z)$ are presented in Fig. 2.6. The Exp-Ln model can represent independently these two evolutions but leads to distinct material parameter values.

Again, this slight discrepancy is attributed to improper boundary conditions for the thick rubber tube inflation model which is not capable of predicting the exact ΔV evolution during the inflation regime due to improper boundary conditions near the initial crack tip position and in the clamps. Thus, the specimen seems more compliant and a higher axial elongation is predicted compared to the axial stretch measured. A fit directly on $P(\lambda_z)$ leads to a better prediction. It is also more robust because the pre-crack length a_0 is not needed for the computation, contrary to the volumetric fitting, and the strain state is homogeneous in the measured zone. In the following, the analysis based $P(\lambda_z)$ on will be used for evaluating the energy stored by the tube inflation process.

2.3.2 Crack monitoring

After a critical pressure value is reached, the rubber /metal interface fails and a stable crack propagation regime is observed while the fluid pressure remains constant. Such a failure process is driven by the critical SERR, G_C. To evaluate this material parameter from the test data, the crack propagation should be monitored during the experiment in order to evaluate the newly created fracture surface $2\pi r_c \Delta a$. However, contrary to other more conventional fracture experiments, the crack tip is not visible during the test due to the axisymmetric nature of the specimen and the opaque rubber envelope. Therefore, an indirect crack propagation length estimate is proposed making use of the markers tracking technique again.

As presented in Fig. 2.7, the longitudinal elongation of the rubber tube is first measured in the pre-crack region of the specimen (length of a_0). After the initial inflation regime, λ_z remains constant at $\lambda_z(0)$ in the cracked part since fluid pressure is also constant during propagation. An additional marker p_t corresponding to the specimen tip is also measured with the marker tracking technique (Fig. 2.7. Considering the total specimen length is L and crack length is $a = a_0 + \Delta a$, and considering the longitudinal elongation abruptly changes from λ_z to one at crack tip position we have the equation 2.6.

$$p_t = L + (a_0 + \Delta_a)(\lambda_z(z) - 1) = L + a_0(\lambda_z(z) - 1) + \Delta p_t \tag{2.6}$$

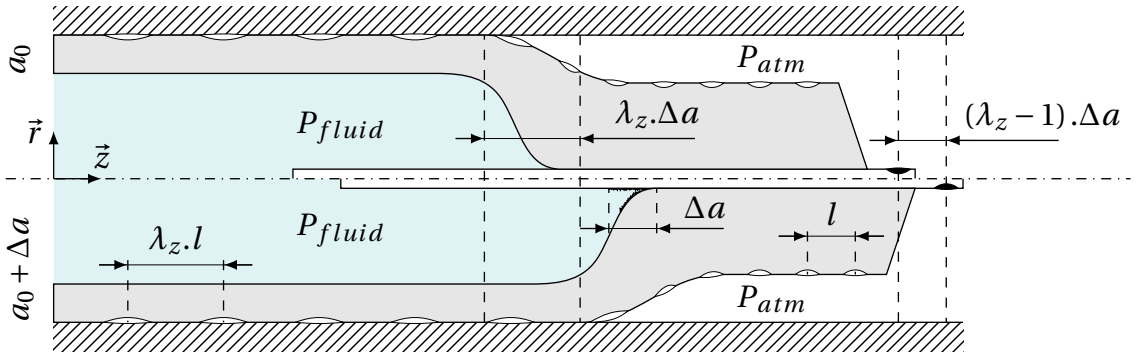

Figure 2.7: Illustration of the crack propagation in two states: before and after propagation over a distance

From the equation 2.6 the instant crack propagation length is simply obtained with the equation 2.7.

$$\Delta a = \frac{\Delta p_t}{\lambda_z(0) - 1} \tag{2.7}$$

2.3.3 Process zone investigation – self-similar regime validation

The marker monitoring technique may be used for validating the self-similar crack propagation regime assumption. This hypothesis should be assessed for rigorous G_C evaluation from energy balance analysis. For such a crack propagation regime to be observed the specimen deformation in the crack tip vicinity should remain the same for all crack tip positions. The equation 2.7 can be refined into equation 2.8 considering the exact longitudinal extension distribution along the specimen to estimate the instant marker position, p, whose initial location is p_0.

$$p = \int_0^{p_0} \lambda_z(z)\mathrm{d}z \tag{2.8}$$

In equation 2.8, the boundary condition at the clamping side is not properly described. Additionally, capturing the longitudinal extension distribution might be cumbersome so an indirect approach is preferred assuming a self-similar propagation regime again. During the only crack propagation regime, marker displacement Δp, is measured rather that the absolute position, resulting equation 2.9.

$$\Delta p = p - p_0 = \int_0^{p_0} (\lambda_z(z) - 1)\mathrm{d}z \tag{2.9}$$

Considering self-similar propagation regime and as observed on Fig. 2.7, $\mathrm{d}z$ can be replaced by Δa in equation 2.8 such that the marker relative displacement during the crack propagation regime can be determined with the equation 2.10.

$$\Delta p(p_0, a_0, \Delta a) \approx \lambda_z(0)\Delta a - \int_{p_0-\Delta a}^{p_0} (\lambda_z(z, a_0)\mathrm{d}z \tag{2.10}$$

Then the longitudinal elongation evolution can be obtained from the marker displacement monitoring with the equation (11).

$$\frac{\mathrm{d}}{\mathrm{d}\Delta a}\Delta p(p_0, a_0, \Delta a) \approx \lambda_z(0) - \lambda_z(p_0 - \Delta a, a_0) \tag{2.11}$$

An illustration of the full presentation of marker tracking monitoring is presented in Fig 2.8. The results are consistent with the initial simplified analysis and equation 2.7 since for all markers initially deposited on the bonded part of the specimen far from the initial crack tip position a linear evolution of marker displacement is observed. The same slope is observed for all markers equal to $\lambda_z(0) - 1$. Once, the marker has reached the fully cracked area far from the crack tip, the stationary marker position is reached

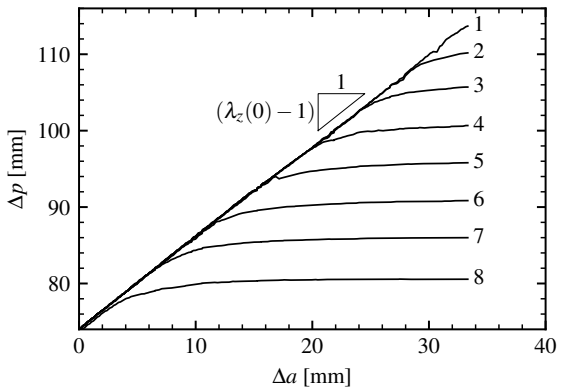

Figure 2.8: Evolution of the displacement of each marker with the crack propagation length.

equal to $(\lambda_z(0)-1)p_0$. These two independent measurements allow consistent evaluation/validation of $\lambda_z(0)$, which is fundamental for accurate determination of crack propagation Δa.

Finally, the transition region between the cracked and bonded length, also designated as the "process zone", is visible in Fig 2.8 since a smooth transition is observed between linear and stationary marker position evolution. The process zone extent is ca. 12 mm long, this value is rather reproducible for all markers. For a more precise evaluation of the zone extend, a "master curve" is obtained by applying an offset (p_0-a_0) along the X axis and $(p_0-a_0)(\lambda_z(0)-1)$ along the Y axis. Then, after reorganizing and smoothing the resulting curve on Fig. 2.9, equation 2.11 is applied to evaluate the distribution λ_z along the specimen.

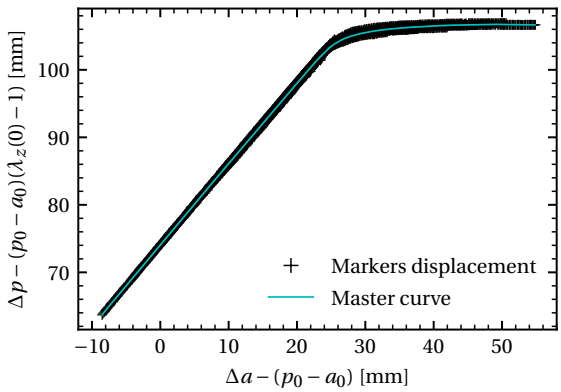

Figure 2.9: Illustration of markers' displacement offsetting and the resulting master curve.

Fig. 2.10 presents the computed axial elongation distribution in the process zone.

The rapid increase at 23 mm reflects the singularity of displacement caused by the crack nearby. Then, the axial elongation reaches gradually the plateau at $\lambda_z(0) = 2.21$

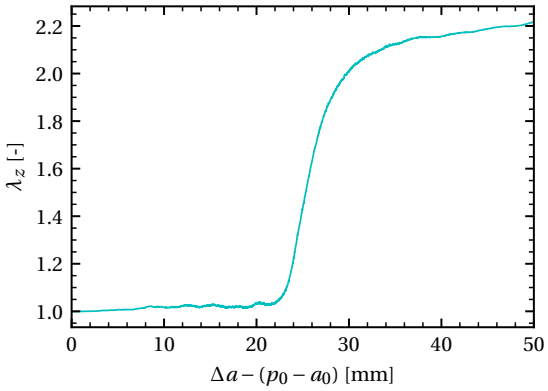

Figure 2.10: Axial elongation variation in the process zone at the crack tip.

2.4 Robust determination of critical SERR, global vs analytical methods comparison

So as for more classical peel test experiments, G_C evaluation from RCAIT relies on simple energy balance analysis between the work provided by the injection of a pressurized fluid, the potential energy stored in the inflated rubber envelope, and energy dissipated by damage development and crack propagation. Initially [Kane et al., 2019], a semi-analytical model was used to describe the hyperelastic tube inflation and evaluate its contribution in the global energy balance. Application, of such model, is also presented in section 2.3.1 to evaluate the $P(\Delta V, \lambda_z)$ evolution during the pre-crack regime. However, this method should be assessed by comparison with alternative measurements since model identification, boundary conditions specimen geometry may suffer from uncertainties that are susceptible to propagating to the estimate of G_C. Thus, in the following section, a graphical approach is proposed exploiting only the inflation pressure-volume variation curve.

2.4.1 Global evaluation of critical SERR

The graphical methods to evaluate the critical SERR make use of a conventional representation of the energy balance analysis of crack propagation experimental in the

$P(\Delta V)$ plane to evaluate the various energy contributions (Fig. 2.11). To evaluate energy dissipated, D, due to the crack propagation, the classical energy balance is performed with equation 2.12.

$$D = W_{tot} - E_{def} \tag{2.12}$$

With E_{def} being the stored strain energy during the whole test. E_{def} is obtained by integrating the $P(\Delta V)$ curve in the pre-crack inflation regime and multiplying it to model the strain energy stored at the end of crack propagation. The total work W_{tot} is obtained by integrating the total inflation curve (Fig. 2.11a).

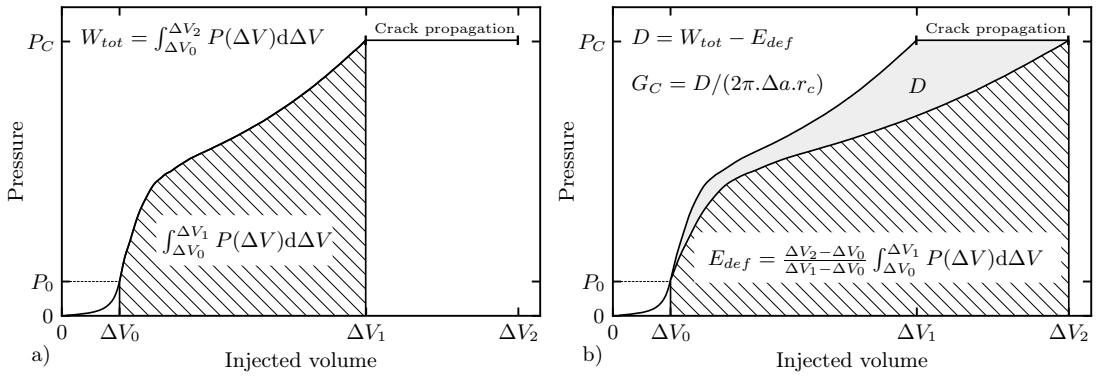

Figure 2.11: Two-step estimation of the energies with the areas under the inflation curve. On a), the strain energy stored during the pre-crack inflation regime corresponds to the hatched area under the inflation curve. This strain energy area is dilated along the injected volume axis on b) to model the strain energy stored E_{def} after crack propagation. The subtraction of the total area under the inflation curve by the scaled strain energy shows a shaded area corresponding to the energy dissipated by the crack propagation D.

To evaluate the stored deformation energy in the specimen at the end of the crack propagation regime, a new "virtual" inflation curve by plotting $P\left(\frac{a_0 + \Delta a}{a_0}\Delta V\right)$ considering little effect of the specimen ends so that the secant stiffness of the specimen is simply proportional to the crack length, resulting equation 2.13.

$$E_{def} = \left(\frac{a_0 + \Delta a}{a_0}\right) \int_0^{\Delta V_1} P(u)\mathrm{d}u \tag{2.13}$$

The volume injected is proportional to the length of inflated rubber, thus the equation 2.13 is similar to equation 2.14.

$$E_{def} = \frac{\Delta V_2 - \Delta V_0}{\Delta V_1 - \Delta V_0} \int_{\Delta V_0}^{\Delta V_1} P(\Delta V)\mathrm{d}\Delta V \tag{2.14}$$

It corresponds to the dilatation of the area under the initial inflation curve below ΔV_1 up to the final volume ΔV_2 in Fig. 2.11b. A small injected volume under ΔV_0 is censored as it reflects experimental artifacts, such as air bubbles trapped in the injection circuit. This volume is not represented by the previous analytical solution, illustrated in Fig 2.6b, where pressure rises abruptly. The injected volume above ΔV_2 corresponds to the unstable propagation when the crack reaches the end of the specimen.

Finally, the critical SERR is obtained by dividing the total dissipated energy D by the newly created crack surface, $2\pi r_c \Delta a$, with r_c being the cable radius. The crack propagation Δa is known at any injected volume thanks to the crack monitoring technique presented previously.

2.4.2 Experimental results

To demonstrate the robustness of the test protocol and data reduction techniques for G_C evaluation, five specimens of the same batch are tested under the same conditions and the data reduction techniques presented above and in [Kane et al., 2021] are used. Fig. 2.12 shows the experimental inflation curves of the five samples for identical test conditions. The evolution is very similar for all these tests. The corresponding critical pressure values during the crack propagation are reported in Fig 2.13. The mean pressure during propagation ranges between 89.7 and 92.6 bar. The standard deviation during the propagation (error bar for each test) is similar to the deviation between the 5 experiments mean critical pressure (error bar for "Mean") demonstrating the test's reproducibility.

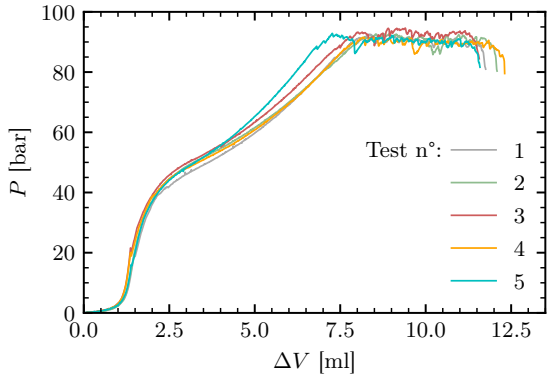

Figure 2.12: Experimental inflation curves for an injection flow of 2 ml/min.

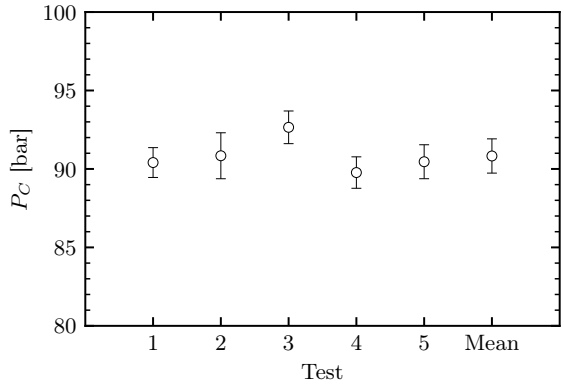

Figure 2.13: Comparison of critical pressures at crack propagation for an injection flow of 2 ml/min.

Fig. 2.14 shows the results of G_C evaluations from the global method presented above and the analytical method [Kane et al., 2021] with $P(\lambda_z)$ fitting for all five tests. The two methods give similar results, with a good consistency on the experimental campaign. The standard deviation on the total mean of critical SERR on the campaign is narrower than each test taken alone. The analytical method gives a critical SERR at 79.2 kJ/m² and the graphical method, at 84.6 kJ/m². Fundamentally, both methods are very similar but the graphical method uses the raw $P(\Delta V)$ while in the semi-analytical method, a hyperelastic strain potential and thick inflation tube model is used to fit the $P(\lambda_z)$ evolution and obtain an analytical expression of G_C. Then, as long the fitting of the $P(\lambda_z)$ curve is good, no discrepancy is observed between both methods considering the standard deviation on G_C.

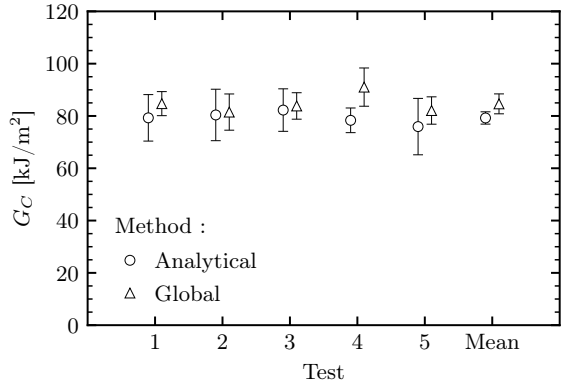

Figure 2.14: Comparison of analytical and global method prediction of the critical strain energy release rate on the experimental campaign.

2.5 Conclusions

In this article, RCAIT has been revisited by introducing supplementary analysis that enriches the available experimental data to validate the test conditions and the assumptions on which are founded the data reduction methods for G_C evaluation. In particular, a marker tracking technique is introduced for fine monitoring of crack propagation, and fluid volume injection and to assess the self-similar nature of the crack propagation process. It also enables to characterization of the rubber tube inflation process by measuring $P(\Delta V)$ and $P(\lambda_z)$ evolution and then evaluating in-situ the rubber mechanical behavior itself. Additionally, with this marker monitoring technique, the evolution of longitudinal elongation of the rubber envelope along the process zone can be determined for further analysis of the failure process. Finally, a direct evaluation of critical SERR from the measured $P(\Delta V)$ curve is proposed and compared with previous data reduction methods. A batch of five identical specimens is tested to evaluate G_C with the two methods.

All results are consistent, a very small standard deviation is observed on the critical pressure recorded during the crack propagation regime and associated critical SERR. The two methods share the assumption of self-similar propagation. However, the analytical method uses a virtual crack extension technique. The technique assumes the development of a process zone ahead of the crack tip does not significantly modify the evaluation of specimen compliance. Meanwhile, the global graphical method energy balance analysis is directly obtained from the analysis of the $P(\Delta V)$ curve. No hypothesis on the nature and effect of the dissipative mechanisms on the structural response of the specimen is needed in contrast to the analytical method. This may indicate that the extend of the process zone size ahead of the crack tip is limited with respect to other dimensions of the specimen.

The results demonstrate the reliability of the RCAIT for characterizing interface toughness between rubber and wire/cable reinforcement through precise in-situ control of test and crack propagation conditions. This original test protocol has now been demonstrated to be a seducing alternative to more traditional peel tests for characterizing metal/rubber interfaces and could also be implemented as an alternative or complement to more industry-oriented tests such as the H-test for instance. If G_C measurements have proven to be reliable, so additional investigations are now necessary to investigate with more detail the local mechanisms in the process zone region con-

trolling the damage and crack propagation condition. Such analysis is now in progress trying in particular to evaluate the mode mixity conditions.

Transient crack growth model 3

P.-Y. Corbel, J. Jumel
"Simulation of fluid driven crack propagation along metal/elastomer interface - Application to the numerical analysis of the Rubber Cord Adhesion Inflation Test"
published in Mechanics of Materials, vol. 185 (2023) 104774

The Rubber Cord Adhesion Inflation Test (RCAIT) has been proposed as an alternative technique to more standard pull out protocols such as H, T, or pull-out tests for characterizing the adhesion between cord/cable reinforcement and rubber. During this test, a fluid is injected in between a wire and a rubber cylindrical envelope to provoke the interface separation once a critical pressure is reached. A simple energy balance analysis is used to evaluate the critical strain energy release rate, G_C, which drives the crack propagation from measurable quantities. However, some assumptions should be assessed to ensure reliable G_C evaluation. Then, a predictive finite elements simulation of the RCAIT is proposed to simulate the fluid driven crack nucleation and propagation process along the rubber cord interface. These results are compared with the ones obtained from the RCAIT simplified analysis.

3.1 Introduction

Elastomers are used for manufacturing a large variety of parts such as antivibration components, gaskets, transmission belts, tires, or pipes. To obtain the desired mechanical performances composite systems are often used by incorporating particles, cords,

cable, mesh, or fabric into an elastomer matrix. However, as for all composite materials, the adhesion strength between matrix and reinforcement is a key parameter controlling the overall initial and long-term performances of the component. Specialized techniques are then developed to modify the chemistry and morphology of the surface of the reinforcement so as to achieve strong and durable bonding with the elastomer matrix [Lechtenboehmer et al., 1990, van Ooij, 1977]. Due to more restrictive regulations regarding processes and product toxicity, substantial efforts are undertaken to develop environmentally friendly processes [Sarkar and Bhowmick, 2018]. The mechanical performances of these new reinforcement/elastomer interfaces should be assessed which requires the use of specialized testing protocols.

Very few experimental techniques are available to characterize the adhesion between an elastomer matrix and a single reinforcement cords or cable [Nicholson et al., 1978, Ellul and Emerson, 1988, Brown, 1996, Gent and Yeoh, 1982, Lake, 2003]. They are mainly adapted from classical pull-out tests and some of them are now standardized (ISO 4647, ISO 5603,[ASTM D1871, 2014]...). Recently, the rubber cord adhesion inflation test (RCAIT) has been proposed as an alternative technique for refined mechanical characterization of rubber to reinforcement wires bonding [Corbel et al., 2022, Kane et al., 2019]. The specimen consists of a unique cord reinforcement embedded along the central axis of a cylindrical rubber envelope and initially partially debonded on one end. A pressurized fluid is slowly introduced in between the rubber envelope and the cord until a critical pressure is reached and a stable and progressive decohesion is observed along the specimen length. To prevent rubber envelope failure, the specimen is placed in a lubricated confinement tube so as to limit the tube circumferential expansion. Contrary to alternative test procedures, the specimen and test conditions are designed so that a steady state crack propagation regime can be observed when the constant pressure of the injected fluid is measured. Then, this test protocol can be viewed as an axisymmetric confined blister test as proposed by [Dannenberg, 1961, Chang et al., 1989]. The analysis of such a test relies mainly on a global energy balance analysis from which the critical strain energy release rate (SERR) which drives the extension of the decohesion is determined. Basically, the work needed to inject the pressurized fluid is partially stored in the rubber deformation and fluid compression potential energy, the rest being dissipated in the damage processes leading to crack propagation. Other possible dissipation mechanisms can be involved such as rubber envelop damage or viscous dissipation so as fluid viscosity. For this analysis

to be valid, the crack propagation regime should be stationary. Also, all possible unwanted dissipation mechanisms should be minimized and/or evaluated. At last, some of the quantities needed for the energy balance analysis are determined indirectly from measurable quantities so that possible calibration errors should be evaluated.

Due to the axisymmetric nature of the specimen, the fracture process zone surrounding the crack tip region is not visible so the experimental assessment of the RCAIT analysis hypothesis is limited. Then, a finite elements simulation is proposed here to simulate both the crack nucleation and propagation steps considering the hyperelastic nature of the rubber and complex loading conditions. Indeed, a stationary pressure is recorded during the steady state crack propagation regime. Then, it is necessary to reproduce the fluid driven crack propagation process to ensure the calculations will remain stable. For this reason, fluid cavity elements are used together with cohesive elements to achieve progressive interface decohesion and also to control the fluid injection rate in the numerical simulation. This solution was found relevant to simulate the overall macroscopic response of the specimen during the test and the rubber envelope deformation during the crack propagation process. Alternative specialized implementations have been proposed in other contexts such as hydraulic fracture simulation, crack propagation in porous media or elastomer using XFEM [Paul et al., 2018, Jin and Arson, 2020] or phase field [Chukwudozie et al., 2019] implementation. However, no contribution was found where volumetric fluid driven crack propagation along a specific interface and involving hyperelastic material was found. The proposed procedure uses only standard routines implemented in the commercial finite element simulation program, Abaqus©, and could be easily replicated to analyze similar situations.

In the following, after a short presentation of the RCAIT principle and analysis, the finite element implementation of the test simulation is described. The results from the model are compared with the ones obtained experimentally and presented in a previous contribution [Corbel et al., 2022]. Finally, the self-similar nature of the crack propagation regime is discussed by analyzing in detail the finite element simulation and by comparing them with the one obtained with the Thich Tube Rubber Inflation Model (TTRIM) [Kane et al., 2021].

3.2 Rubber cord adhesion inflation test principle

The rubber cords adhesion inflation test (RCAIT) studied here is depicted in Fig. 3.1. To evaluate the crack nucleation and propagation condition along a metal cord and a rubber matrix, a pressurized fluid is slowly introduced between the two components. The specimens are obtained by molding a 9.4 mm diameter rubber cylinder around a 1.3 mm diameter steel wire coated with brass. During the vulcanization process, the rubber creates cohesive bonds with the coating which leads to strong bonding. A release film or anti-adherent coating is placed on one specimen end along a distance a_0= 50 mm producing an initial decohesion to ease the fluid injection and evaluation of rubber mechanical properties. The specimen geometry also includes a flange on the precrack side which is clamped tightly to a fluid injection fixture connected to a hydraulic circuit. Finally, a glass confinement tube having 10 mm inner diameter is placed around the specimen so as to prevent rubber envelope failure and force the crack propagation along the cord. The tube is lubricated to prevent any adhesion between rubber and glass or at least limit possible friction effects.

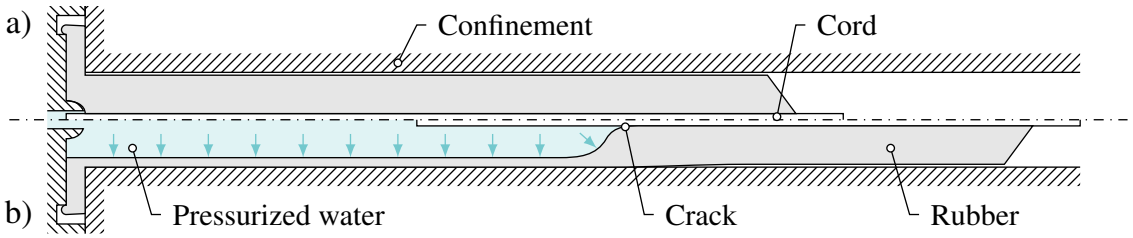

Figure 3.1: Rubber cord inflation test in a) initial configuration and b) pre-crack length inflation regime.

The test is driven under a constant fluid volume injection rate. During the test, the fluid pressure first increases while the precrack part of the specimen envelope inflates. Two regimes are observed here. First the free inflation regime, prior to the outer surface of the specimen touching the confinement tube. Then the confined inflation regime, when the specimen is constrained radially and the envelope expands mainly axially. After a critical pressure is reached, the crack propagates in a stable manner and the fluid pressure remains almost constant. Tap water is generally used for the experiments.

During the test, several quantities can be measured. Fluid pressure, P, is recorded with a pressure sensor placed along the hydraulic circuit. The fluid is injected by using a high-pressure stainless-steel syringe whose piston is attached to a tensile testing

machine to control the volume injection rate. The injected volume, ΔV, is determined from the crosshead displacement measurement after proper calibration of the system is performed to evaluate the possible effect of fluid compressibility and hydraulic circuit compliance. Finally, markers and/or patterns are drawn on the specimen and observed during the experiment with a camera in order to monitor the longitudinal elongation, λ_z, at the surface of the specimen.

Assuming the initial decohesion is large and the contribution of clamping and crack tip regions on the overall deformation is negligible, the measured $P(\Delta V)$ evolutions can be used to evaluate the rubber's mechanical behavior with the help of the thick tube rubber inflation model (TTRIM). Once a critical pressure P_C value is reached a decohesion occurs at/or near the rubber/cord interface. The decohesion then propagates in a stable manner longitudinally while the fluid is slowly injected at a constant pressure value. A simple energy balance analysis is then used to evaluate, G_C, which controls the propagation of the decohesion:

$$P_C \delta V = 2\pi r_c G_C \delta a + w_e \delta a \tag{3.1}$$

In equation 3.1, the term $P_C \delta V$ corresponds to the energy transferred to the system when injecting the pressurized fluid and propagating the crack along a distance δa. This energy is converted mainly into potential energy $w_e \delta a$ due to rubber envelope reversible expansion and fluid incompressibility. w_e corresponds to the stored elastic energy per unit length. Finally, a substantial ratio, $2\pi r_c G_C \delta a$, is dissipated during the fracture process and other dissipative mechanisms. From the global energy balance analysis, the estimated G_C value incorporates all these dissipation sources. According to the above presentation and previous contributions, a reliable analysis of the RCAIT and G_C estimate requires proper monitoring of crack propagation, fluid pressure, injected fluid volume, and specimen deformation. Also, the influence of additional dissipation mechanisms should be evaluated.

3.3 Finite element modeling of the RCAIT

Up to now, the analysis of the experimental data from the RCAIT is essentially funded on conclusions drawn from the TTRIM results [Kane et al., 2019, Kane et al., 2021] and global energy balance evaluation. This 1D model applies to the regime preceding the crack propagation step and describes the inflation of an infinite pressurized rubber

tube whether it is confined or not. However, the influence of the specimen clamping region and the vicinity of crack tip position are not considered. Finally, it would be relevant to assess the energy balance analysis during the crack propagation regime by reproducing with a complete finite element simulation of both crack nucleation and propagation regime. Finally, the self-similar nature of the crack propagation regime could be confirmed.

3.3.1 Model description and preliminary hyperelastic analysis

In the following, all finite element simulations use Abaqus© code. The model geometry and boundary conditions of the model are presented in Fig. 3.2 so as the mesh in the vicinity of the crack tip position. Due to specimen geometry and loading conditions, 2D axisymmetric simulations are performed and cylindric coordinates system ($\vec{r}\vec{\theta}\vec{z}$) is considered. Due to the mechanical contrast between the rubber and steel, the cord reinforcement is modeled as a rigid line placed at a distance 0.65 mm from the cylinder axis. The cord displacement is free along direction $\vec{z}$ but other degrees of freedom are set to zero ($U_r = R_\theta = 0$). The rubber envelope's outer radius is r_{ext} =4.7 mm and is represented with a rectangular solid surface.

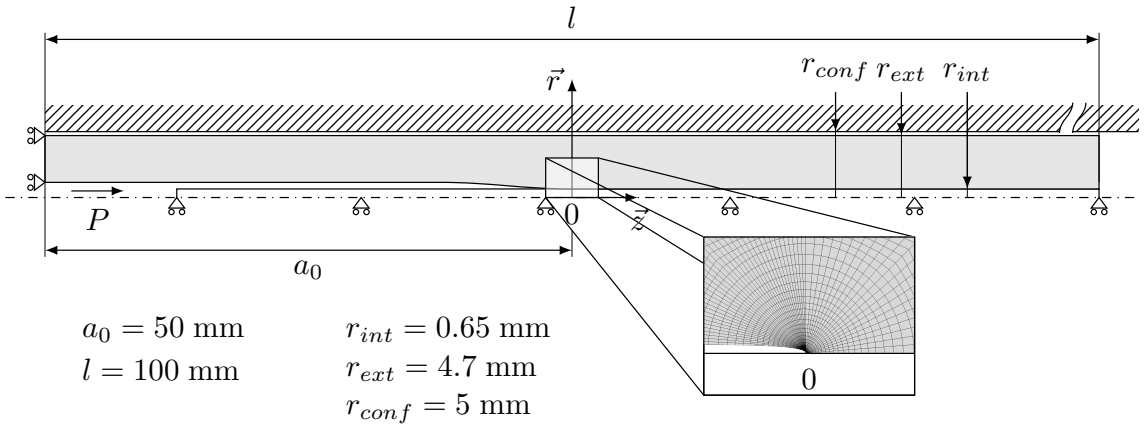

Figure 3.2: Geometry, boundary conditions, and mesh topology of the finite element model for crack onset study. The pre-crack opening is exaggerated for visualization.

In the present analysis, a detailed analysis of the clamping condition is not proposed. Assuming the clamping region length is small compared to the pre-cracked distance, the contribution of clamping region deformation on the overall injected volume will be assumed negligible. Therefore, the clamped side of the specimen is simply replaced by the kinematic condition ($U_z(z = 0) = 0$) corresponding to the free radial

expansion of the rubber tube across the section. Along the $\vec{z}$ direction, the rubber envelope is partially bonded to the cord. The length along which antiadhesive coating is deposited is considered as a pre-crack length, the presence of film or coating is not explicitly considered in the simulation except by introducing discontinuity between the two materials. The interphase region between rubber and cord is not considered either and the bonding between the cord and the rubber is simply modeled with a displacement continuity condition at the interface between rubber and cord.

A focus ring of elements meshes the interface singularity region. 2D axisymmetric quadrangle elements with quadratic interpolation are chosen. Full integration and hybrid formulation scheme (*viz.* CAX8H in Abaqus) are used to manage material incompressibility. All present computations use the implicit solver of Abaqus and the hypothesis of finite strain.

Finally, the 5 mm inner radius confinement tube is introduced. Again, the mechanical contrast between rubber and glass tubes is very large so that the confinement tube can be modeled as a fixed rigid body. Considering that the lubrication between the glass tube and rubber is efficient, the contact between the rubber envelope and the confinement is modeled as frictionless contact using node-to-surface and penalty algorithms. Various loading conditions can be applied to the inner radius of the rubber envelope (pressure, volume variation, ...) which are detailed below.

The Exp-Ln strain energy potential [Khajehsaeid et al., 2013] is used to derive the rubber material constitutive law, as given in equation 3.2:

$$W = A\left[\frac{1}{a}\exp(a(I_1-3)) + b(I_1-2)(1-\ln(I_1-2)) - \frac{1}{a} - b\right] \tag{3.2}$$

The expression of the strain energy density function only depends on the first invariant I_1 of the transformation gradient. The Exp-Ln strain potential is applicable to natural rubbers reinforced with black carbon which exhibit hardening for large elongation values. Material parameters A, a and b values used for the simulation have been identified previously ($A = 1.29$ MPa, $a = -1.19$, $b = -0.87$) [Corbel et al., 2022]. The constitutive law is implemented in the finite element code Abaqus© using the UHYPER subroutine.

In Fig. 3.3 is represented the deformed configuration of the specimen for several inflation pressure values up to 9 MPa as determined with the finite element model. The maximum pressure value corresponds to the one measured experimentally when the decohesion of the rubber/cord interface propagates. A 4.9 MPa pressure value is found

for the end of the free rubber expansion regime and the start of the rubber envelope to confinement tube contact ($r_{ext} = r_{conf}$). Then, at higher pressure, the confinement tube tends to constrain the rubber envelop radial expansion. Meanwhile, the axial expansion along the tube axis tends to increase rapidly with the pressure.

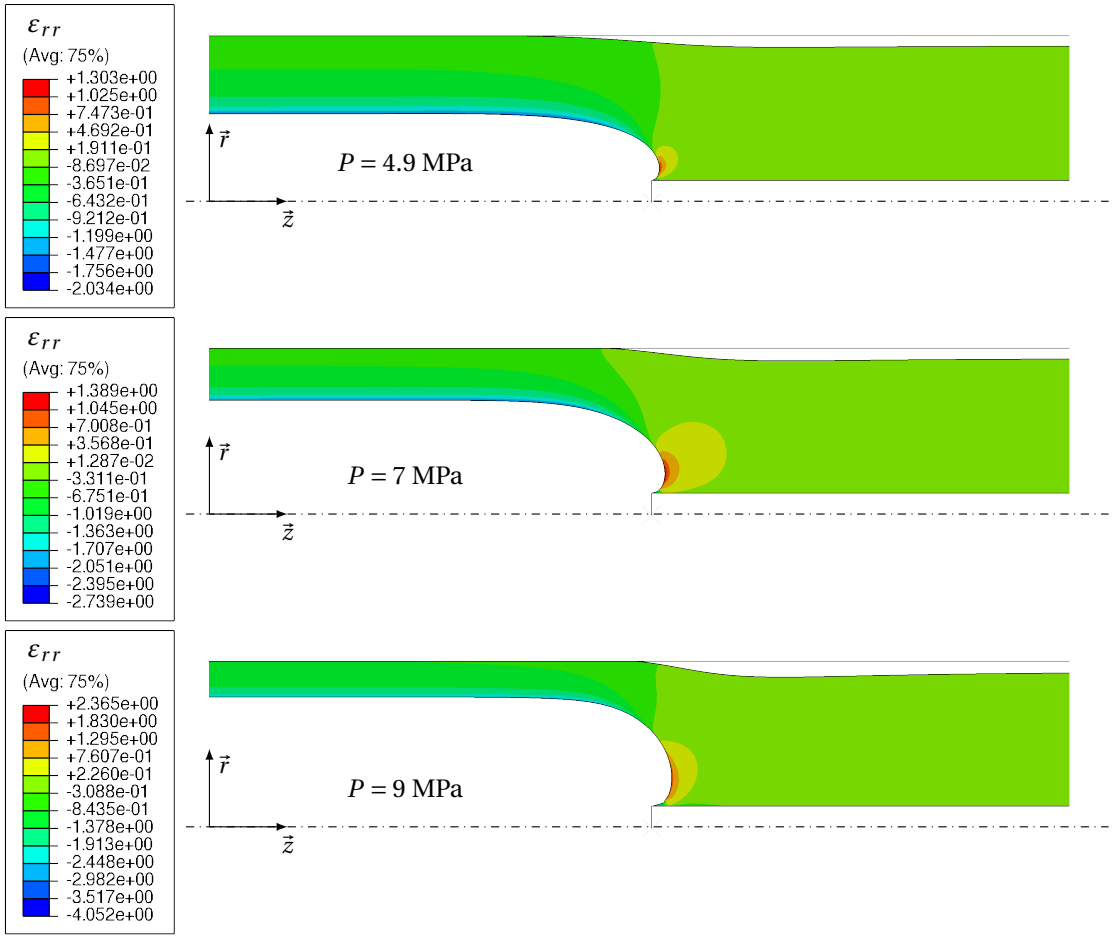

Figure 3.3: Opening logarithmic deformation at different pressure for the crack onset model.

These results may seem similar to the ones observed in other contributions [Liechti and Wu, 2001, Neggers et al., 2015] where elastomer/metal delamination mechanisms are discussed and modeled. However, peel-like mechanical test procedures are generally considered which leads to very different stress/strain fields in the fracture process zone region compared to the RCAIT situation. The main difference lies in the fact that due to the axisymmetric situation, the crack front is circular, and homogeneous plane strain condition is achieved all along the crack front. As also observed when strong adhesion is achieved between rigid and soft bodies, a blunted crack tip is observed at a

finite distance from the rubber/metal interface. The initial stress singularity located at the crack tip position vanishes since the rubber/cord contact angle becomes very small [Krishnan and Hui, 2009, Lengyel et al., 2014]. Such a result is consistent with a previously observed fractured surface where a thin layer of residual rubber was observed on the cord after complete failure. The mapping of the ε_{rr} distribution in the specimen section does not illustrate the modification of the rubber loading condition from mainly radial to longitudinal expansion but clearly enlightens the presence of large circumferential stress concentration along the blunted crack tip at a finite distance from the rubber/cord interface.

Now that the initial stage preceding the crack onset has been described, additional features should be added to the finite element calculations to simulate the crack initiation and propagation steps. Due to the presence of the initially sharp crack tip, numerical convergence of the node-release crack propagation technique is difficult to achieve. More advanced methods such as phase field, X-FEM are numerically costly, and specific formulation and implementation are required to describe the fluid injection process. The main objective of the present model is to analyze the macroscopic response of the RCAIT specimen trying to capture the overall response of the rubber envelope so as its interaction with the fluid and the confinement tube. Nevertheless, numerous highly nonlinear phenomena can be evidenced (large displacements and rotations, hyperelastic behavior, contact, ...). It seems difficult to capture these macroscopic phenomena together with a fine description of the damage processes at the crack tip position which could be studied in a second step. A phenomenological description is then chosen to model the interface decohesion.

3.3.2 Cohesive zone modeling of crack nucleation

Since the crack path is known, a cohesive zone modeling (CZM) approach seems appropriate as proposed in previous contributions [Liechti and Wu, 2001, Mukherjee et al., 2016, Meng and Chang, 2020]. Indeed, using CZM allows for the simulation of both the decohesion nucleation and propagation regimes of the interfacial region between the rubber and the cord. A phenomenological description is then achieved since the cohesive elements are not capable of describing the complexity of the damage processes at the crack tip. However, after appropriate calibration, a damage process zone with physical extent should be observed and a sensitivity to mode mixity loading conditions can be introduced.

So, a layer of cohesive elements is introduced in between the rubber material and the solid line representing the rigid cord. Using Abaqus cohesive elements is preferred rather than cohesive surface interaction following a recommendation from [Gilormini and Diani, 2015] for finite strain considerations. Abaqus surface interaction integrates the cohesive model on the current configuration, while cohesive element maps back to the initial configuration. It leads to a large difference of over 10% in the effective work of fracture in the case of an elastomeric peel test from a rigid substrate.

The model including cohesive elements is quite similar to one presented in section 3.3.1. However, the introduction of cohesive elements needs to modify the mesh topology. Mesh and boundary conditions applied to the finite element model are presented in Fig. 3.4. A grid-like mesh topology is used for the rubber envelope with higher element density near the inner radius where large elongation gradients are expected. Quadratic size distribution is used, therefore the mesh density along $\vec{r}$ is given by the total number of elements in the radial direction N_r, set at 20 elements. 2D axisymmetric quadrangle elements with linear interpolation (CAX4H) are chosen to ensure connectivity with the rest of the elements.

Cohesive elements are inserted between the rubber envelope and the rigid cord along half of the total length, with element density equal to $d_z = 4$, to bond the cord to the rubber envelope. Cohesive elements COHAX4 from the element library of Abaqus© with an initial zero thickness are used (see Fig. 3.4). The cohesive element length is identical to the rubber mesh (0.25 mm). The cohesive element is formulated with a 2D axisymmetric hypothesis, linear interpolation, and a Newton-Cotes integration scheme. As discussed above, the detailed description of the mechanical fields and damage processes close to the rubber/cord interface is replaced by a one-dimensional phenomenological description of the overall decohesion process. The cohesive model controls the evolution of cohesive stresses normal and tangent to the interface as a function of the relative displacement across the interface until complete decohesion. A phenomenological stress versus displacement evolution should be calibrated so that the simulated overall specimen response is found similar to the one observed experimentally. As main parameters, the cohesive element stiffness, K, should be chosen so that no significant softening is introduced during the elastic loading regime. Also, the CZM parameters (*viz.* max. relative displacement, δ_f, ultimate stress, σ_0, ...) should be chosen so as to respect the energetic criteria controlling the complete decohesion of the interface.

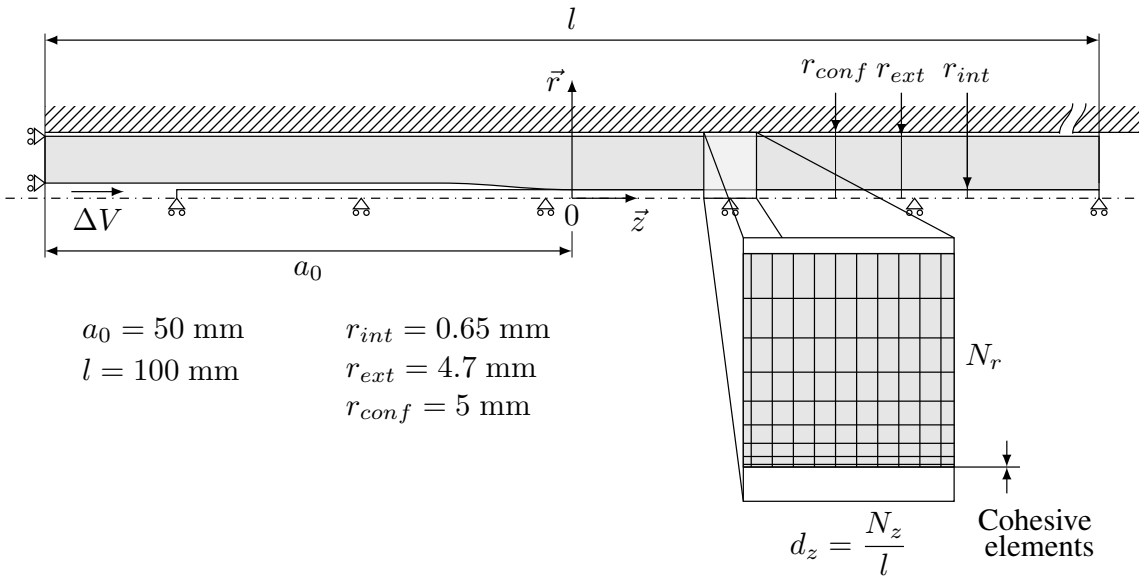

Figure 3.4: Geometry, boundary conditions, and mesh topology of the finite element model including cohesive elements. The pre-crack opening is exaggerated for visualization.

In the present RCAIT configuration, the crack nucleation intermediate regime cannot be distinguished from the reversible loading regime prior to crack propagation by analyzing $P(\Delta V)$ or $P)\lambda_z)$ evolutions. This suggests that the fracture process zone extension remains small compared to other dimensions so that linear elastic fracture mechanics is applicable. CZM parameters should be chosen also to observe the limited extent of the fracture process zone in the simulations. A triangular interface separation law is generally adopted for cohesive element [Liechti and Wu, 2001, Meng and Chang, 2020, Mukherjee et al., 2016] over trapezoidal or exponential laws. However, large fracture process zone is generally observed which are not consistent with the experimental observations. Then, a trapezoidal law is preferred here with an additional shape parameter, r, which controls the plastic regime extend, is used. A higher energy dissipation can be introduced while keeping the same critical stress and critical relative displacement at the break. Interface separation law is represented in Fig. 3.5. In the following, the nominal interface "stiffness", K, and shape parameter, r, will be kept constant. Indeed, K, is set so that the overall specimen stiffness response is not altered with respect to the rigid interface situation. Meanwhile, the critical strain energy release rate G_C is set arbitrarily in a range of values corresponding to the ones measured experimentally. The critical stress σ_0 is directly linked to G_C, K, r and δ_f. Then δ_f, σ_0, and r are chosen so as to obtain a physically realistic fracture process zone (FPZ)

configuration. As evidenced in section 3.3.1 and generally observed in interface decohesion situations mixed mode loading conditions are expected. Mixed mode failure criteria could then be introduced. However, due to the lack of experimental data describing the effect of mode mixity on the decohesion process in this situation, it would be artificial to introduce supplementary parameters. Then identical interface separation laws are used for both traction and shear contributions. The stress criterion at damage initiation is quadratic and the damage evolution rule also considers the coupling between peel and shear stresses. Simulation results will be introduced later, once the method for coupling CZM with the fluid injection process is discussed.

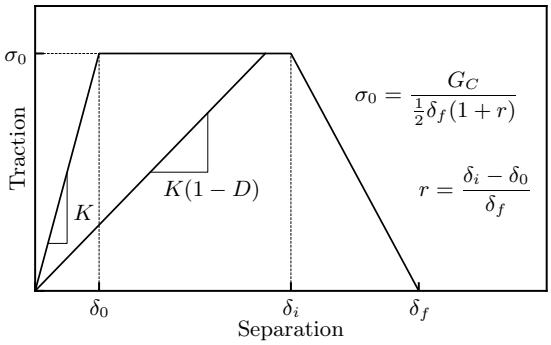

Figure 3.5: Shape of the trapezoidal traction-separation law to model the interface.

3.3.3 Modelling of fluid driven crack nucleation and propagation

Implementation of hydrostatic fluid element

The RCAIT such as most mechanical characterization tests including blister tests is not load-controlled but kinematic-controlled. Indeed, since the injected fluid is incompressible and the compliance of the hydraulic circuit is considered negligible the experiment is driven by fluid volume injection rate. A constant pressure is applied to the inner surface of the specimen but the contour of the inner surface including the near crack tip region depends on the fluid/structure interaction. Since large deformation and nonlinear hyperelastic behavior are introduced the pressure versus injected volume evolution, $P(\Delta V)$, is not linear either. Then applying pressure load to the inner radius of the specimen along the decohesion as a boundary condition is not really representative of the test conditions. Kinematic conditions should be applied in the numerical simulation which are representative of the pressurized fluid injection rate control conditions. This is notably critical to simulate the crack propagation regime

when the fluid pressure is constant where numerical instability may arise unless artificial numerical "viscosity" would be introduced. To control the volume variation inside the rubber envelope rather than applying pressure to the inner radius, hydrostatic elements from the Abaqus elements library are used. Such elements describe the mechanical behavior of a closed cavity filled with either compressible (pneumatic) or incompressible (hydraulic) fluid. They introduce a simple fluid-structure interaction through the hypothesis of constant pressure across the fluid volume and assume the effect of liquid inertia is negligible. This formalism was previously used for mechanical study of pressurized vessel [Rumpel and Schweizerhof, 2004], air spring suspension [Berry and Yang, 1996], air-filled closed-cell foam [Mills et al., 2009] or multiple pneumatic crash cushion [Graczykowski and Heinonen, 2007].

Numerically, a layer of fluid cavity limits elements (here FAX2) is introduced around the enclosed space between the rubber and the cord interface. The FAX2 elements mesh the boundary of the fluid cavity, sharing nodes with the corresponding surface. Then, a node placed in the meshed cavity acts as an integration point to compute the pressure. For an axisymmetric situation, this node must lie on the axis of revolution.

As a boundary condition, a prescribed quantity of fluid can be added to a cavity. This parameter corresponds to the one set experimentally. Providing, the displacement of the inner radius of the rubber envelope could be prescribed by the expansion of the fluid cavity at a given expansion rate, a uniform pressure will be applied to the inner radius of the rubber envelope.

Coupling fluid cavity element and cohesive element

The simulation of fluid driven crack propagation remains a complex issue especially due to the difficulty in controlling the application of the pressure loading to the newly created surface. The simulation of the RCAIT is even more complex due to the large deformation of the medium coupled with the fact that the injected fluid pressure is expected to be constant during the crack propagation regime. Therefore, to achieve numerical stability, kinematic controlled loading conditions should be applied. Therefore, the proposed strategy consists of introducing multiple connected hydrostatic fluid cavities along the rubber/cord interface which will be filled with fluid sequentially during the crack propagation regime to force the crack opening while the decohesion extends. This solution is proposed since the pore pressure cohesive elements and hydrostatic fluid cavities cannot be used together in a model in Abaqus. The main advantage

of the coupling presented here is the meaningful dialogue between the inflation of the pre-crack length of the specimen and the newly cracked surface length. The coupling of the fluid cavity is also possible with continuum element degradation or node-release crack propagation.

The superimposition of the initial mesh with the fluid cavity elements network describing the interaction between cohesive and fluid cavity elements is presented in Fig. 3.6. A main fluid cavity maps the initial pre-crack length of the specimen. Then, a succession of fluid cavities is superimposed on each cohesive element. However, each cavity is extended up to the axis of revolution in order to compute the injected volume properly and allow to place the integration point of the cavity. These cavities are filled sequentially along the crack propagation path, and fluid link elements are used to connect each successive cavity. The fluid flow from the first cavity to the following is given by the relation:

$$\Delta P = P_m - P_s = C_v q \tag{3.3}$$

Where ΔP is the pressure difference between the first (pressure P_m) and following (pressure P_s) cavities, C_v is a viscous resistance coefficient and q is the fluid flow between the two cavities. This additional numerical parameter, C_v, should be calibrated so that no artificial rate dependence effect is observed. Also, the fluid link elements have a modifiable fluid behavior since C_v can depend on ΔP, temperature, or user-defined field variables f_v. This last dependency is the key to the coupling between fluid cavities flow connection and cohesive elements degradation. Indeed, from a physical standpoint, the flow of the fluid penetrating the fracture process zone may be dependent on local damage to the rubber. Then, the C_v coefficient value is updated during the simulation as a function of the damage level of the local cohesive element. For now, a simple cavity onset criterion is introduced considering the local fluid cavity element starts to fill once the damage variable D of the local cohesive element is more than 0.2. Indeed, it was observed that the numerical convergence is enhanced when the pressure is applied before the total degradation of the cohesive element is reached. Therefore, the pressure locally increases with the fluid flowing to the cavity and then introducing an intermediate process zone region where the internal pressure accelerates the damage process but also allows smooth injection of the fluid in the newly created area.

The relation between fluid cavity elements and damage is not a standard implementation in Abaqus. The algorithm depicted in Fig. 3.7 is executed between each

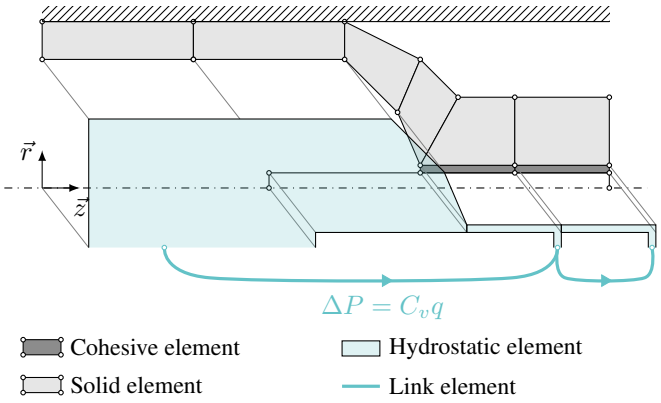

Figure 3.6: Illustration of the superposition of hydrostatic fluid element and cohesive elements (thickness of the cohesive elements is exaggerated) and connection between cavities.

iteration of the finite element solver. First, the local damage value of each cohesive element is read with a URDFIL subroutine. Then, the subroutine UFIELD assigns a field variable, f_v, to each fluid link element depending on the damage of the cohesive element located at the slave cavity element. Two values can be assigned to C_v. In case $D < 0.2$ then C_v is set to zero so that the fluid is blocked, in case $D \geq 0.2$ then an incommensurable value is assigned to C_v so that the fluid fills the cavity immediately at the next iteration. A Fortran COMMON BLOCK is used to retrieve damage values from the URDFIL subroutine and transmit them to the UFIELD subroutine.

With this numerical procedure, the whole crack nucleation and propagation steps are simulated reproducing the complete RCAIT. In particular, fluid-driven crack propagation under a constant volume injection rate is achieved with a stable crack propagation regime with constant fluid pressure. Add to the cohesive zone parameters two additional parameters (onset, C_v) which control the pressurized fluid flow through the process zone.

3.4 Cohesive zone modeling of the RCAIT

In the following, the numerical procedure described above is used to reproduce theoretically the experimental results obtained on a specimen made with NR bonded to a brass-coated steel cord. After a satisfactory agreement is found at a macroscopic scale, then the results from the simulation are analyzed to evaluate locally the conditions leading to crack nucleation and propagation and also to discuss the limits of the

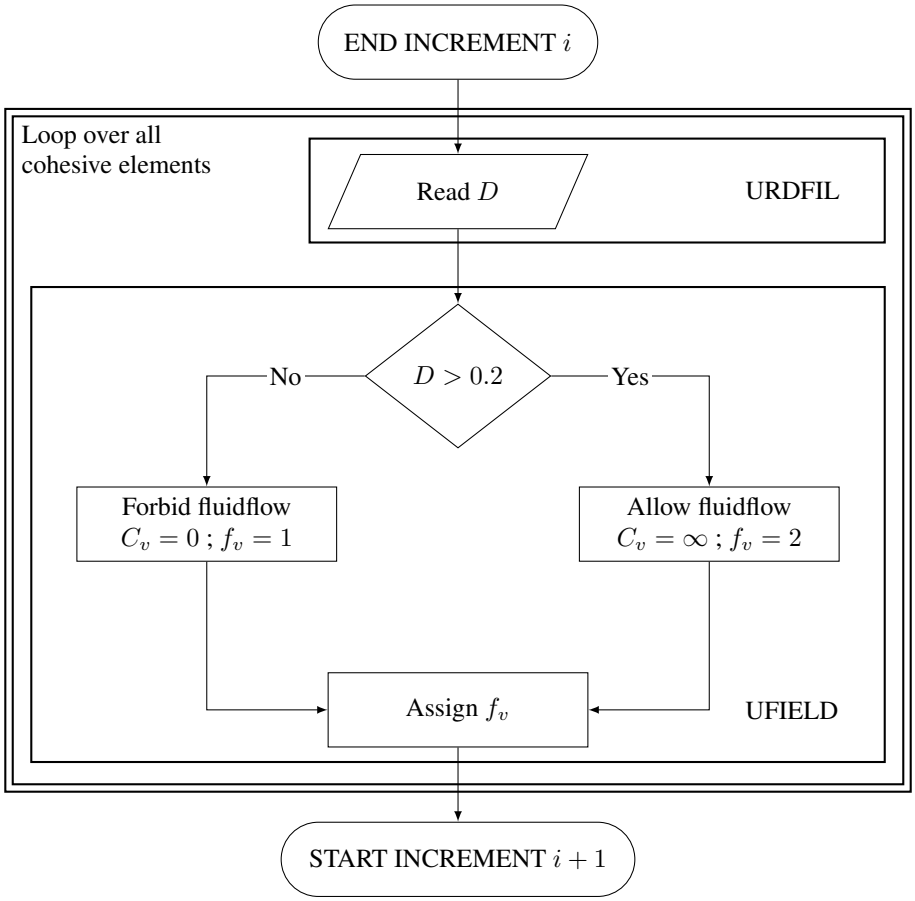

Figure 3.7: Flowchart of numerical procedure to combine fluid cavity and cohesive element and the breakdown between the two Abaqus subroutine.

proposed approach.

3.4.1 RCAIT macroscopic response - experimental vs theoretical

As discussed above, most of the material parameters controlling the response of the RCAIT can be determined experimentally. Indeed, a simple hyperelastic model of the rubber behavior has been identified from uniaxial tensile test data and evaluation of the RCAIT data along the pre-crack length. The critical SERR of the rubber/cord interface is obtained from energy balance analysis of the RCAIT, and rubber strength is obtained from tensile test results again. The remaining parameters are mostly numerical ones except for the remaining cohesive zone model parameters (*viz.* r and δ_f). In the following, the shape factor is set arbitrarily to 85%. Indeed, as for most cohesive zone models use cases, a high enough element density should be used to ensure an appropriate description of the interface separation law along the FPZ. Then, $r = 0.85$ was

G_C	K	σ_0	r	δ_f
80 kJ/m^2	1000 MPa	30 MPa	0.85	2.8 mm

Table 3.1: Cohesive zone model parameters.

found satisfactory to obtain a satisfying compromise between mesh density, numerical cost, and description of the FPZ. Then a smooth development of damage along the process zone was found which is also a necessary condition to observe a progressive filling of the fluid cavity elements according to the scheme depicted in Fig. 3.7. Then, the last parameter to be determined is the displacement jump leading to complete interface separation, δ_f, which is found equal to 2.8 mm. CZM parameters are finally summarized in Table 3.1.

In figures 3.8 and 3.9 report the main experimental data recorded during a RCAIT which are compared with the complete results of the RCAIT simulation describing decohesion nucleation and propagation regimes. It should be noted that the simulation is stopped before total delamination of the whole interface is observed considering the computation time. Indeed, for $G = 80\,\text{kJ/m}^2$, the simulation of a 1 mm crack propagation requires approximately 3 days of processing using 16 cpus at 2.60 GHz. In Fig. 3.8, the injected fluid pressure, P, versus injected fluid volume shows satisfactory agreement for both the crack nucleation and propagation regime. Indeed, during the crack propagation regime, the same plateau pressure value is found which confirms the crack propagation behavior is controlled at the macroscopic scale by the only energy balance criteria. During the crack nucleation regime, very similar behavior is observed. The experimental evolution exhibits more compliant behavior so as abnormal preliminary inflation regime. Indeed, the specimen attachment condition is not precisely modeled in the finite simulation nor the possible presence of air entrapped in the hydraulic circuit so that very stiff initial response is found numerically compared to the experimental result. Also, overall more compliant specimen behavior is found experimentally due both to poor evaluation of the initial decohesion length value and also probably to underestimation of the inner radius of the rubber envelope since the presence of anti-adhesive film is not considered.

During the RCAIT, a marker tracking technique is implemented to evaluate the evolution of the longitudinal elongation at the outer radius position along the specimen axis. Experimental and theoretical evolutions are compared in Fig. 3.12 and exhibit similar evolutions again. A small discrepancy is found on the plateau, λ_z value in the

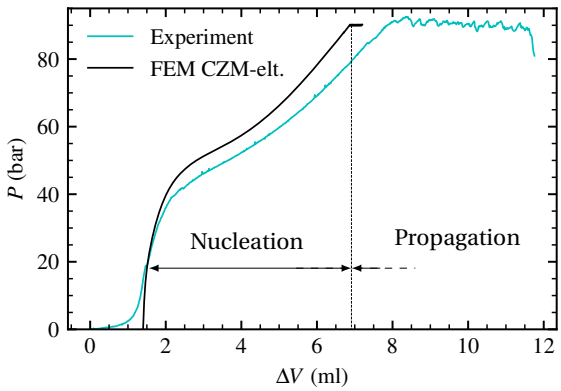

Figure 3.8: Comparison of experimental and numerical inflation curves.

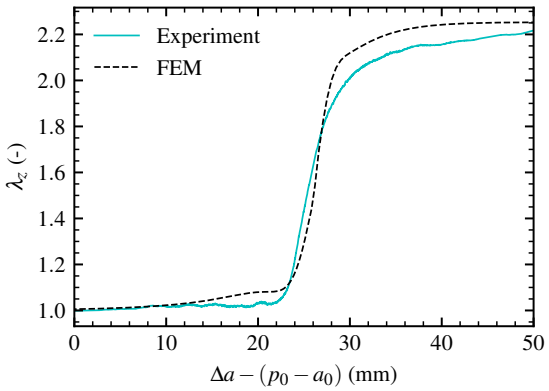

Figure 3.9: Comparison of experimental and numerical process zone.

inflated region of the specimen which may attributed to biased evaluation of the inner radius again, or experimental artifacts such as confinement tube/rubber residual friction. However, the two evolutions evidence identical shape and extend (ca. 20 mm) of the transition region between bonded and fractured parts of the specimen. For both Fig. 3.8 and 3.9 no significant feature allows evidence of the development of a FPZ at the interface scale which justifies the use of simple linear fracture mechanics approach to analyze RCAIT.

Then, using the same procedure, RCAIT is simulated again but considering different critical SERR values for the cohesive elements in the interval [10:80] kJ/m². All CZM parameters are kept the same except ultimate stress which is changed so as to obtain the appropriate G_C value. The resulting fluid pressure versus injected volume evolutions are reported in Fig. 3.10. All evolutions are found the same except the plateau pressure value which varies with the G_C value. The semi-analytical relation derived in [Kane et al., 2021] to evaluate G_C from the measure critical pressure value is compared

with numerical results in Fig. 3.11. Both analytical and numerical model predictions agree which demonstrates again that LEFM is valid to evaluate G_C. This indicates that the FPZ extension should be negligible compared to other characteristic dimensions (rubber envelope thickness, initial decohesion, accommodation length ...) but also that the steady state crack propagation regime is observed after a small crack propagation distance.

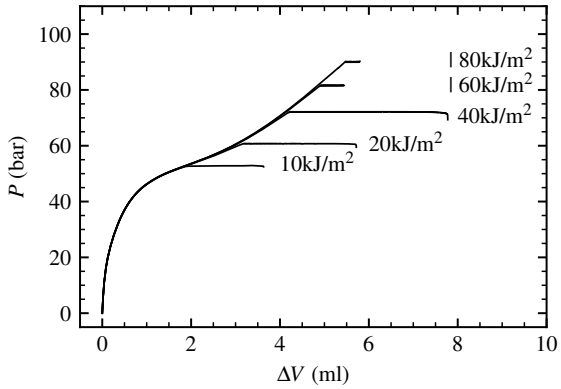

Figure 3.10: Inflation curves prediction of the cohesive modeling for different value (r = 0.85, δ_f = 2.9 mm).

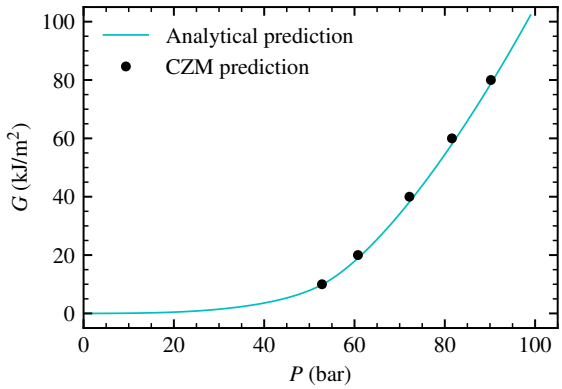

Figure 3.11: Comparison of analytical [Kane et al., 2019] and cohesive modeling prediction of critical pressure to propagation in function of critical SERR.

It should be noted that the value of G_C as high as 80 kJ/m² enforces a correct phenomenological description of the experiment. The dissipation during propagation comes both from the bulk material and the interface. Meanwhile, the model places all the dissipation in the cohesive element. And, as the crack surface is cylindrical, the G_C value is actually dependent on the radial position of the cohesive element.

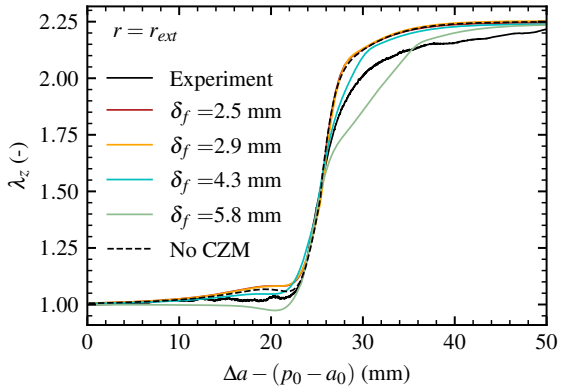

Figure 3.12: Comparison of the transition zone length on the exterior radius of the specimen for different displacement at complete failure for the cohesive zone model ($G = 80\,\mathrm{kJ/m^2}$; $r = 0.85$).

3.4.2 Local analysis – development of FPZ

The previous results seem to indicate that the macroscopic response of the RCAIT is little affected by the exact shape of the interface separation law since non-features related to the FPZ development were observed compared to a purely elastic analysis. However, to assess this hypothesis a parametric analysis is performed by varying parameter, δ_f, and modifying σ_0 accordingly to keep constant $G = 80\,\mathrm{kJ/m^2}$ value. The resulting $\lambda_z(z)$ evolution for all test cases are reported in Fig. 3.12. For the two smaller values considered in this study including the one used in section 3.4.1, the resulting evolutions are identical to the one obtained for the perfectly bonded interface. For a significant difference to be observed very large δ_f values should be used leading to unrealistic FPZ extension. The total displacement to failure can reach a size similar to the confinement radius r_{conf} while still reaching a steady-state propagation. Indeed, the confinement radius limits the opening displacement. Nonetheless, if the element does not fail under opening mode for a small process zone, it will undergo a shear loading. Therefore, while the opening displacement is limited by the confinement radius, the shear displacement is limited only be the maximum axial elongation of the fully cracked part of the specimen. Then the parameters given in Table 3.1 offer the best compromises with the present mesh topology to reproduce the results obtained at a macroscopic scale.

In Fig. 3.13 are reported the cartography of the radial elongation in the specimen cross-section, and contour also presented in section 3.3.1 to evidence the presence of strong stress concentration at the blunted crack tip position. The contour of the refer-

ence configuration (rigid interface) for the same injected fluid pressure value is superimposed with the result of the cohesive zone modeling. Both contours match except in the vicinity of the crack tip position where the presence of a cohesive element strongly modifies the contact angle between rubber and cord and more generally the near cord region. These pictures illustrate the phenomenological nature of the proposed modeling strategy which requires careful calibration of the CZM parameters as a function of the mesh topology and consequently its limitations. Indeed, the CZM modeling aims to describe the rubber/cord interface decohesion. From Fig. 3.3, it is clear that the crack will initiate and propagate from the stress concentration region located at a finite distance from the interface. The CZM parameters are then representative of the decohesion of the near cord region over a finite distance rather than the one of the interface unless very small element sizes are used. Indeed, with the present mesh topology no crack propagation is observed with the CZM when small δ_f values are used (and consequently large σ_0) since due to the element distortion at the crack tip position, the normal stress in the cohesive element becomes compressive and block the development of any damage. δ_f values are finally representative of the radial position of the blunted crack tip when crack propagation starts.

At last, the damage value in the cohesive elements is reported which is also representative of the pressure of the local fluid cavity element and applied to the inner contour of the rubber interface. As seen in Fig. 3.13, by filling the fluid cavity when the damage value in the cohesive element is larger than 0.2, the fluid pressure is applied to most of the inner contour of the rubber envelope so that the resulting deformation is similar to the one obtained by considering rigid interface. In conclusion, the present finite element procedure is capable of describing both crack nucleation and propagation sequence during RCAIT and the overall macroscopic response including the regular stress and elongation fields in the rubber envelope. However, CZM remains phenomenological so calibration is required. Such macroscopic description then fails in describing the exact nature of the process zone, however the identified CZM parameters are representative of specimen configuration.

3.4.3 Loading paths during crack propagation

In previous contributions, the analysis RCAIT uses only one-dimensional TTRIM which doesn't consider the three-dimensional nature of the stress and elongation fields in the accommodation region. Also, the TTRIM only describes the initial inflation regime of

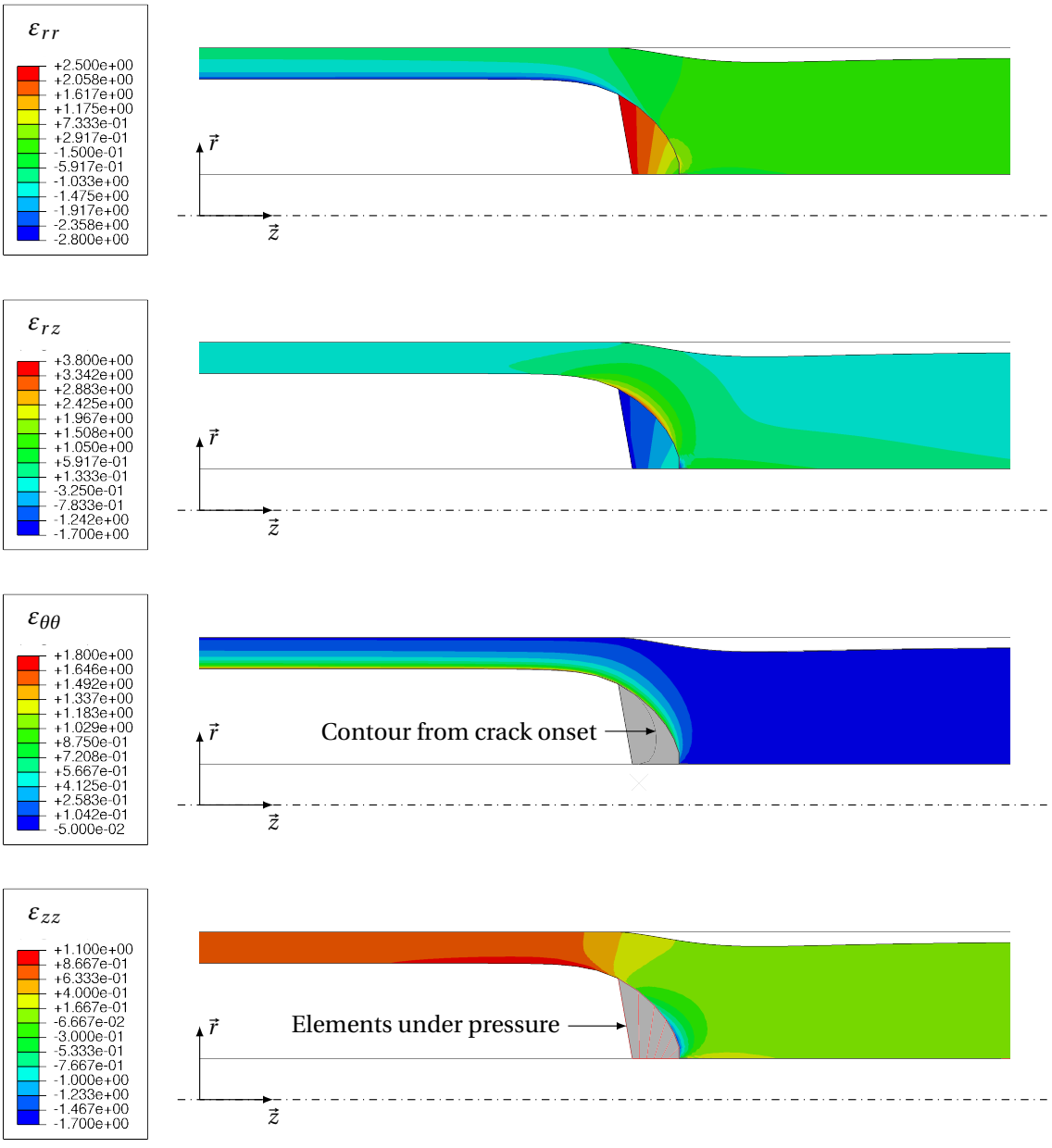

Figure 3.13: Cartography of the strain tensors value around the crack tip during propagation.

the precrack region but not the crack propagation regime. Capturing the exact loading path in the specimen could be important to better evaluate the dissipative mechanisms in the rubber during crack propagation.

To illustrate this, the evolution of the local elongations of a given element during crack propagation is reported in Fig. 3.14. The evolutions are plotted as a function of the instant distance to the crack tip position so that in an Eulerian representation of

a steady-state crack propagation regime, these evolutions are similar to their spatial evolutions along the specimen for a given crack tip position. Two radii are considered, on the outer skin and the mid-through thickness position. As the finite element can only capture globally the strain field around the crack tip, a loading path on the inner radius is omitted. Also, the values determined with the TTRIM are reported. These evolutions are found the same whatever the element is chosen at the same radial position along the crack propagation direction which confirms the self-similar nature of the crack propagation regime. Also, these simulations clearly reveal the multiaxial nature of the rubber loading condition during crack propagation also predicted with the TTRIM.

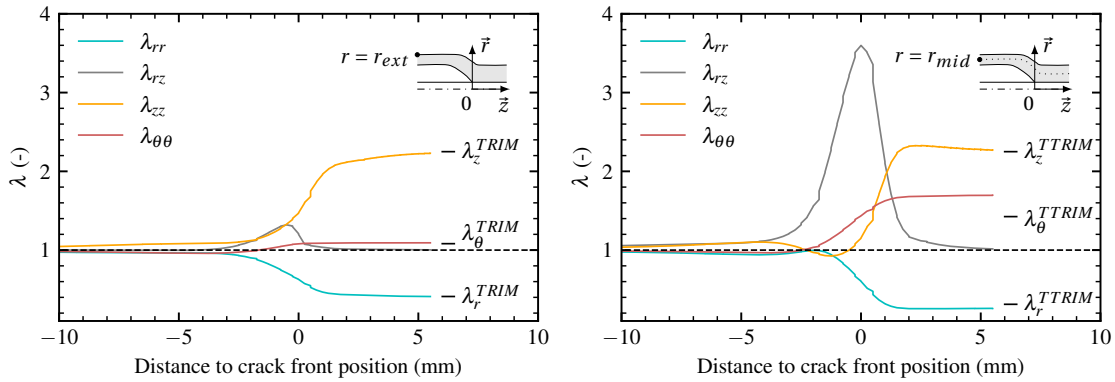

Figure 3.14: Evolution of the elongation of an element of matter in the middle and the exterior of the rubber envelop as the cord delamination advances ($\sigma_0 = 30\,\text{MPa}$, $r = 0.85$, $G_C = 80\,\text{kJ/m}^2$).

However, a significant shear deformation is found along the accommodation length which is not predicted with the TTRIM. In Fig. 3.15, the two loading paths are compared in the principal stretches space, at the middle and the exterior of the rubber envelope. The two paths are similar at the exterior radius, while a difference appears at the mid-radius. Moreover, the shear component is predominant on a large amount of the path. The analytical solution has an eigenspace corresponding to the global coordinates $(\vec{r}\vec{\theta}\vec{z})$, while the FE CZM eigenspace has an angle with respect to the global coordinates. An angle value of 0° indicates only traction/compression deformation and 45°, only shear deformation. The angle is higher on the mid radius than on the exterior radius, meaning a higher shear state closer to the interface. Thus, the local rubber and interface loading condition is different from the early analysis with the TTRIM and indicates that shear behavior characterization of the rubber would be needed for proper hyperelastic model calibration.

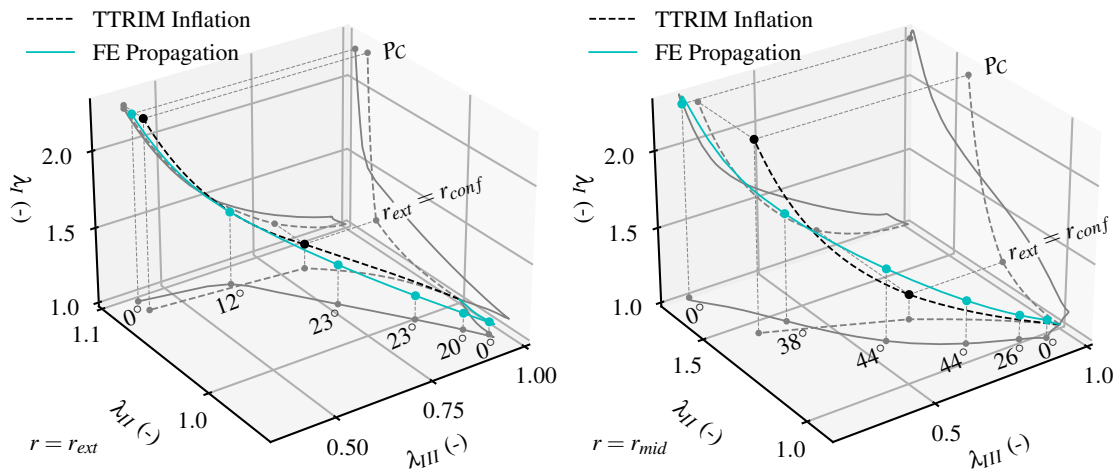

Figure 3.15: Comparison of loading path in principal stretches space between inflation (TTRIM analytical) and propagation (FE CZM) at two radii. Rotation angle between the FE and the analytical eigenspaces is reported on FE loading path.

3.5 Conclusion

In the present contribution, a simulation of the complete RCAIT considering a fluid-driven crack propagation test under constant injection rate conditions is achieved. The original implementation is proposed here consisting of coupling fluid cavity elements with cohesive zone elements. The load application conditions over the whole crack nucleation and propagation process are reproduced from which the self-similar nature of the crack propagation can be observed as associated with a fluid injection pressure value. The model calibration uses mainly data directly obtained from macroscopic tests (rubber behavior, rubber strength, specimen fracture energy). Indeed, with the actual specimen geometry, the experimental data recorded during the test can be reproduced with simple LEFM consideration and hyperelastic modeling of the rubber inflation. Then little/no influence of the CZM parameter is found except G_C. Other two parameters K, r, δ_f are chosen essentially to ensure numerical convergence and realistic FPZ extension. to propagation dictated by the critical strain energy release rate. With this model, a more complete picture of the RCAIT condition is obtained and the self-similar nature of the crack propagation condition is validated. While the detailed description of the FPZ is not achieved, a more realistic description of the accommodation region is obtained which exhibits large shear deformation values that are not predicted with the TTRIM where the maximum deformation state could be reached.

Multiple perspectives regarding the application of the present RCAIT finite element

model can be drawn. First, the model can be used for a better estimate of the influence of test boundary conditions. In particular, the effectiveness of rubber to confinement tube lubrification could be assessed by introducing friction contact. Additional bulk dissipative mechanisms apart from the one developing in the FPZ can now introduced in the rubber behaviour such as softening [Mullins, 1969] and viscosity with the objective to deconvolute these contributions from the one driving locally the crack propagation. Finally, these results could be assessed with supplementary experimental observations which may require the use of tomographic equipment to image the specimen section during crack propagation.

Friction effect 4

P.-Y. Corbel, J. Jumel

"Rubber Cord Adhesion Inflation Test: influence of envelope/confinement friction"

published in Engineering Fracture Mechanics, vol. 298 (2024) 109919

The Rubber Cord Adhesion Inflation Test (RCAIT), has been previously introduced as an alternative test protocol to traditional pull-out tests for measuring the toughness of rubber matrix to metal reinforcement interfaces. A pressurized fluid is injected in between the matrix and reinforcement in a non-adherend region to initiate and propagate a crack along the specimen. A self-similar crack propagation regime hypothesis is assumed and the critical strain energy release rate is obtained from a simple energy balance analysis. However, to force the crack propagation along the specimen and prevent the development of an aneurysm in the rubber envelope, a confinement tube is used. A lubricant allows "free" longitudinal expansion of the rubber envelope during the contact. Combined theoretical, numerical, and experimental analyses are then proposed here to assess the effectiveness of lubrication conditions. Our results indicate an inversely proportional scaling between the elongation gradient and the friction coefficient in the pre-crack region. The observation confirms the validity of frictionless contact with a greased contact. Meanwhile, the steady-state crack growth assumption holds with the introduction of contact friction.

4.1 Introduction

Controlling the adhesion between fibrous reinforcement and polymer matrix is fundamental to achieving optimal performances of composite materials. For this reason,

chemical and/or physical processes are generally implemented to modify the nature of fiber surfaces to achieve appropriate compatibility with the polymer in which they are to be embedded [Crowther, 2001]. Needs for improved mechanical performances and durability, but also more demanding environmental and safety regulatory constraints, resulting in the development of alternative products and processes including new surface preparation protocols. To support these developments a better understanding of the key mechanisms that rule the fiber adhesion, interphase formation, aging phenomena, and failure mechanisms at the interface scale is needed.

Apart from fiber-reinforced polymer applications, rubber, and elastomeric components also use fiber or fabric reinforcements to enhance rigidity and strength. Metal cords and cables are often used for structural applications. The adhesion between the rubber matrix and the reinforcements should be assessed with a series of mechanical tests at various scales and tried to reproduce in-service conditions. However, few test protocols are available to characterize the adhesion of a single fiber. Most of them are derived from pull-out test configurations (e.g. ISO 4647, ISO 5603, or ASTM D1871) so that the interface mainly sustains shear loading conditions [Brown, 2018, Nicholson et al., 1978]. Recently, an alternative test protocol called the Rubber Cord Adhesion Inflation Test (RCAIT), has been proposed for characterizing the adhesion between metal cords and rubber matrix [Kane et al., 2019]. In this test, a pressurized fluid is injected in between a cylindrical rubber envelope and a single reinforcement to propagate a crack along the interface. After a critical pressure value P_C is reached, a stable crack propagation regime along the cord with constant injected fluid pressure value. Assuming a steady-state crack propagation regime, an energy balance analysis is performed for which the critical strain energy release rate G_C driving the fracture is determined from the pressure vs. injected fluid volume evolution recorded during the test. However, for large adhesion values, the crack may deviate from the interface and lead to rubber envelope failure. As suggested by [Chang et al., 1989] for the blister test, confinement is then used to force the decohesion to propagate along the cable. The same energy balance analysis is applicable whether confined or unconfined conditions are used (both boundary conditions are modeled) provided the specimen is free to expand along the cord direction. Then, a lubricant is deposited on the specimen and tube surface to achieve frictionless contact conditions.

Several lubricants have been used to assess the free longitudinal expansion hypothesis and evaluate if the nature of the lubricant could modify the test result. For most

test conditions, the same experimental results were obtained during the propagation regime. However, when dry contact is considered the rubber envelope adheres to the confinement tube so that a very small fluid quantity is needed to separate to cord from the rubber. Experimental investigation of the influence of contact behavior would be complex to implement due to the large variety of lubrication conditions to be tested. Then, combined theoretical, numerical, and experimental analysis is proposed here to analyze the crack onset and propagation regimes during RCAIT and evaluate the influence of confinement tube/rubber envelope friction. The technical objective is to demonstrate that providing the appropriate lubricant is used the actual RCAIT protocol and data reduction techniques are robust enough to achieve reliable determination of the G_C. From a scientific perspective, the refined analysis of the RCAIT is required for better analysis of the local damage processes leading to the development of the fracture process zone and the propagation of the decohesion. The study of elastomeric envelop inflation contact is also beneficial to a larger extent in inflation mechanics [Gasser et al., 2005, Patil et al., 2014] or tribology [Devalba et al., 2018, Dong et al., 2023, Tuononen, 2016].

4.2 Rubber cord adhesion inflation test

4.2.1 Test presentation

The RCAIT has been introduced by [Kane et al., 2019] as an alternative testing protocol to the H-test [Gent et al., 1981], a pull-off / pull-out test [Huang et al., 2023, Jiang and Penn, 1992] to evaluate the adhesion between rubber and reinforcement. This protocol is inspired by the test configuration proposed by [Dannenberg, 1961] and can be assimilated as a “tubular” version of the constrained blister test proposed by [Chang et al., 1989].

The specimen depicted in Fig. 4.1 consists of a fiber/cord or cable reinforcement embedded/bonded along the axis of a cylindrical rubber envelope. One side is left unbonded using either a demolding agent or PTFE tape so that pressurized fluid can be introduced to inflate the rubber envelope and act as the pre-crack length a_0. In this work, the specimens are obtained by molding and curing a black carbon-reinforced natural rubber cylindrical envelope around a 1.3 mm diameter high-strength steel cord coated with brass. The brass coating allows the formation of strong Cu_xS covalent

bonds with the rubber during the vulcanization process leading to strong adhesion [Crowther, 2001, van Ooij, 1984, van Ooij, 1979, van Ooij et al., 2009]. The outer diameter of the cylindrical envelope is 9.2 mm. A flange is added to the specimen geometry on the pre-crack side which is clamped to the hydraulic circuit fixture to ensure fluid-tightness. During the test, tap water is slowly introduced into the specimen under constant volume injection rate conditions (1 ml/min) by pressing a high-pressure stainless-steel syringe with a tensile testing machine. A pressure sensor is placed along the hydraulic circuit to measure the fluid pressure during the test. Supplementary valves and purges are also placed to avoid the presence of air entrapped in the system which would lead to a biased evaluation of the volume of fluid injected in the specimen. Two regimes are generally observed during the test. First, the fluid pressure increases while the pre-crack length of the rubber inflates. Free inflation first occurs before contact is established between the outer diameter of the rubber envelope and the inner diameter of the confinement tube. Then confined expansion occurs before a critical pressure value is reached leading to crack propagation. Then slow and stable crack propagation regime is observed while the pressure of the fluid generally remains constant. From the ultimate pressure value and considering experimental data, geometrical parameters, and rubber mechanical properties, the critical strain energy release rate can then be determined using simple energy balance analysis. The confinement tube is made of borosilicate glass. The confinement is needed to prevent finite strain instability which would be observed in case of strong adhesion and leading to rubber envelope failure rather than crack propagation along the interface [Kane et al., 2019].

On the outer surface of the glass confinement, in the pre-crack region, strain gauges monitor the confinement circumferential deformation depicted in Fig. 4.1 and Fig. 4.2. Similarly to the confined compression test [Burlion et al., 2001], the slight deformation $\varepsilon_{\theta\theta}$ of the confinement is proportional to the pressure on the inner surface of the confinement (with the hypothesis of small strain and linear elastic behavior of the glass confinement). Analytical relations can achieve the translation of strain into contact pressure. However, an experimental calibration gives directly the relation. The inner part of the tube is filled with pressurized water up to 45 bar. A pressure transducer measures the fluid pressure while the strain gauges measure the confinement deformation. A linear relation is found between the pressure and the deformation. Because of the discrepancy in alignment and quality of bonding, each of the 4 gauges has a different

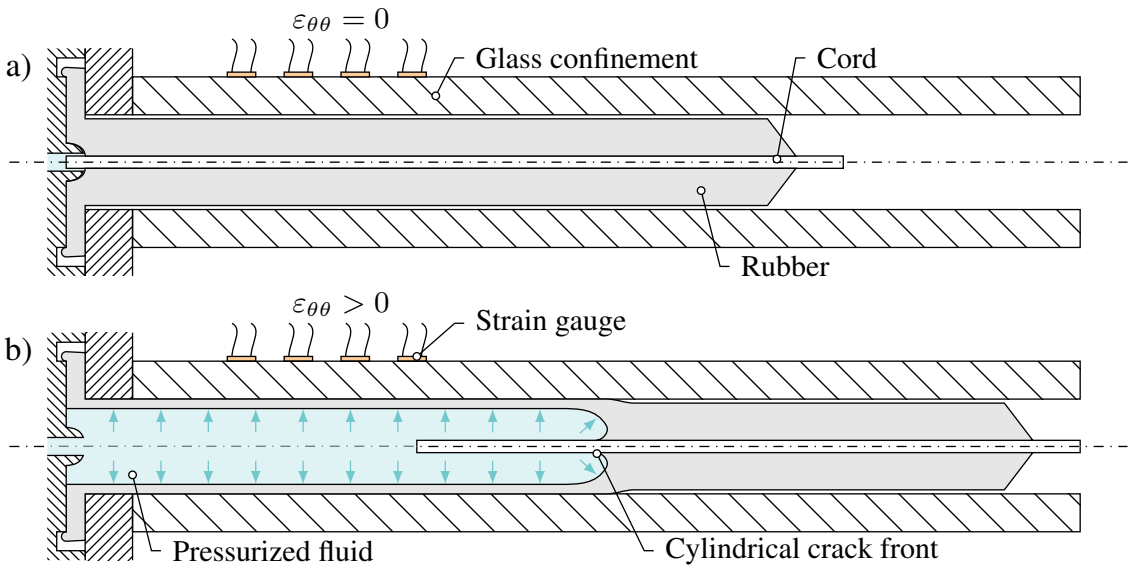

Figure 4.1: Section of the Rubber Cord Adhesion Inflation Test in a) initial configuration and b) pre-crack length inflation regime.

deformation-pressure factor. Then, the contact pressure given by each gauge is measured. Because of the high rigidity of the glass tube (10 mm thick borosilicate tube), a possible contact pressure gradient is naturally averaged. Therefore, the contact pressure is averaged between the 4 gauges to improve the measure and get a standard deviation from the apparatus. Each gauge has a separated quarter-bridge measured with a National Instrument® 9219 acquisition card. The acquisition from gauges, pressure transducer, displacement sensor of the plunger, and the camera are synchronized.

For the proposed data analysis to be valid, the longitudinal expansion of the specimen should not be constrained so that lubricant is used to prevent any friction between the rubber and the tube. As evidenced below insufficient lubrication could drastically change the crack nucleation and propagation conditions and render the analysis of the experimental results very complex. To monitor the test conditions, white markers are deposited on the specimen surface along the longitudinal direction to evaluate the longitudinal elongation. This technique has been implemented to validate the steady-state crack propagation regime assumption and evaluate the length of the accommodation region between the cracked and bonded parts [Corbel et al., 2022]. Similarly, the test protocol is now used to evaluate the influence of lubrication conditions.

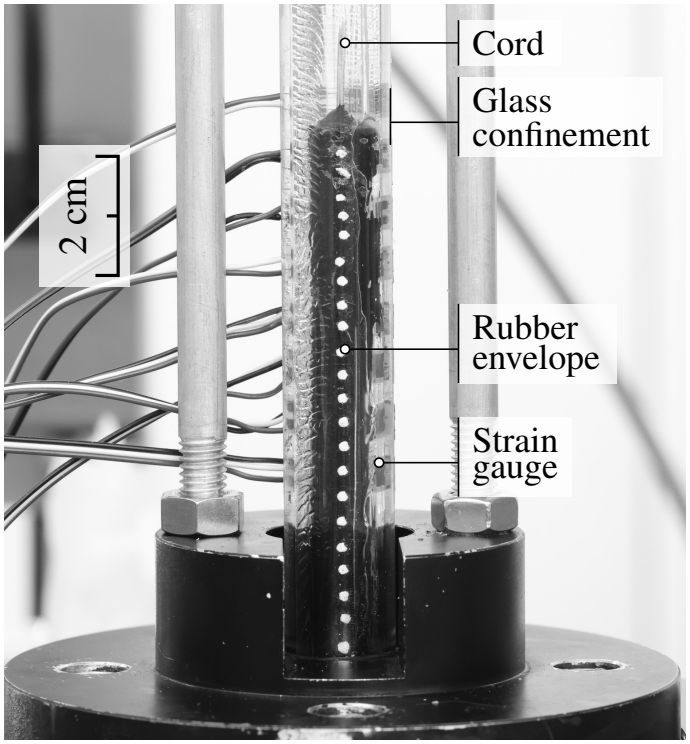

Figure 4.2: RCAIT apparatus with strain gauge glued on the glass confinement (strain gauges are on the back of the tube - riddles on the confinement tube are the grease).

4.2.2 Evidence of contact friction effects

Following the same procedure detailed in [Corbel et al., 2022], a series of specimens from the same manufacturing batch is tested under the same conditions but considering different lubricants. Two different silicon lubricants are tested. Their typical static viscosities are 4.9×10^{-4} m²/s for the Silicone Grease from CRC® (designed G490 hereafter), and 7×10^{-4} m²/s for the SAPPHIRE® Aqua-Sil from ROCOL® (designed G700 hereafter). Then, the two other contact conditions are a dry contact and a wet contact.

Evidence of friction effect appears on the specimen axial elongation at the end of the test in Fig. 4.3. The silicon-lubricated case shows similar elongations between the pre-crack at $\lambda_z = 1.9$ and the crack region at $\lambda_z = 2.1$. The wet contact shows an elongation gradient in the pre-crack region, ranging from 1.4 to 1.9. This reveals a sliding friction contact in this case. Meanwhile, the crack region reaches an elongation of 2. The dry case shows the lowest elongation at 1.1 in the pre-crack region and 1.7 in the crack region. The contact with dry friction blocks the axial elongation.

Fig. 4.4 resumes the experimental result, with the global inflation curve. Firstly, in the pre-crack inflation regime, all curves are superimposed before the contact of the

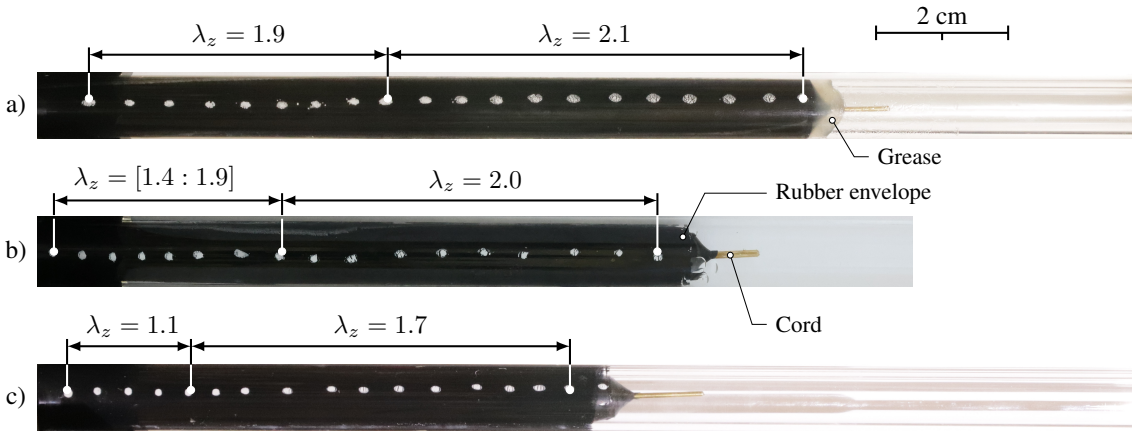

Figure 4.3: Comparison of deformed specimens at the end of the propagation regime for a) Silicon G490 lubricated contact, b) water contact, and c) dry contact. The specimen is divided into the pre-crack region on the left and the crack propagation region on the right.

rubber envelope and confinement tube. Then, discrepancy appears depending on the lubrication condition, with the steepest evolution for the dry condition. This behavior matches with the measure of axial elongation λ_z in Fig. 4.5. Before the contact, the rubber envelopes expand axially. Then, it either blocks totally in case of dry friction or continues to expand axially for wet or lubricated conditions. The contact is directly deduced from the blocking of axial elongation with a dry contact test or is given by the strain gauges in lubricated contact. Meanwhile, the wet contact shows a strong variation of axial elongation on the pre-crack region (significantly higher than the standard deviation of the marker following method). The elongation is growing gradually from the bottom to the tip of the pre-crack length. It is an intermediate contact condition between a grease-lubricated contact and a dry contact.

Secondly, during the crack propagation regime, a plateau of pressure is observed in all conditions in Fig 4.4. The plateau corresponds to the critical pressure to crack propagation, in a self-similar manner [Corbel et al., 2022]. For all contact conditions, the critical pressure is similar. The mean elongation during the cracked part of the specimen is reported by markers in Fig. 4.5. The elongation in propagation is similar for the three lubricated cases at $\lambda_z = 2.1$, while dry contact is slightly lower at $\lambda_z = 1.8$. Fig. 4.6 reports the axial elongation on the outer surface of the specimen after total propagation, with axial coordinate in the initial configuration. The local elongation is reported for all specimens of each contact condition. The pre-crack region is under 50 mm, with 15 mm hidden from sight by the test apparatus (see Fig. 4.2). The water

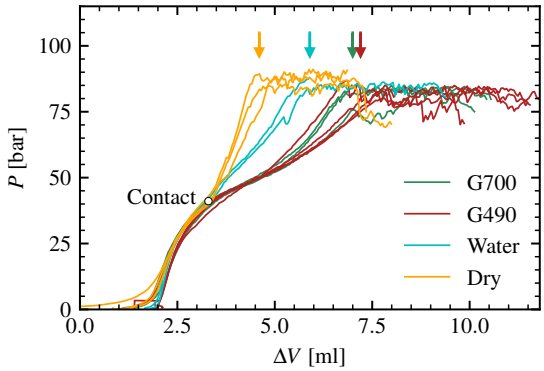

Figure 4.4: Comparison of inflation curves for 4 contact conditions, with repeatability (arrows indicate the start of the propagation regime).

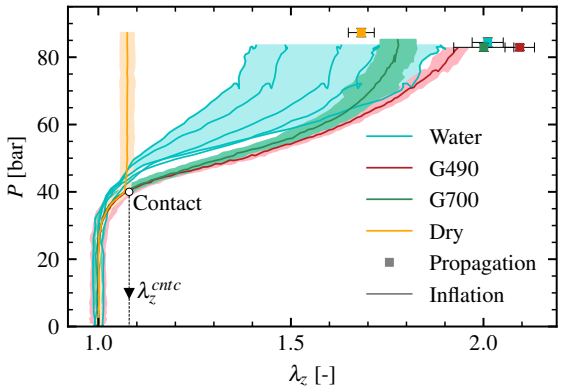

Figure 4.5: Comparison of elongation variation during the primary inflation regime and the mean elongation during propagation for 4 contact conditions.

lubrication condition generates a significant gradient of elongation in the pre-crack region, while the other condition remains constant. The elongation during propagation is very different from the elongation at the end of the pre-crack inflation regime for the dry contact. Therefore, the blocking effect of dry contact happening in the pre-crack inflation regime decreases or stops in the propagation regime.

To shed some insight on the interaction between the contact condition and the rubber envelop inflation, both analytical and numerical modeling are proposed.

4.3 Modeling friction effects during RCAIT

First, an analytical model is proposed to quantify the friction effect during the inflation regime only. Then, a finite element model evaluates the friction effect during both inflation and crack propagation regimes.

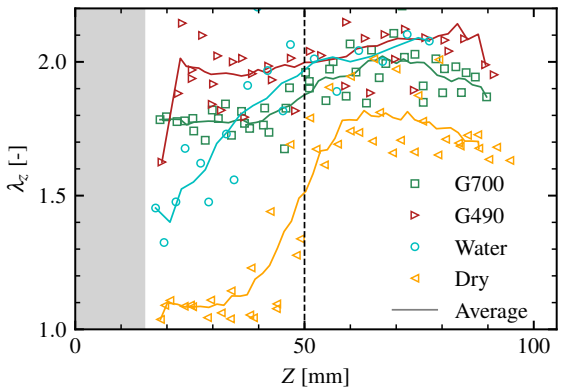

Figure 4.6: Distribution of axial elongation after crack propagation with different lubrication conditions and multiple samples (undeformed configuration). The grey area corresponds to the bottom of the sample hidden by the test apparatus.

4.3.1 Analytical evaluation in inflation regime

The mechanical analysis of the RCAIT is founded on a semi-analytical modeling of the free or constrained expansion of the rubber envelope due to the application of inner pressure (TTRIM: Thick Tube Rubber Inflation Model). However, during the confined regime, while the radial expansion is limited by the confinement tube, the longitudinal expansion is possible due to the frictionless contact assumption. The analysis is valid in the crack region of the specimen far from the specimen clamping and crack tip position so that it reduces to a one-dimensional problem.

The same analysis can be used but changing to boundary conditions to consider the possible presence of friction force on the rubber envelope as depicted in Fig. 4.6. Indeed, the presence of friction forces requires the presence of contact pressure and is induced by the trend of the specimen to expand axially. The presence and extent of the accommodation region between the bonded and inflated region of the specimen is visible during the test by observing the longitudinal elongation with the marker monitoring technique or simply by observing the variation of the specimen's outer diameter. However, the evolutions of contact pressure and friction force between the specimen and confinement tube are not known. Assuming, the friction forces are developing along a finite distance from the crack tip, then the same TTRIM model can be adapted to evaluate the mechanical response of the rubber envelope far from the accommodation region only by modifying the boundary conditions.

The following considers the axisymmetric expansion of a thick incompressible hyperelastic tube. The inner and outer radius in the nondeformed state are respectively

R_{int} and R_{ext}. An internal pressure, P_{int}, is applied to the tube until the outer surface touches a confinement tube whose inner radius is equal to R_{conf}. In the deformed configuration, the internal and external radius of the rubber envelope are respectively equal to r_{int} and r_{ext}. During the unconfined inflation regime and once the contact is established between the rubber envelope and the confinement tube, an axial elongation, λ_z, of the specimen is observed which is supposed to be uniform through thickness. This longitudinal expansion is due both to the incompressible nature of the material and to the pressure applied on the closed end of the tube. In the following, a cylindrical coordinate system will be used, the position in the initial non-deformed configuration is defined by coordinates (R,Z). In the inflated configuration, only radial and axial displacements are observed due to axisymmetry. The current position in the deformed configuration is given by coordinates (r,z). The material elongations in the tube are then given by Eq. 4.1.

$$\lambda_r = \frac{\mathrm{d}r}{\mathrm{d}R} \quad \text{and} \quad \lambda_\theta = \frac{r}{R} \quad \text{and} \quad \lambda_z = \frac{z}{Z} \tag{4.1}$$

In the following, the rubber material is supposed to be incompressible so that the condition $\lambda_r\lambda_\theta\lambda_z = 1$ should be fulfilled. Considering, that the length of the homogenous inflated tube region is large (approx. 50 mm), a constant should be obtained. Then, explicit expressions for the radial evolution of principal stretches can be obtained [Skala, 1970] in Eqs. 4.2, 4.3, and 4.4.

$$\lambda_r^2(r) = \frac{1}{\lambda_z}\left[\frac{cr^2-1}{cr^2}\right] \tag{4.2}$$

$$\lambda_\theta^2(r) = \frac{1}{\lambda_z}\left[\frac{cr^2}{cr^2-1}\right] \tag{4.3}$$

$$r = \sqrt{\frac{1}{c} + \frac{R^2}{\lambda_z}} \tag{4.4}$$

The kinematic of the tube expansion problem then depends only on two parameters, λ_z and an integration constant, c, which are determined from the boundary conditions. While the unconfined regime leads to a complex characteristic equation to be solved to obtain the two integration constants, the confined regime is described by only kinematic conditions. Then direct expressions of the two integration constants are obtained as a function of the tube inner radius evolution [Skala, 1970] in Eqs. 4.5, 4.6.

$$\lambda_z = \frac{R_{ext}^2 - R_{int}^2}{R_{conf}^2 - r_{int}^2} \tag{4.5}$$

$$c = \frac{R_{ext}^2 - R_{int}^2}{R_{ext}^2.r_{int}^2 - R_{conf}^2.R_{int}^2} \tag{4.6}$$

Other dimensions (initial radii and inner confinement tube radius) are given quantities. Then, the stress equilibrium equation and material behavior are introduced. In the axisymmetric configuration, the stress tensor reduces to only three principal components σ_{rr}, $\sigma_{\theta\theta}$ and σ_{zz} in the radial, circumferential, and axial directions respectively, and the equilibrium equations reduce to Eq. 4.7.

$$\frac{\mathrm{d}\sigma_{rr}}{\mathrm{d}r} + \frac{\sigma_{rr} - \sigma_{\theta\theta}}{r} = 0 \tag{4.7}$$

The rubber being incompressible, stress components can be split into deviatoric and spheric terms in Eq. 4.8.

$$\sigma_{ii} = -\sigma_h(r) + \lambda_{ii}\frac{\partial W}{\partial \lambda_{ii}} = -\sigma_h(r) + s_{ii}(r) \tag{4.8}$$

With σ_h being the hydrostatic pressure and where the additional term is derived from a hyperelastic strain potential W. In the following, the Exp-Ln model [Khajehsaeid et al., 2013] will be used since it was found the most adequate to fit both the tube inflation and uniaxial response simultaneously [Kane et al., 2021]. The elastic potential is given in Eq. 4.9.

$$W = K\left[\frac{1}{p_1}\exp(p_1(I_1-3)) + p_2(I_1-2)(1-\ln(I_1-2)) - \frac{1}{p_1} - p_2\right] \tag{4.9}$$

with K, p_1, p_2 the material parameters and $I_1 = \lambda_1^2 + \lambda_2^2 + \lambda_3^2$ the first invariant of the right Cauchy-Green tensor. The introduction of the hydrostatic pressure radial variation in the stress equilibrium Eq. 4.7 results in Eq. 4.10.

$$\frac{\mathrm{d}\sigma_h}{\mathrm{d}r} = \frac{\mathrm{d}s_{rr}}{\mathrm{d}r} + \frac{s_{rr} - s_{\theta\theta}}{r} \tag{4.10}$$

Under confined inflation regime condition, the through-thickness elongation evolutions are set from Eqs. 4.7 and 4.6. Then analytical expressions of $\delta\sigma_{ii}$ evolutions can be found which depend on the chosen material behavior and related expression of the potential W. The radial evolution of the hydrostatic pressure is obtained by integrating Eq. 4.10, resulting in Eq. 4.11.

$$\sigma_h(r) = \sigma_h(r_{int}) + \delta\sigma_h(r) \tag{4.11}$$

With $\delta\sigma_h(r)$ defined in Eq. 4.12.

$$\delta\sigma_h(r) = s_{rr}(r) - s_{rr}(r_{int}) + \int_{r_{int}}^{r} \frac{s_{rr} - s_{\theta\theta}}{u} \mathrm{d}u \tag{4.12}$$

and $\delta\sigma_h(r_{int})$ is a last integration constant to be determined. In the case of frictionless contact between the tube and the rubber envelope, the static equilibrium between the axial force due to the pressure of the fluid applied to the close end of the tube and the cohesive axial stress in the envelope should be assessed. This boundary condition leads to the Eq. 4.13.

$$2\pi \int_{r_{int}}^{r_{ext}} \sigma_{zz}(u)\mathrm{d}u = P_{int}\pi r_{int}^2 \tag{4.13}$$

with P_{int} being the pressure of the fluid in the tube. Combining Eqs. 4.12 and 4.13 an integral expression of the integration constant $\sigma_h(r_{int})$ is found in Eq. 4.14.

$$\sigma_h(r_{int}) = \frac{2}{r_{ext}^2 - r_{int}^2} \left[\int_{r_{int}}^{r_{ext}} s_{zz} u \mathrm{d}u - P_{int} r_{int}^2 \right] \tag{4.14}$$

which is determined numerically. Finally, the both inner pressure from the injected fluid and outer pressure at contact are determined with Eq. 4.15.

$$\sigma_{rr}(r_{int}) = -P_{int} \quad \text{and} \quad \sigma_{rr}(r_{ext}) = -P_{ext} \tag{4.15}$$

Other quantities such as elongations and stresses are obtained with Eq. 4.2, 4.3, 4.4, and 4.8. First, let us consider the sliding contact reference condition. The simulations are performed by considering the free expansion condition and then the confined expansion regime to determine the evolution of inner and external pressure as a function of tube expansion as defined with the longitudinal elongation value.

A particular emphasis is necessary to reproduce correctly the experimental $P_{int}(\lambda_z)$ curve and the correct elongation at contact λ_z^{cntc} with the TTRIM. The elongation at contact influence heavily the tube inflation behavior in the presence of friction. Therefore, the identification of the strain potential uses a minimization of square root error on P_{int} [Corbel et al., 2022] with an addition of a weighted error on λ_z^{cntc}. The identified parameters are $K = 2.43\,\mathrm{MPa}$, $p_1 = -1.91$ and $p_2 = -0.545$. Fig. 4.8 compares the analytical prediction with experimental results (all 4 samples for contact condition G490). Before the contact, the unconfined inflation solution (UIS) predicts no contact pressure. After the contact, the confined inflation solution (CIS) predicts a rise of contact pressure. The predicted evolution of external pressure is similar to the experiment and validates the identification strategy in Fig. 4.9.

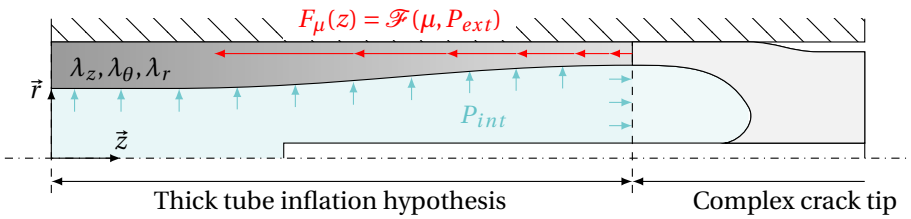

Figure 4.7: Representation of the tangential force introduced by the Coulomb friction model on the inflation of the rubber envelope in the pre-crack region.

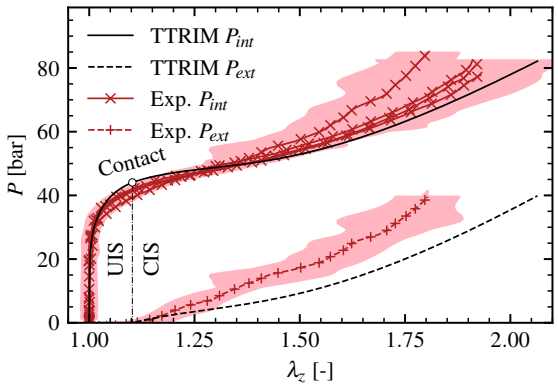

Figure 4.8: Tube inflation reference pressure-elongation solution compared to experimental results (contact condition G490).

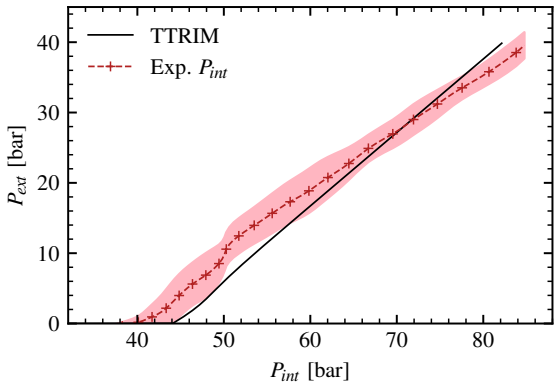

Figure 4.9: Tube inflation reference internal-external pressure solution compared to experimental results (contact condition G490).

Now, the presence of additional tangential forces along the specimen should be introduced. They can be attributed to friction. In the following, we assume the thick tube inflation kinematic remains valid so that the shear deformation due to the tangential forces along the specimen is negligible. The boundary condition in Eq. 4.6 remains applicable but Eq. 4.13 is valid only at the closed end of the tube which corresponds to the limit of the length along which the contact is established between the rubber envelope

and the confinement tube. Then, due to the interaction between the confinement tube and the rubber envelope, the axial cohesive stresses fluctuate as the internal radius and the longitudinal elongation according to Eq. 4.16.

$$\frac{\mathrm{d}}{\mathrm{d}z}\left[2\pi\int_{r_{int}}^{r_{ext}}\sigma_{zz}(u)u\mathrm{d}u - P_{int}\pi r_{int}^2\right] - \|\mathrm{d}F_z\| = 0 \tag{4.16}$$

Then discrete approximation of Eq. 4.16 can be used to evaluate the increment Δz corresponding to a given variation of rubber envelope expansion condition in Eq. 4.17.

$$\Delta z = \frac{2\pi\left[\int_{r_{int}(z+\Delta z)}^{R_{conf}}\sigma_{zz}(u)u\mathrm{d}u - \int_{r_{int}(z)}^{R_{conf}}\sigma_{zz}(u)u\mathrm{d}u\right] - P_{int}\pi\left(r_{int}^2(z+\Delta z) - r_{int}^2(z)\right)}{0.5\left[\mathrm{d}F_z(z+\Delta z) + \mathrm{d}F_z(z)\right]} \tag{4.17}$$

For all positions, the inner pressure remains the same and corresponds to one of the fluid used for inflating the specimen. The position z along the friction contact region is obtained by performing a cumulative sum of all Δz increments. The position along the non-deformed configuration is obtained by performing the cumulative sum of $\Delta Z = \Delta z/\lambda_z$.

We assume simple Coulomb's friction law is applicable as given by Eq. 4.18.

$$\|\mathrm{d}F_z\| \leq \mu 2\pi R_{conf} P_{ext} \tag{4.18}$$

When tangential relative displacement is present, Eq. 4.18 reduces to equality, and Eq. 4.17 becomes Eq. 4.19.

$$\Delta z = \frac{2\pi\left[\int_{r_{int}(z+\Delta z)}^{R_{conf}}\sigma_{zz}(u)u\mathrm{d}u - \int_{r_{int}(z)}^{R_{conf}}\sigma_{zz}(u)u\mathrm{d}u\right] - P_{int}\pi\left(r_{int}^2(z+\Delta z) - r_{int}^2(z)\right)}{\mu\pi R_{conf}\left[P_{ext}(r_{int}(z+\Delta z)) + P_{ext}(r_{int}(z))\right]} \tag{4.19}$$

Fig. 4.7 presents the model to take into account the friction effect. The tangential force exerted by the Coulomb contact model can be introduced in the TTRIM as an additional axial force $-F_\mu\vec{z}$ [Holzapfel et al., 2001]. In frictionless contact, the total axial force $F_z\vec{z}$ acting on a tube section is only the pressure acting on the closed end of the tube. The additional axial force $-F_\mu\vec{z}$ tends to decrease the inner deformed radius and axial elongation. Therefore various scenarios of tube inflation conditions will be examined for an inflation pressure in the range of 44 to 80 bar with varying axial force. 80 bar corresponds to the critical pressure plateau P_C which leads to rubber/cable decohesion observed in Fig. 4.4. As discussed before, the problem is entirely defined

once the inner pressure and inner and outer radius are set. All possible configurations are evaluated considering confined expansion condition (viz. $r_{ext} = R_{conf}$) and $R_{int} < r_{int} < r_{int}^{max}$ where the maximum value corresponds to the lubricated reference regime. These results are presented in Fig. 4.10, Fig. 4.11, Fig. 4.12.

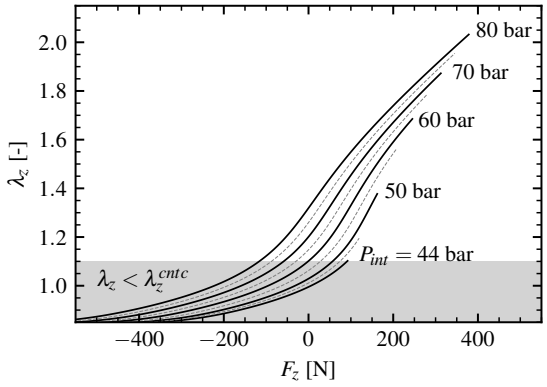

Figure 4.10: Analytical variation of the axial elongation with the total axial force for different inflation pressures (each dashed line is an intermediate pressure).

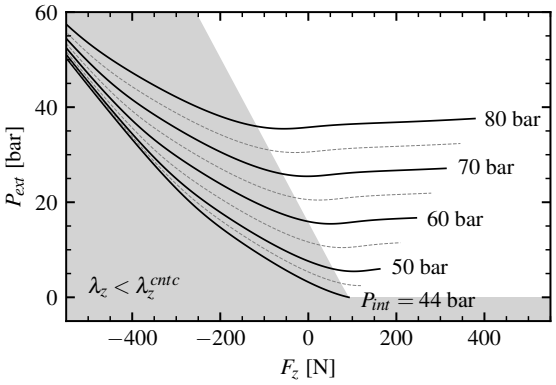

Figure 4.11: Analytical variation of the contact pressure with the total axial force for different inflation pressures (each dashed line is an intermediate pressure).

Not all configurations presented should be observed in real situations. The highest total axial force on each curve corresponds to the reference case. The diminution of F_z by the friction force acting in the opposite direction F_μ decreases the axial elongation and the internal radius. However, the axial elongation cannot be inferior to the axial elongation at contact. The grey areas on the three figures correspond to impossible situations.

Integrating Eq. 4.19 into the different inflation cases of Fig. 4.10, Fig. 4.11, Fig. 4.12 results in the evaluation of the sliding friction length in Fig. 4.13, Fig. 4.14. An

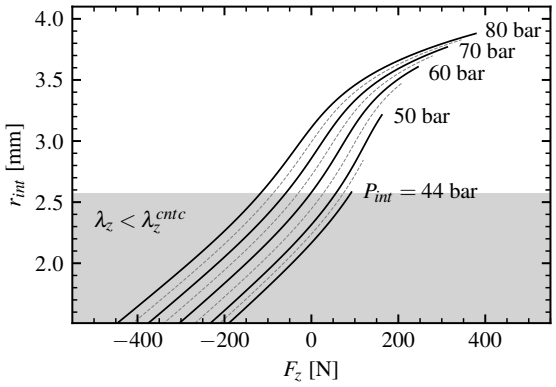

Figure 4.12: Analytical variation of the deformed internal radius with the total axial force for different inflation pressures (each dashed line is an intermediate pressure).

axial elongation gradient appears for all inflation pressure. The material being incompressible, a similar gradient of the internal radius is introduced in Fig. 4.14. For both quantities, the sliding friction length decreases in the undeformed configuration.

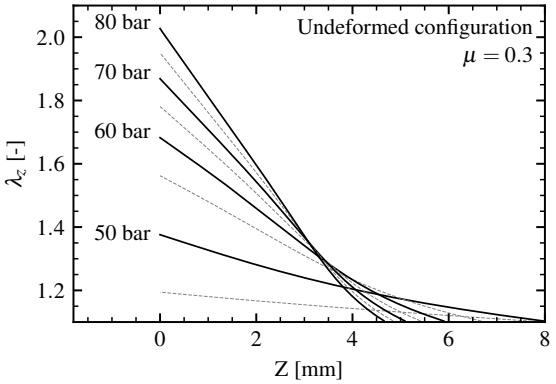

Figure 4.13: Variation of axial elongation in the sliding friction zone for different inflation pressures (each dashed line is an intermediate pressure).

Fig. 4.15 presents the sliding friction length at equal pressure for multiple friction coefficients. The axial elongation gradient length increases with the decrease of friction (both in undeformed and deformed configurations). Considering the RCAIT specimen dimension, any gradient of elongation is significant over the 35 mm measurement area. Even with a friction coefficient as low as 0.01, the analytical model predicts a friction effect in the inflation regime.

The present analytical model solves directly the friction problem. Nonetheless, an extension to iterative computation for variable friction coefficient is possible.

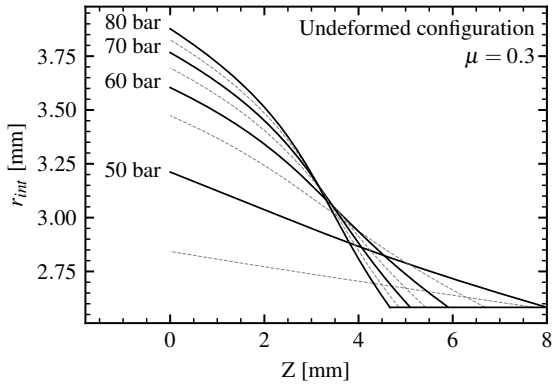

Figure 4.14: Variation of internal radius in the sliding friction zone for different inflation pressures (each dashed line is an intermediate pressure).

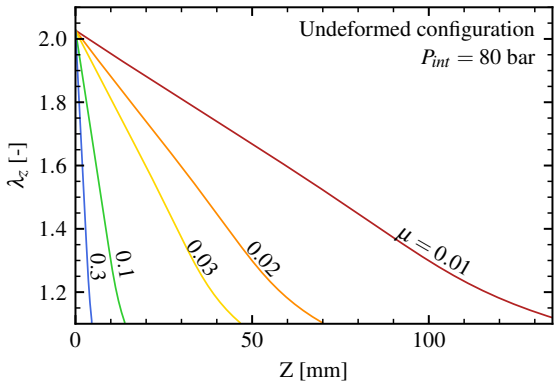

Figure 4.15: Analytical prediction of the axial elongation variation in the sliding friction length for different friction coefficients.

4.3.2 Finite element evaluation in inflation and propagation regime

The previous analytical modeling can address only the inflation regime. A thick tube inflation hypothesis cannot describe the complex deformed shape at the crack tip. During the propagation, the rubber envelope comes into contact with the glass tube as the crack advances. Therefore, a transient finite element modeling of both inflation and propagation regimes is needed. The cohesive zone model proposed previously [Corbel and Jumel, 2023] offers a predictive simulation of the whole experiment (more details of the model in chapter 3). The geometry and the material constitutive law correspond to the analytical model. In the following, the response of the model to varying friction coefficients on rubber envelop-confinement contact is studied. The goal is to reproduce and understand the modification of deformation in friction contact conditions during the propagation phase. The friction model of the contact between rubber

and confinement is Coulomb's model.

Fig. 4.16 presents the global inflation curves for different contact friction coefficients. The different curves are identical before the contact between the envelope and the confinement. Then, each case exhibits a different global compliance. The reference frictionless model with $\mu = 0$ exhibits the most compliant response. With the contact friction, the response becomes more rigid with a higher friction coefficient, up to the limit case of $\mu = \infty$. The pressure plateau during propagation is similar between all cases, a slight increase appears with the increase of friction coefficient.

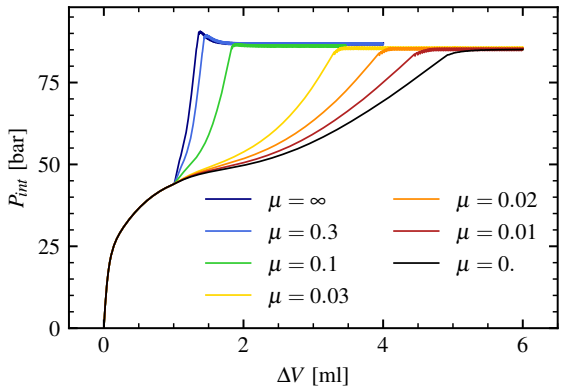

Figure 4.16: Numerical global inflation curves for different friction coefficients.

On the axial elongation distribution at the end of propagation, Fig. 4.17 presents different gradient of λ_z in the pre-crack region ($Z < 50\,\text{mm}$). The steepest gradient corresponds to the highest friction coefficient value. The axial elongation gradient then decreases with the decrease of μ. In all cases, the axial elongation is uniform in the propagation region ($Z > 50\,\text{mm}$).

Fig. 4.18 presents a close view of the axial elongation map in a radial section of the sample at the end of the inflation regime and after crack propagation. The gradient of axial elongation in the pre-crack region is set at the end of the inflation regime and remains still after crack propagation. Meanwhile, the rubber section delaminated after the crack advance exhibits the highest axial strain value compared to the pre-crack region. It is a consequence of the deformation shape at the crack tip that allows an important axial elongation before coming into contact.

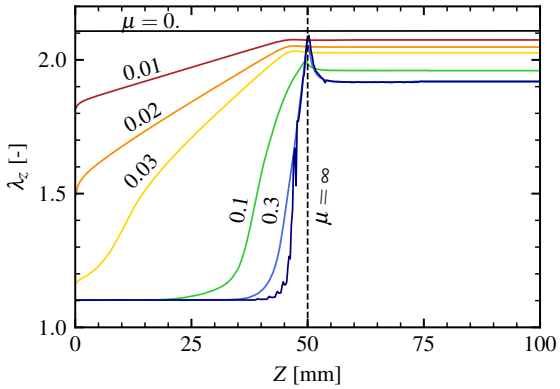

Figure 4.17: Numerical prediction of axial elongation distribution on the exterior surface of the sample after crack propagation with different Coulomb's friction coefficient (undeformed configuration).

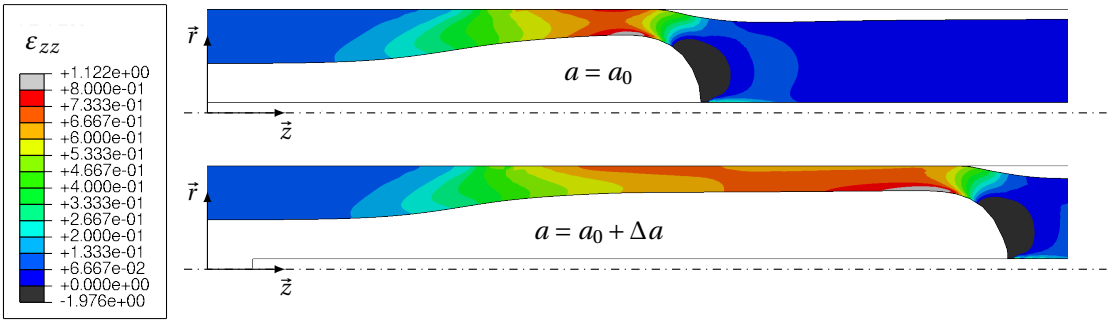

Figure 4.18: Map of the axial strain at the end of the inflation regime ($a = a_0$) and after crack propagation ($a = a_0 + \Delta a$) with friction coefficient (deformed configuration).

4.3.3 Scaling of sliding friction length

Eq. 4.19 exhibits a linear scaling of the displacement increment with the friction coefficient μ. Fig. 4.19 presents the numerical, analytical, and experimental results with the scaling. The value of μ corresponds to the value fixed for the numerical simulation. For the analytical model, all the curves of Fig. 4.15 collapse exactly. However, for the experimental results, the friction scaling is identified to fit the numerical curves. For the dry friction condition, μ is equal to 0.2 and for the wet friction condition, μ is equal to 0.04. A slight discrepancy appears between the numerical curves and the analytical curve. The position of the transition from the tube hypothesis to the complex crack front (see Fig. 4.7) is fixed arbitrarily at the undeformed pre-crack length. It explains the shift observed between the numerical and analytical models. Then, the analytical model, and therefore the μ scaling, supposes a tube model kinematic without any

shear deformation. For a μ above 0.1, the shear components become large enough to deviate from the proposed scaling. Nonetheless, the experiment and both models are in accordance considering the experimental deviation.

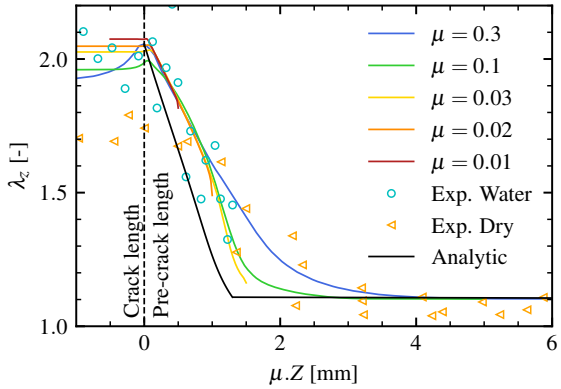

Figure 4.19: Comparison of numerical, analytical, and experimental axial elongation variation in the normalized sliding friction length.

4.4 Discussion

The experimental results show a clear dependence on contact conditions during the RCAIT. The major impact is in the pre-crack inflation regime where the friction can prevent the axial elongation of the rubber envelope. A clear gradient of elongation in the pre-crack region is seen in dry and wet contact conditions in Fig 4.6. This gradient is well modeled by both the analytical (Fig 4.15) and numerical (Fig 4.17) models. Moreover, a scaling law shows the λ_z gradient in the friction sliding length is inversely proportional to the Coulomb friction coefficient μ in Fig 4.19. From this analysis, the wet and dry contact conditions agree well with the analytical and numerical models of the classic Coulomb friction model. The identified friction values at 0.04 and 0.2 respectively for the wet and dry conditions are below the values reported in the literature on sliding contact between black carbon natural rubber and glass. For dry contact, values range from 0.3 [Gong et al., 1999] up to 2 [Tuononen, 2016]. The friction coefficient for soft material is reported as dependent on material visco-elastic dissipation [Wu et al., 2021] and surface roughness [Devalba et al., 2018, Xu et al., 2013]. Contrary to most tribology-focused experiments, the surface of the rubber envelope in RCAIT comes into contact with the glass in an already stressed/deformed configuration. This deformed surface rugosity effect plus the error from the identification procedure of μ

(e.g. the error between the analytical inflation model and the experiment in Fig. 4.8) could explain the difference between the observed friction coefficient and the value from the literature.

The case of the 2 greases is similar with an homogenous axial elongation in the pre-crack zone ($Z < 50\,\text{mm}$ in Fig 4.6). Considering the models with a friction coefficient as low as 0.01 predict a theoretically observable axial elongation gradient, the two silicon greases create a frictionless contact condition. The lubrication performance can be attributed to the creation of elastohydrodynamic lubrication [Dong et al., 2023, Öngün et al., 2008, Schmidt et al., 2010, Zhao et al., 2019]: the rubber envelop squeeze and shear the grease during inflation, creating a continuous flow. And the grease flow creates a contact condition close to frictionless.

On the other hand, the consequence of friction on the propagation regime is negligible. All experiments' pressure plateaus are similar during crack propagation in Fig 4.4. A similar result is predicted by the numerical model in Fig 4.16. The pressure plateau is directly related to the critical strain energy release rate of the rubber-cord interface. The decrease of friction effect during propagation can not be addressed with the analytical model. The strain path in the rubber envelope during the propagation differs largely from an inflation tube kinematic [Corbel and Jumel, 2023]. Results from the finite element model give more insight into the friction effect on the kinematic at the crack tip. During the propagation, the rubber envelope delaminates from the cord and reaches a high axial elongation before contact with the confinement tube. Then, it either blocks the axial elongation totally for an infinite friction coefficient or allows some sliding depending on the friction coefficient value (see Fig 4.18). This state of deformation is possible thanks to the gap between the rubber envelope and the confinement tube.

4.5 Conclusion

The experimental development with strain gauges introduced in the study of friction effect permits an addition to the previous metrology. The combination of the contact pressure and the axial elongation measurements enhances the material identification and ensures the correct inflation kinematic. It is key to model correctly the friction effect.

The experiment and the two models conclude on the significance of the friction

effect. The initial inflation regime is affected by limiting the axial elongation of the rubber envelope in case of friction. The effect is the apparition of an axial elongation gradient on the upper part of the pre-crack length. The size of this sliding friction length varies in $1/\mu$ as presented by a simple scaling law. Thus any slight friction effect is visible with the marker following technic. The two tested silicon greases with different viscosity give a homogenous axial elongation in the pre-crack length zone and validate the frictionless hypothesis.

On the propagation regime, both numerical and experimental results show the robustness of the test. All tested contact conditions result in a steady-state crack propagation. The analysis of the numerical model shows that the gap between the confinement tube and the elastomeric envelope accommodates enough of the crack front region to let the rubber envelope expand axially before coming into contact. Finally, the critical pressure plateau, which gives the G_C between the rubber envelope and reinforcement cord, is similar between all tested conditions.

Mode mixity effect 5

P.-Y. Corbel, J. Jumel
"Characterization of the interface fracture energy dependency on mixed mode fracture between rigid fiber and soft matrix"
published in Journal of Mechanics and Physics of Solids, in press (2024)

An enhanced version of the Rubber Cord Adhesion Inflation Test (RCAIT) has been designed to experimentally assess the internal pressure and cable tension applied to the specimen needed to propagate a crack along the matrix/reinforcement interface. To calculate the critical strain energy release rate, we develop a semi-analytical model describing the deformation of a hyperelastic tube under loading conditions that reflect the ones applied experimentally. A more comprehensive numerical model of the test is also proposed to investigate the influence of loading conditions on rubber deformation near the crack tip. Comparison of different experimental data sets with the theoretical/numerical data demonstrates that the new experimental setup allows for a reliable determination of the rubber/cord interface failure envelope under combined loading conditions.

5.1 Introduction

Like other polymers, elastomers are mixed with particle fillers and reinforcements of diverse shapes, sizes, and types. This process aims to finely adjust and enhance their overall performance in terms of processability, durability, and thermal and mechanical properties. The inclusion of reinforcements allows for increased stiffness, strength, and toughness of materials, meeting the requirements of demanding applications including tires, anti-vibration components, piping, cables, medical prostheses, smart

materials, and adhesives. The choice of particles, fibers, cables, or fabric materials must ensure compatibility with the polymer matrix to achieve the necessary adhesion between constituents. Indeed, this parameter significantly influences the failure modes and ultimate mechanical performances, particularly in terms of strength and toughness [Beter et al., 2020, Bonneric et al., 2019, Luo et al., 2023]. Continuous efforts are being made to improve the reinforcement/polymer interface quality and the properties of the interphases formed within the polymer. This is achieved through surface treatment and conversion processes, in addition to new polymer chemistry compatible with more restrictive regulation [Crowther, 2001]. However, adequate characterization tools, especially those related to mechanical properties, are crucial for assessing the adhesive performance of these interfaces and supporting ongoing developments. This study aims to introduce a more versatile test protocol for characterizing the adhesion between fibrous reinforcement and an elastomer matrix, and more specifically the bonding between drawn steel wires and rubber, which are the components of tires. Currently, there are only a few tests available. Pull-out tests, as proposed by [Gent et al., 1981, Nicholson et al., 1978] or described in standard procedures [Fielding-Russell et al., 1979], are generally used to assess adhesion between elementary filaments and the matrix [Meng and Chang, 2020]. Additionally, peel or shear tests are conducted on reinforced rubber plies to complement the data [Rao et al., 2004, Su et al., 2021]. New experimental developments in this field are scarce.

Nonetheless, a test inspired by the confined pressurized blister test [Dannenberg, 1961], named Rubber Cord Adhesion Inflation Test (RCAIT), has been developed recently with the sole purpose of evaluating the adhesion between a fibrous reinforcement and a polymer matrix, specifically an elastomer. During the RCAIT, a pressurized fluid is injected into the interface between the matrix and the reinforcement to initiate and propagate a crack. The test specimen is obtained by embedding a single cord along the axis of a cylindrical rubber envelope. To prevent the rubber through-thickness failure and force the decohesion to propagate along the rubber/cord interface, the specimen is placed in a transparent rigid confinement tube that restricts the radial expansion of the rubber tube. Considerable effort has been made to refine the test protocol and analysis to consolidate the energy balance analysis used to calculate the critical Strain Energy Release Rate that governs the crack propagation condition. The main limitation of most existing tests is the inability to precisely control the interface loading conditions. Indeed, the stress distribution is significantly affected by

various experimental parameters such as specimen geometry, component mechanical properties, specimen loading conditions as well as experimental artifacts such as friction between the specimen and the fixture or between the cord and the matrix. Controlling and accurately predicting the mode mixity at the crack tip position is a challenging objective [Gent and Yeoh, 1982]. It is worth noting that the loading conditions applied to the interface in real situations may differ significantly from those encountered during pull-out tests [Pupurs and Varna, 2017]. This can be attributed to complex macroscopic loading, the effect of reinforced rubber layers' stacking sequence, or the interaction between the cords themselves [Bonneric et al., 2019]. A modification of the RCAIT is proposed wherein internal pressure is applied simultaneously but independently on the reinforcement/matrix interface, along with tension load on the reinforcement. This modification allows for adjustment of the mode mixity at the crack tip position.

This article provides a detailed analysis of a novel experimental setup, along with the presentation of the results from a first series of tests carried out on rubber/brass plated cord assemblies. The main objective is to demonstrate the ability of the test to establish a failure envelope indicating the stable crack propagation onset conditions as a function of the values of the injected fluid pressure and the tension applied to the cord. Following this, a mechanical model of the experiment is introduced to predict the deformation of the pre-crack specimen length considering combined axial loading, external (un)confinement, and internal pressure loading conditions. The energy balance analysis proposed for the classical RCAIT analysis is modified to account for the effect of axial tension and evaluate the strain energy release rate under these combined loading conditions. Moreover, supplementary finite element simulations are presented to clarify the relation between macroscopic and crack tip loading conditions.

5.2 Rubber / Cord Mixed mode adhesion test: RCAIT²

The RCAIT (see Figure 5.1) was originally proposed as an alternative to the traditional H-test and Gent's test [Gent and Yeoh, 1982] for characterizing the adhesion between a rubber matrix and a single cord, filament, or strand reinforcement. The original test protocol is described in [Kane et al., 2019], while subsequent improvements in the test fixture design and instrumentation are given in [Corbel et al., 2022]. The test specimen is obtained by curing a cylindrical rubber envelope around the cord in a mold so that

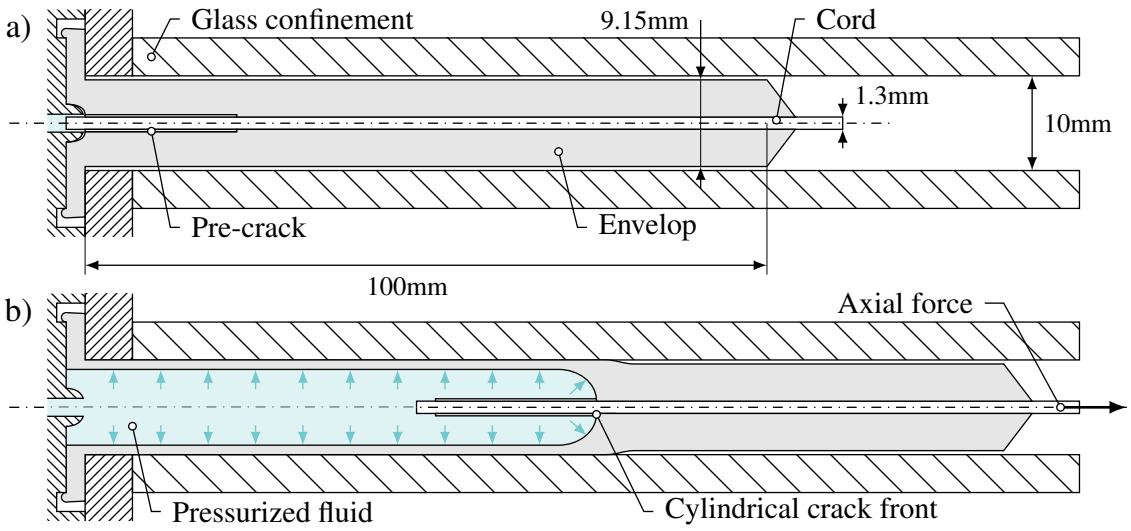

Figure 5.1: Section of the Rubber Cord Adhesion Inflation Tension Test configuration in a) initial configuration, b) mixed inflation-tension pre-crack regime.

the cord is located along the axis of the specimen. An anti-adhesive coating is applied to one side of the specimen to produce an artificial initial decohesion, the rest of the cord adheres to the rubber during the rubber vulcanization process due to the formation of strong Cu_xS covalent bonds [van Ooij, 1984, van Ooij, 1979].

A flange is also formed on the pre-crack side of the specimen during molding so that the specimen can be tightly connected to a hydraulic circuit from which a pressurized fluid is injected. The fluid flows inside the rubber envelope along the interface, inflating the precracked length. To prevent any crack propagation through the thickness of the rubber sheath due to an aneurysm, the specimen is placed in a confinement tube which limits the radial expansion of the specimen. A suitable lubricant (CRC® Silicon grease) is used to prevent any friction between the rubber and the tube which could limit the axial expansion of the specimen. The fluid is slowly injected until a critical pressure is reached, resulting in a stable self-similar propagation of the rubber-cord interface decohesion. Finally, by measuring the critical pressure, crack propagation, injected volume, and rubber deformation during the test, the critical strain energy release controlling the extent of the decohesion can be determined.

5.2.1 Experimental setup

The stress state at the crack tip, and consequently the mode mixity ratio, is not controlled in the classical RCAIT test set-up, as it depends on the geometry of the speci-

men. To allow the mode mixity to be tuned, a second loading condition is applied to the specimen. In the RCAIT, the pressurized fluid is slowly introduced by pressing a high-pressure stainless-steel syringe with a tensile testing machine. In the proposed Rubber Cord Adhesion Inflation Tension Test (RCAIT²) configuration, the specimen fixture is now placed in the tensile testing machine to pull off the cord under constant displacement rate conditions. Before the start of the pull-off load, the pressurized fluid is released into the pre-cracked part of the specimen from a hydro-pneumatic accumulator which maintains the pressure constant throughout the test.

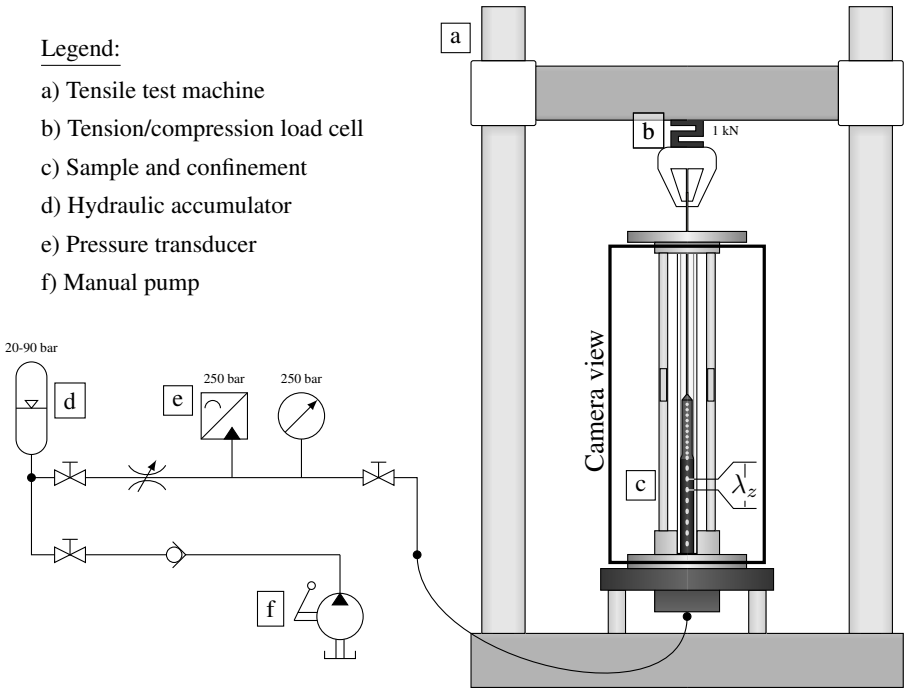

Figure 5.2: Experimental setup with the hydraulic line, tensile machine, RCAIT, and sensors.

A schematic view of the new setup is shown in Figure 5.2. To obtain the necessary experimental data and to control the test conditions, various sensors and equipment are added to the system. A manual high-pressure pump (VIRAX® 262005 – 100bar – 10 l) is used to fill the hydropneumatic accumulator, whose capacity is much greater than the volume injected into the specimen (1l vs 15 ml), thus ensuring a constant fluid pressure condition. A choke valve (Swagelok® SS-ORS2) is connected to the hydraulic circuit to release slowly the pressurized fluid. A pressure transducer (Swagelok® Model S Transducer – 250 bar) is also connected to the circuit to measure the fluid pressure during the test. Before the test, the hydraulic accumulator is filled with the appropri-

ate pressure of nitrogen gas, which controls the minimum fluid pressure injected into the specimen. The tensile testing machine is equipped with a load cell to measure the tension applied to the cord. White dot markers are also deposited along the specimen and the specimen is observed during the test with a digital camera. The position of each marker is then determined using the markers tracking technique, then by analyzing the evolution of markers' positions during the test, specimen elongation due to inner pressure and axial tension is determined so as the evolution of crack propagation during the test. A more detailed description of the metrological aspects of RCAIT is given in [Corbel et al., 2022]. The same methodology is applicable here when combined internal pressure and tension are applied to the specimen. In the following, a series of tests are performed to measure the evolution of the pull-out force during the stable crack propagation regime as a function of the injected fluid pressure. Then mechanical model of the sheave inflation is proposed to evaluate the value of the critical SERR which controls the crack propagation onset condition.

5.2.2 Results

A first series of tests are performed using the classical RCAIT protocol (no pull-out force, constant fluid injection rate). A typical fluid pressure vs injected fluid volume evolution is reported in Figure 5.3. Nonlinear evolution is observed during prior stable crack propagation regimes due to rubber hyperelastic behavior also leading to geometrical non-linearities. From the evolution of rubber envelope elongation, as a function of injected fluid pressure or using the evolution of injected fluid volume, the rubber mechanical behavior can be identified using a thick rubber tube inflation model. During the stable crack propagation regime, a stationary pressure evolution is observed. The mean pressure value is designated as the critical pressure, P_C, hereafter. The constant pressure is due to the steady-state nature of the crack propagation process. The measured critical pressure is equal to 83.1 bar with a standard deviation of 0.95 bar, the crack growth rate is controlled by the injection rate and equal here to 10 mm/min. When the process zone ahead of the decohesion reaches the end of the bonded length unstable crack propagation regime is observed as evidenced by the rapid pressure drop.

A second series of tests are then conducted using the novel RCAIT² configuration to evaluate the effect of an additional pull-out tension exerted on the cord. Figure 5.4 reports the typical pressure and pull-out force evolutions with time recorded during

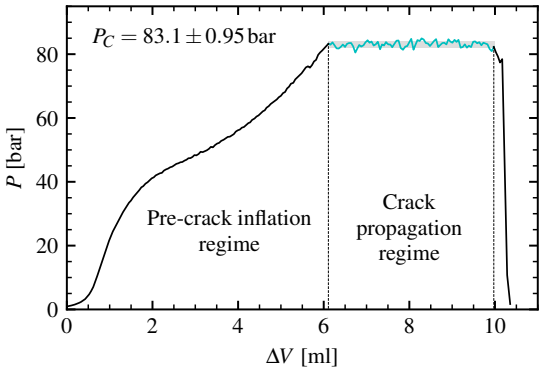

Figure 5.3: Typical experimental evolution of pressure with injected volume for a pure pressure RCAIT (flow rate at 1ml/min).

a RCAIT². First, the pressurized fluid is slowly introduced from the accumulator (20s < time < 40s) into the specimen by opening the hydraulic circuit as detected by the progressive increase of the inflation pressure. Once a stable P_C value is reached, the pull-out test procedure is started. The pull-out force reaches a peak value which indicates the onset of the stable crack propagation regime. Then stationary pull-out force is recorded while the fluid pressure also remains constant (150s < time < 270s) until the decohesion reaches the specimen end and the final fracture is observed. The instant crack length evolution is also recorded from marker displacement analysis [Corbel et al., 2022], (see fig. 5.5). The measured crack growth rate is 25mm/min which corresponds to the crosshead displacement speed value.

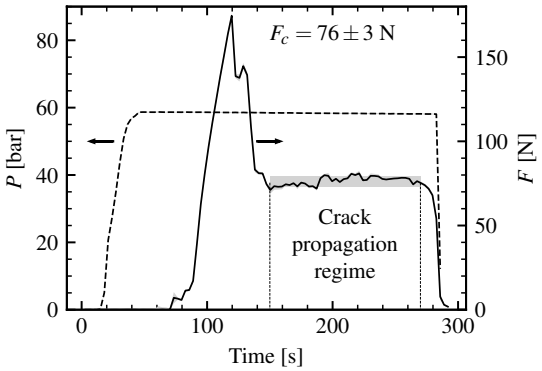

Figure 5.4: Typical experimental evolution of inflation pressure and external force with time for a mixed inflation tension RCAIT². The inflation pressure is set at 60 bar with the pressure accumulator (displacement rate at 15 mm/min).

Again, the stationary pull-out force and injected fluid pressure values recorded during the test suggest that the steady-state propagation hypothesis remains valid when a

supplementary axial force is introduced. Therefore, the analytical method developed to analyze RCAIT results should be adapted to introduce the effect of the axial force.

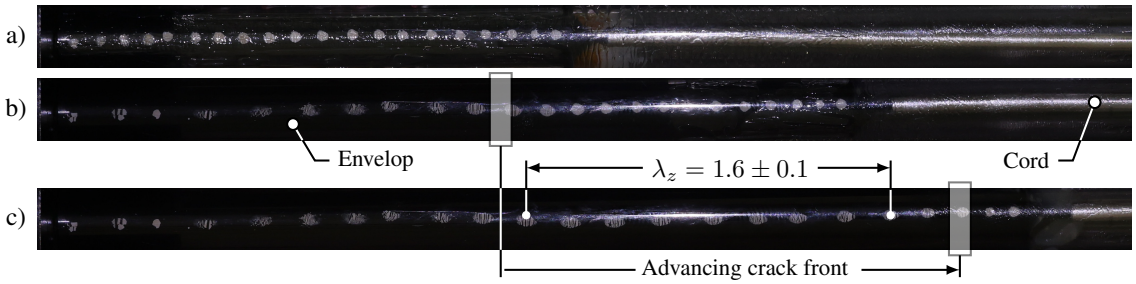

Figure 5.5: Markers on the outer surface of the specimen a) undeformed configuration b) start of the force plateau c) end of the force plateau. Inflation pressure at 60 bar and displacement rate at 15 mm/min).

5.3 Analytical model

The critical strain energy release rate is determined by performing a comprehensive energy balance of the crack propagation process, taking into account the work provided to drive the crack propagation, which is counterbalanced by various dissipative mechanisms. The framework applicable to RCAIT is primarily described in [Kane et al., 2019]. It takes advantage of the steady-state nature of the crack propagation process to establish a simple energy balance considering an infinitesimal extension of the crack length, δa [Pupurs and Varna, 2017]. Now, by introducing an additional external force, the new energy balance is given by equation 5.1.

$$\delta W_{tot} = P_{int}\pi\left(r_{int}^2 - R_{int}^2\right)\lambda_z\delta a + F_{ext}(\lambda_z - 1)\delta a = 2\pi R_{int}G\delta a + \delta E \tag{5.1}$$

The term, $P_{int}\pi\left(r_{int}^2 - R_{int}^2\right)\lambda_z\delta a$, corresponds to the work done by the injection of the pressurized fluid, $F(\lambda_z - 1)\delta a$, is the energy provided by the application of the tensile force to the cord. This energy is counterbalanced by the potential energy stored due to the deformation of the rubber, δE, and the effect of dissipative processes due to crack propagation, $2\pi R_{int}G\delta a$. It should be noted that G is an effective global quantity since at a macroscopic scale no distinction can be made between the local dissipative damage mechanisms at the crack front scale and those at a more global scale related to the whole envelope deformation. For the time being, the main issue in the analysis

of the test data is related to the evaluation of the potential energy stored in the rubber envelope, δE.

5.3.1 Constitutive equations

In the original version of the RCAIT, a Thick Tube Rubber Inflation Model (TTRIM) is derived and solved semi-analytically to simulate the expansion of the rubber envelope due to the application of internal pressure under unconfined and/or confined radial conditions. This model is now modified to introduce the application of an additional axial force. The kinematic of thick tube inflation is identical when combining inflation- and axial tension loading conditions [Holzapfel et al., 2001]. The TTRIM assumes incompressible rubber behavior and axisymmetric expansion of the cylindrical envelope in the cylindrical coordinate system, $(0,\vec{r},\vec{\theta},\vec{z})$. Assuming a constant elongation along $\vec{z}$, the elongations correspond to equation 5.2.

$$\lambda_r(r) = \frac{\mathrm{d}r}{\mathrm{d}R} \quad \text{and} \quad \lambda_\theta(r) = \frac{r}{R} \quad \text{and} \quad \lambda_z = \frac{z}{Z} \tag{5.2}$$

Thanks to these two main assumptions, the deformation of the specimen is completely determined in a large deformation framework by only two parameters [Skala, 1970]:

$$\lambda_r^2(r) = \frac{1}{\lambda_z}\left[\frac{cr^2-1}{cr^2}\right] \tag{5.3}$$

$$\lambda_\theta^2(r) = \frac{1}{\lambda_z}\left[\frac{cr^2}{cr^2-1}\right] \tag{5.4}$$

where, λ_z, $\lambda_\theta(r)$, and $\lambda_r(r)$ are the axial, circumferential, and radial expansion of the envelope respectively. c is an integration constant that will be determined from the boundary conditions for a given λ_z value. The radial position in the deformed state r is related to the radial position in the initial state R with the equation 5.5.

$$r = \sqrt{\frac{1}{c} + \frac{R^2}{\lambda_z}} \tag{5.5}$$

With the specimen deformation being preliminarily defined by the incompressible axisymmetric expansion problem, the Cauchy stress distribution through the thickness can be determined for a given hyperelastic behavior of the rubber envelope. The mechanical behavior of the rubber is defined by a hyperelastic strain potential function, $W(\lambda_r,\lambda_\theta,\lambda_z)$, the parameters of which can be determined directly from RCAIT test

data or alternatively from separate rubber characterization test methods. The Cauchy principal stress components, σ_i, are then given by the equation 5.6.

$$\sigma_i(r) = -\sigma_h(r) + \lambda_i \frac{\partial W}{\partial \lambda_i} = -\sigma_h(r) + s_i(r) \tag{5.6}$$

where σ_h is the hydrostatic pressure component and s_i are the principal deviatoric components. The expressions for s are obtained directly from the strain potential, W, using the expressions of the elongations given in equations 5.3 and 5.4. In the following, an Exp-Ln hyperelastic behavior [Khajehsaeid et al., 2013] is considered whose strain energy function is given by equation 5.7.

$$W = K\left[\frac{1}{p_1}\exp(p_1(I_1-3)) + p_2(I_1-2)(1-\ln(I_1-2)) - \frac{1}{p_1} - p_2\right] \tag{5.7}$$

Material parameters K, p_1, and p_2 are identified using the method depicted in [Corbel et al., 2022] and their values are respectively equal to 2.43 Mpa, -1.91, and -0.545.

The through-thickness evolution of $\sigma_h(r)$ is found by solving the static equilibrium constitutive equation. Using the previous notation, this reduces to equation 5.8.

$$\frac{\mathrm{d}\sigma_h}{\mathrm{d}r} = \frac{\mathrm{d}s_r}{\mathrm{d}r} + \frac{s_r - s_\theta}{r} \tag{5.8}$$

With:

$$\sigma_h(r) = \sigma_h(r_{int}) + \delta\sigma_h(r) \tag{5.9}$$

Then considering equation 5.9 and integrating equation 5.8 we obtain:

$$\delta\sigma_h(r) = s_r(r) - s_r(r_{int}) + \int_{r_{int}}^{r_{ext}} \frac{s_r(u) - s_\theta(u)}{u}\mathrm{d}u \tag{5.10}$$

Again, it should be noted that the entire stress and strain distribution in the hyperelastic and incompressible tube is controlled by only two geometrical boundary conditions, such as r_{int} and r_{ext}. The stress distribution is determined up to an additive constant, $\sigma_h(r_{int})$, due to the incompressible nature of the rubber, which is determined with the boundary applied to the closed end of the tube.

$$2\pi \int_{r_{int}}^{r_{ext}} \sigma_z(u)u\mathrm{d}u = P_{int}\pi r_{int}^2 + F_{ext} \tag{5.11}$$

In equation 5.11, the left term corresponds to the contribution of the longitudinal stress component in the rubber sheath, the static equilibrium is obtained by applying the pressurized fluid on the closed end of the tube, so that the axial force exerted

on the cord. After a few manipulations, the additive constant is obtained with equation 5.12.

$$\sigma_h(r_{int}) = \frac{2}{r_{ext}^2 - r_{int}^2}\left[\int_{r_{int}}^{r_{ext}} s_z(u)u\mathrm{d}u - P_{int}r_{int}^2 - F_{ext}\right] \tag{5.12}$$

The geometry of the specimen and confinement tube inner radius are also important input parameters of the model. In the following, the outer radius of the specimen rubber envelope is equal to $R_{ext} = 4.575\,\mathrm{mm}$, the cord radius is equal to $R_{int} = 0.65\,\mathrm{mm}$, the confinement tube is equal to $R_{conf} = 5\,\mathrm{mm}$ and the inner radius of = 5 mm (see Figure 5.1). Two different calculations should be performed to determine the strain and stress distribution in the elastomer envelope corresponding respectively to the confined and unconfined inflation regimes, due to the different boundary conditions encountered during the test. In the case of contact between the envelope and the confinement, the confined inflation solution (CIS) is obtained directly by using $r_{ext} = R_{conf}$ and using r_{int} as a control parameter to set the deformation of the rubber sheath. The axial force applied on the cord is then calculated as a function of the injected fluid pressure, considering $\sigma_r(r_{int}) = -P_{int}$ and using relations 5.8 and 5.11. In the unconfined inflation regime, the boundary condition, $\sigma_r(r_{ext}) = 0$, is again introduced, using r_{int} parameter. A Newton-Raphson procedure is then used to determine the r_{ext} value compatible with the loading condition (P_{int}, F_{ext}) applied to the specimen, as proposed in previous work [Kane et al., 2021], to find the unconfined inflation solution (UIS). A series of analytical simulations are then carried out using increasing applied axial force values for the constant pressure of the injected fluid, as would be done experimentally.

The results of the analytical simulation of the unconfined inflation regime are shown in Figure 5.6. The evolutions of the inner and outer cylindrical envelope radius are represented as a function of the tension applied to the cord for various fluid pressures. Three different behaviors are observed. 1) For low fluid pressure, both the inner and outer radius decrease due to the Poisson effect, as the tube is essentially in pure tension. For high fluid pressure values, the inner and outer radius values increase simultaneously. The tube sustains biaxial stresses and the reduction of the net cross section facilitates the diametral expansion due to the inflation pressure. During the transition between these extreme situations, first, the inner radius starts to increase with the tension applied to the cord, then the outer one. In the 56 bar < P_{int}< 59 bar range, the evolution of the outer radius with the tension applied to the cord is not monotonous. This behavior could be critical for the control of the test condition, since after the ap-

plication of the initial pressure, an unconfined situation should be observed, but then, during the progressive application of the tensile load, the contact between the envelope and the confinement tube is established.

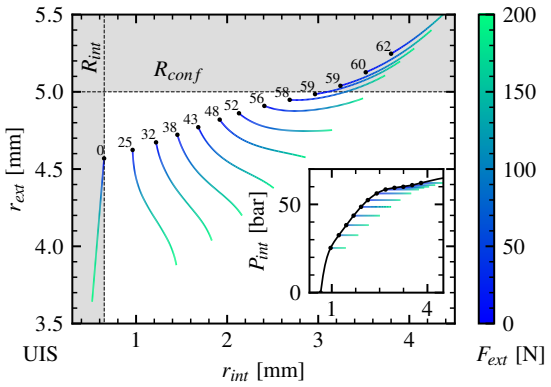

Figure 5.6: Variation of the external and internal deformed radius with external force application at different inflation pressures in the unconfined boundary condition. Corresponding evolution of inflation pressure with the internal deformed radius reported in the insert.

Figure 5.7 also illustrates the intermittent nature of the contact between the rubber envelope and the confinement tube. The evolutions of the applied tensile force as a function of the inner rubber envelope radius are reported for various constant values of the injected fluid pressure. A grey shaded area is added to distinguish the situations where there is no contact or confined expansion. For Pressure values close to 55 bar, the contact may be intermittent since the $r_{int}(F_{ext})$ evolution is tangent to the shaded area.

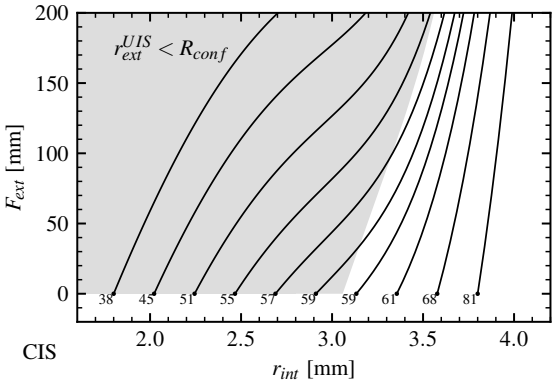

Figure 5.7: Variation of the internal deformed radius with external force application at different inflation pressures in the confined boundary condition. The grey area corresponds to the contact clearance predicted with the UIS.

We merge the UIS and CIS into the Mixed Inflation Solution (MIS) with the condition of contact $r_{ext} \geq R_{conf}$ in Figure 5.8.

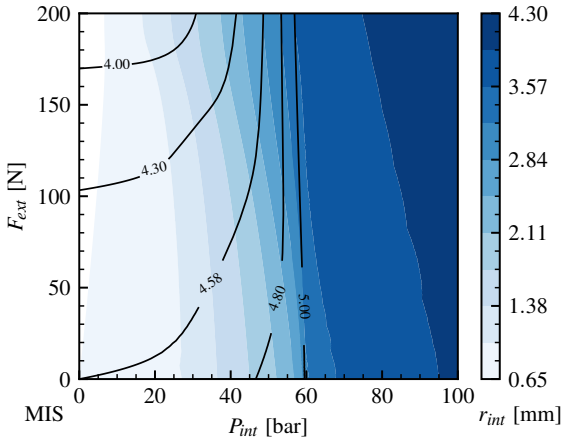

Figure 5.8: Variation of the internal deformed radius with inflation pressure and externally applied force from the mixed inflation solution. Black lines correspond to isovalues of external deformed radius from the UIS.

Using the confined or unconfined inflation/tension problem resolution to respect experimental condition, $r_{ext} < R_{conf}$, (mixed using inflation solution), the global energy balance analysis can be performed during the entire loading sequence to determine the Strain Energy Release Rate which controls the crack propagation condition.

5.3.2 SERR Computation

The RCAIT² aims to evaluate the critical SERR that drives the decohesion process at the rubber/cords interface under mixed-mode loading conditions. To achieve this, the TTRIM model can be used to evaluate all the terms required in equation 5.1 and determine the intensity of the dual loading condition, (P_{int}, F_{ext}), that causes the crack extension for a given critical SERR value, G_C. In equation 5.1, it is assumed that the overall behavior of the rubber envelope is hyperelastic and that dissipation is localized in the close vicinity of the rubber/cord interface. The potential energy stored in an infinitesimal length, δa, of the rubber envelope is then given by equation 5.13.

$$\delta E = 2\pi \int_{r_{int}}^{r_{ext}} W(r) r \mathrm{d}r \delta a \tag{5.13}$$

$W(r)$ is obtained using the equation 5.7 and the values of λ_r and λ_z determined with the equations 5.3 and 5.4. To complete the previous analysis, a series of analytical simulations were performed by varying F_{ext} in the interval [0-200]N and P_{int} in

the interval [0-100]bar to map the specimen deformation and determine all relevant boundary conditions and output parameters, such as r_{int}, r_{ext} and λ_z. Then using equation 5.1, G is calculated. Figure 5.9 represents with isovalue lines the evolution of the SERR as a function of the applied load F_{ext} and P_{int} combined a colormap representing the evolution of longitudinal elongation. The relation between the SERR and the applied load is highly non-linear due to the non-linearity of the specimen deformation. The evolutions differ depending on whether crack propagation would occur with unconfined contact conditions (at the left side of the blue line "Contact") or confined contact conditions (at the right side of the blue line). The SERR increases slowly with the pressure before contact and accelerates after. The addition of axial force increases the SERR for a given pressure similarly before and after the contact. The loading condition leading to an inner tube radius smaller than the one of the cord which would lead to friction contact in practice is indicated with the dashed area. Such a condition is observed for low fluid inflation pressure value which varies with the applied pull-out force. Such friction contact is due to the Poisson effect in the rubber. The axial elongation increases slowly before the rubber/tube contact occurs and remains almost constant along an iso-G line. However, a strong variation of axial elongation is predicted after the rubber/tube contact condition occurs at constant G when increasing the axial load. Following the constant G line (e.g. 50 kJ/m²) from the pure pressure case to the pure tension case, the axial elongation decreases with the increase of axial force. This counter-intuitive evolution is important to anticipate the specimen's behavior during the test. Indeed, under combined loading conditions, the crack propagation rate is proportional to the crosshead displacement by a factor of $(1-\lambda_z)$. The final λ_z value during the crack propagation regime is important to control the crack propagation rate.

The pull-out forces measured for various injected fluid pressures are reported in Figure 5.9 to evaluate the dependence of the critical SERR on loading conditions. The lowest fluid pressure used during this series of tests is equal to 20 bar but no plateau pull-out force evolution was observed during the crack propagation regime. For such a low inflation pressure value, an unconfined inflation regime is expected whatever applied pull-out force value together with a dramatic decrease of the specimen's outer radius but also eventually of the inner radius. Such abnormal pull-out force evolution indicates that friction contact is susceptible to develop under such low injected fluid pressure conditions. For all tested conditions, cohesive failure is observed, and

a residual rubber layer is observed on the surface of the cord for all tested conditions. Additionally, a larger residual rubber thickness is generally found at the initial crack tip position. Indeed, the crack initiation conditions differ from the crack propagation ones due to the presence of the PTFE insert used to obtain an artificial initial decohesion. In any case, the cord's radius underestimates the effective rubber sheath inner radius. Therefore, the dashed area indicates the loading conditions leading to friction contact between the rubber and the cord is certainly underestimated.

For all other test conditions plateau force evolution is observed together with a steady state crack propagation regime making SERR computation valid. The reference situation associated with only pressurized fluid injection indicates a 45.9 kJ/m² critical SERR value corresponding to a 83.1 bar critical pressure value. When smaller fluid pressure is initially injected, an additional axial force is needed to propagate the crack. However, by reporting the resulting (P_C, F_{ext}) in Figure 5.9 we observe that the combination of axial loading and inflation leads to reduce the critical energy release rate value from 50 kJ/m² to 20 kJ/m². A similar observation has been observed during peel tests by varying the peel angle [Liechti and Wu, 2001]. The prediction of axial elongation at 1.2 in UIS is similar to the experiments. Figure 5.9 reports the longitudinal elongations of the specimen measured with the marker monitoring technique. The observed elongations are close to the value predicted with the tube inflation model even if λ_z values are slightly overestimated. Again, this difference may be attributed to the underestimation of the rubber envelope's inner radius.

This combined theoretical and experimental analysis leads to the main conclusion that the critical SERR controlling the rubber/cord decohesion process under mixed mode loading conditions tends to decrease with increasing the pull-off force intensity until friction contact between rubber and cord occurs. A finite element model is then proposed to investigate the influence of macroscopic loading conditions on the local strain/stress distribution in the vicinity of the crack tip.

5.4 Finite element analysis

The simulation of the complete test procedure is a complex task. As a preliminary analysis, a simple elastic finite element (FE) simulation with a still crack tip position at the interface between the cord and the rubber sheath is considered here. The same Exp-Ln hyperelastic model as the one introduced in section 5.3 is used for the numerical

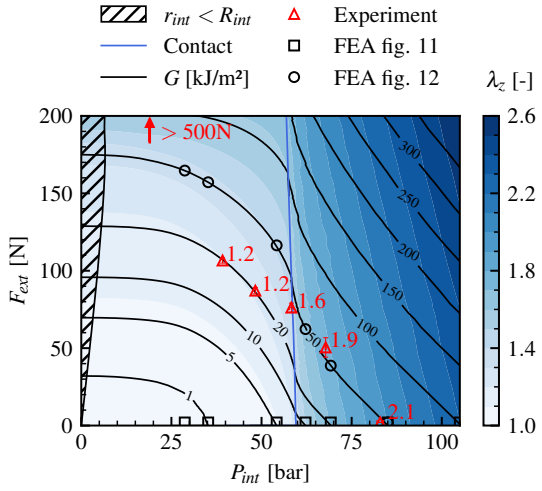

Figure 5.9: Mapping of axial elongation and strain energy release rate depending on the inflation pressure and external force. The "Contact" line corresponds to the transition from unconfined to confined boundary condition. Dashed area corresponds to the theoretical internal friction region. Continuous lines are at equal strain energy release rates. The number in red beside the experimental point indicates the axial elongation during propagation. The error bar corresponds to the standard deviation of the measured pressure and force plateau.

simulation to describe the mechanical behavior of the rubber. The cord is modeled as a rigid body. It is assumed that the resulting stress/strain displacement is representative of the one that would be observed during crack propagation despite the remaining rubber layer on the cord is not considered here. The boundary conditions and finite element mesh used as input for the Abaqus implicit solver are depicted in Figure 5.10. The axisymmetric assumption is used reducing the model to a 2D one and thus reducing the computational time. The longitudinal displacement is blocked on the bottom part of the specimen (viz. $u_z(z = -50\,\text{mm}) = 0$). Kinematic coupling is introduced to bond the rubber to the cord whose displacement along the longitudinal axis is not constrained. The confinement tube is modeled as a fixed rigid body. A frictionless contact condition (node-to-surface with penalty enforcement) is assumed between the confinement tube and the rubber envelope. Uniform pressure is applied to the inner surface of the rubber tube and an axial pull-out force F_{ext}, is applied to the rigid cord's right edge. A spiderweb mesh structure centered around the crack tip position is used using triangular elements with quadratic interpolation (CAX6H) in the vicinity of the crack tip position. Quadrilateral elements (CAX8H) with lower density are used far from the crack tip position where a more uniform stress and strain distri-

bution is observed.

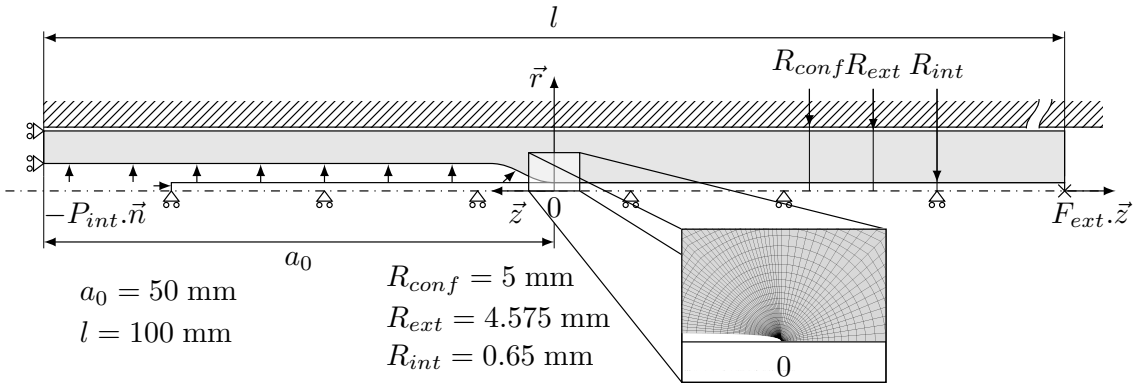

Figure 5.10: Finite element model of crack front analysis with geometry, boundary conditions, and mesh.

Detailed analysis of the near crack tip region will not be developed here but the results from the FE simulations will be helpful to discuss the effect of loading condition (P_{int},F_{ext}) on crack blunting. Figure 5.11 represents the evolution of the rubber crack lip shape in the vicinity of the crack tip under pure pressure loading conditions for various SERR values as determined with the method given in section 5.3. Two main effects should be outlined from this simulation. First, the crack tip angle between the rubber and the cord rapidly increases while the injection pressure increases. For high-pressure values, a blunted crack is obtained in the rubber rather than at the rubber/-cord interface. Similar effects have also been observed for an interfacial crack between a rigid and a neo-hookean body [Krishnan and Hui, 2009] sustaining plane strain loading conditions. Under such a configuration a strong shear stress distribution develops along the interface despite the crack being macroscopically loaded under mode I condition due to the incompressible nature of the rubber and the contrast between the metallic cord and rubber stiffness.

In Figure 5.12, the shapes of the rubber crack lip are shown for various combined loading conditions but leading to the same macroscopic $G = 50\,\mathrm{kJ/m^2}$ value which corresponds to the one measured experimentally under pure internal pressure loading condition. The application of an additional pull-out force makes the crack tip opening sharper and reduces the crack tip blunting phenomenon for an equal SERR, the internal deformed radius decreases.

Generally, the addition of the addition of axial force increases the crack tip angle, with the variation depicted in Figure 5.13. For a given SERR, i.e. $30\,\mathrm{kJ/m^2}$, the crack tip

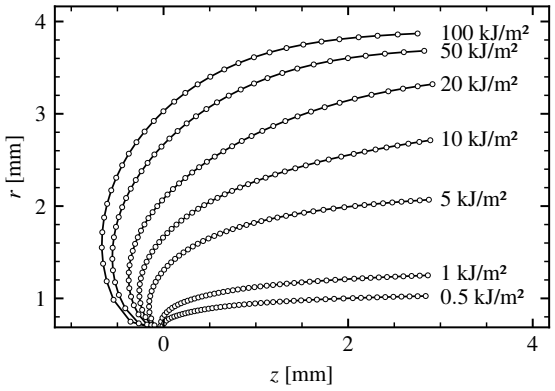

Figure 5.11: Comparison of crack tip opening profiles for an increasing strain energy release rate under pure pressure load.

angle can vary from 16° to 140° with the increase of axial force and decrease of inflation pressure.

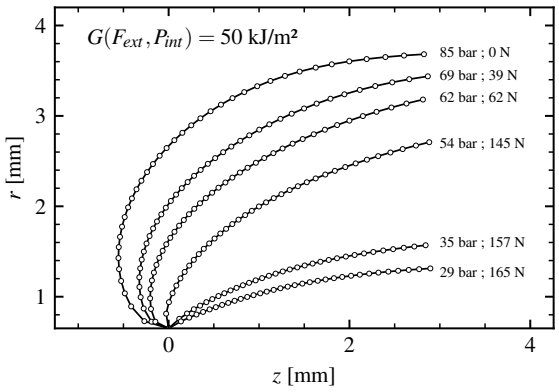

Figure 5.12: Comparison of crack tip opening profiles for a constant strain energy release rate with different pressure-tension load mixity.

The experimental data presented in Figure 5.9 are added in Figure 5.13 by computing the crack tip angle corresponding to the axial force and inflation pressure during crack propagation. The experimental SERR appears to decrease with the increase of the angle. An angle of 16° results in an experimental SERR of around 50 kJ/m^2, while at around 100°, the SERR decreases towards 20 kJ/m^2. Note that the experiments giving a higher crack tip angle, *i.e.* purely pull-out load, have an internal friction problem. The internal radius tends to decrease with the addition of axial force (see Figure 5.8) because of the thick-walled tube kinematic.

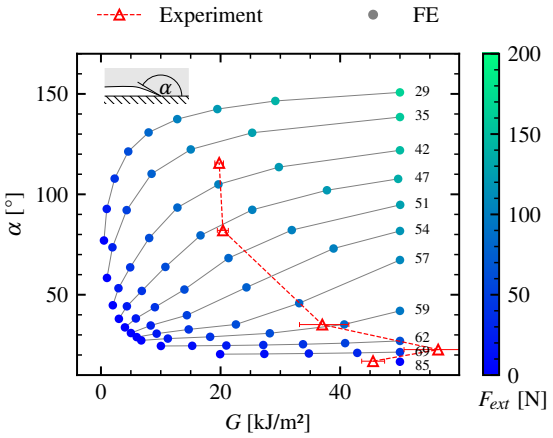

Figure 5.13: Variation of the crack tip angle from the finite element model with the strain energy release rate for multiple iso-P_{int} (corresponding pressure in bar) with an increasing axial force. The experimental critical strain energy release rate points are added with the corresponding crack tip angle computed numerically.

5.5 Discussion

The numerical results provide an insight into the load mixity influence on the crack tip hidden by the cylindrical rubber envelope. By balancing the inflation pressure and the axial force, multiple crack tip angles from 16° to 150° can achieved. The experiments exhibit a strong load mixity dependence, with G_C ranging between 20 to 50 kJ/m^2. Hence, reaching a specific crack tip angle appears difficult experimentally: α depends on both the proportion of pressure/force and the critical SERR. The RCAIT² can vary the crack mode mixity but cannot set it a priori. Furthermore, the geometry effect (i.e. smaller or larger R_{ext}) could modify the crack tip angle. For a flat configuration, the equivalent test would be the Peel test [Bartlett et al., 2023] with a variable peel angle. The peel angle is related to the crack mode mixity and gives a metric of the SERR dependence on load type (shear or opening). The crack tip is visible on the peel configuration while hidden on the RCAIT, the only solution being conducting a test under a X-ray scan. Nonetheless, applying the peel test to a cord geometry or a ply of cord is tedious and the result will be heavily dependent on the geometry (distance between cords in the ply, number of cords, true fracture surface). Furthermore, the RCAIT has the advantage of keeping the crack propagating at the interface when the failure is cohesive (i.e. a residual layer of rubber on the cord) thanks to the axisymmetry on small radius geometry.

On the crack tip morphology, the finger-like shape in pure inflation is pulled for-

ward by the addition of the axial force (Figure 5.12 and Figure 5.13). The variation of the crack tip angle could modify the crack surface position, transitioning from cohesive fracture for a low crack tip angle to adhesive fracture as it increases. The low crack angle keeps a singular stress [Krishnan and Hui, 2009] at the interface crack tip but locates a possible blunted crack away from the interface, which could explain the cohesive nature of the observed failure. However, without introducing a process zone with the correct physical length, a numerical model will not give the correct fracture morphology and behavior.

The fracture envelope in Figure 5.13 could be compared to an equivalent on the peel test, with an analogy between the crack tip angle and the macroscopic peel angle. Therefore, the observed variation of the experimental G with α is the rubber cord adhesion agrees with the variation of SERR with peel angle reported in the literature on the rubber peel test [Cook et al., 1997]. Establishing a common mode mixity metric between the peel test and the RCAIT² should however require much more experimental and numerical work, perhaps with a local approach.

5.6 Conclusion

A novel experimental setup is proposed to evaluate the critical SERR controlling the decohesion between a metal cord and a rubber sheath sustained mixed mode loading conditions. The novel test configuration consists is a combination of the RCAIT and pull-out tests. A semi-analytical model is derived to evaluate the specimen SERR under combined pull-out force and internal pressure loading conditions and take into confined or unconfined rubber envelope conditions during the crack propagation. A failure envelope characterizing the combined pull-out force and internal pressure values leading to stable crack propagation is obtained from a series of tests which exhibits a noticeable decrease of the critical SERR when the pull-out force contribution increases. However, for small internal pressure values, friction contact between the rubber and the cord is suspected leading to a large increase of the critical SERR which is not predicted with the actual model. Preliminary finite element analyses are performed to evaluate the influence of the combined loading condition on the shape of the crack tip which evidences that the crack tip angle decreases significantly with increasing injected pressure so that no stress singularity is observed anymore but blunted crack tip configuration. Due to the application of pull-out force, the crack tip angle is increasing,

and sharp crack tips are observed again which mostly explains the decrease of critical SERR under combined loading conditions.

The proposed RCAIT² is an original technique to evaluate the decohesion processes between a fiber reinforcement and a matrix. The rubber/cords configuration reveals complex effects leading to a complex failure envelope. Supplementary theoretical and experimental activities should now be engaged to achieve a better understanding of the damage and dissipative mechanisms in the vicinity of the crack tip which are involved in the failure process.

Pre-softening effect 6

6.1 Introduction

We study the influence of a pre-softening loading sequence on the rubber-cord adherence to evaluate the energy contribution of the Mullins dissipation during a rubber-cord adherence test. On bulk materials, the sample is easily softened by applying an initial load cycle prior to the fracture test [Diani et al., 2015, Qi et al., 2018]. However, on adhesion test, such as peel test [Bartlett et al., 2023] or blister test [Dannenberg, 1961], it is difficult to load the elastomer coating to produce pre-softening effect due to the planar geometry and due to the presence of the rigid substrate. However, a fiber adherence test geometry offers more range to soften the material, as demonstrated here with the RCAIT.

6.2 Adhesion on pre-softened samples

A fibre-matrix geometry [Gent and Yeoh, 1982, Kane et al., 2019] can offer a way to accommodate the material prior to the adhesion testing. The method is presented hereafter and the adhesion test to demonstrate the pre-softening effect on the interface fracture dissipation is the Rubber Cord Adhesion Inflation Test.

6.2.1 Experimental softening method

The diametrical compression of brittle materials is common to determine their fracture toughness (e.g. the Brazilian disk test). However, the application to soft materials is scarce, and limited to spheres [Shima et al., 1993, James et al., 2020]. The strain field is not homogenous and the friction between the plates and the sample creates uncer-

tainties, justifying the lack of interest for this configuration. Nonetheless, adding damage in a sample by compression before testing can be found in biological application [Fraser et al., 2021] to study injuries' effect on peripheral nerves' mechanical behavior. In the present study, the diametrical compression is only a means to perform specimen preconditioning procedure so that some Mullins dissipation would be produced without crack propagation occurs prior the interface crack propagation test.

Figure 6.1: Diametrical compression setup for 3 RCAIT samples, with the sample holder in white.

The experimental setup consists of a tension-compression machine (LLOYD LR5K) with compression plates and three RCAIT samples placed on the plateau, as illustrated in figure 6.1). This experimental arrangement of three samples is needed, in order to ensure the applied force is centred along the load load cell and to avoid any detrimental moment which would damage the apparatus. The specimen clamped part would obstruct the compression plate and working on one specimen only could create detrimental torque on the loading cell. The three-specimen configuration ensures the planarity of the upper compression plate. As the test machine is limited to 5kN, the compressed length of the specimen is adjusted to increase the Mullins dissipation in-

troduced in the section (full-length or half-length).Aa camera is placed in front of the specimen to observe the squashing of the transverse section.

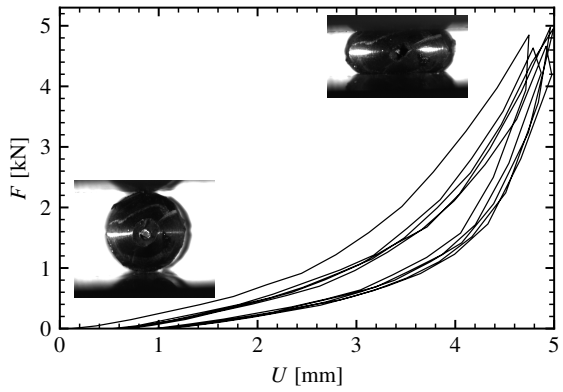

Figure 6.2: Experimental result of 5 compression cycles (compressed length = 25 mm).

Figure 6.2 presents the result of a cyclic compression test on a RCAIT sample. The compressed length is equal to 25 mm and the specimen has been already softened on a compressed length of 50 mm (but no video is recorded as the two other specimens block the view). A first hysteresis loop appears after the first load, then the material stabilizes on a viscous hysteresis. Therefore, the rubber envelope is softened by compression.

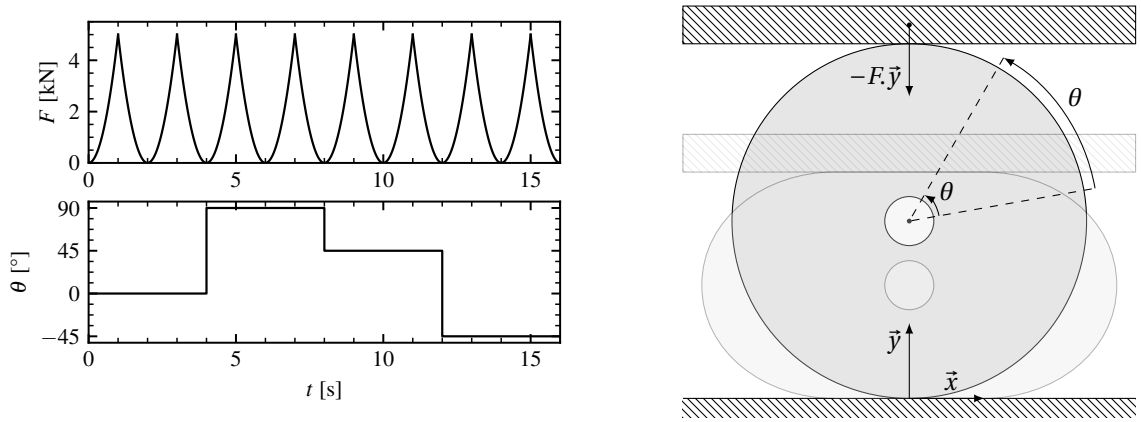

Figure 6.3: Loads F and rotations θ sequence applied to the RCAIT samples on a) and the axial view of the successive diametrical compression in the initial and deformed (drawn transparent) configuration on b).

A single simple cyclic diametral compression test will not introduce a homogeneous rubber envelope softening neither in the radial nor circumferential directions. While the radial softening will remain heterogeneous, a more axisymmetrical softening

distribution can be achieved by repeating the cyclic compression sequence for several specimen orientations. Figure 6.3 presents the sequence of compression and specimen orientation. The specific loading steps were derived from the numerical study of the test. The cycle is controlled by displacement rate with a cycle inversion based on force. The choice of force for the maximum compression is only based on practical considerations to reach the maximum force allowed by the test machine (limited to 5kN). One or two cycles are sufficient to introduce a majority of softening (see figure 6.2).

6.2.2 Adhesion results on softened samples

Directly after the softening preparation, the adherence between the cord and the softened rubber is measured with the RCAIT. Figure 6.4 compares the sample inflation curve for a reference sample and 2 softening conditions for a different batch of the specimen.

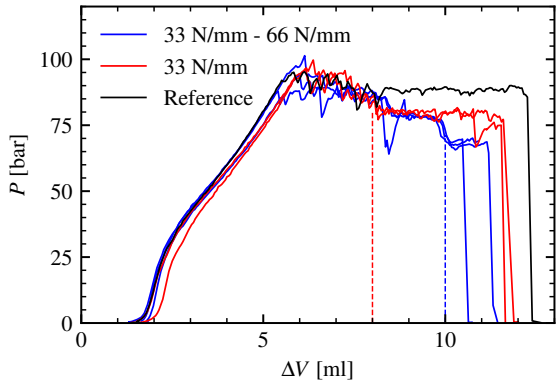

Figure 6.4: Compression setup for 3 RCAIT samples from a different batch of samples (propagating crack length is 70 mm instead of 50 mm).

The inflation curve exhibits pressure plateaus, correlated to a steady-state crack growth. No preload sequence is applies to the reference specimen. The second specimen (red line) is loaded along 50mm length (33 N/mm). The third specimen (blue) has been first loaded along 50mm as for the second specimen. Then to add supplementary softening, the same loading sequence is applied along 25 mm length (66 N/mm), resulting in 2 softened regions in the sample. Distinct plateau evolutions are observes which are correlated to crack propagation along distinct level of rubber envelope softening. As the pressure plateau is proportional to the critical SERR, the pre-softening

methods successfully suppressed (at least partially) the Mullins dissipation. Nonetheless, the energy balance with the non-softened behavior is no longer applicable to the results and needs an update.

6.3 Pre-softening in the energy balance analysis

To evaluate the effect of the pre-softening procedure on the recorded plateau pressure value during the RCAIT. The energy balance analysis is updated to consider the change in $P(\Delta V)$ curve due to Mullins dissipation. An energy balance analysis on a softened section of the specimen is proposed, with a numerical basis to retrieve the softening distribution caused by the diametrical compression in the rubber envelope. Unfortunately, due to manufacturing issues, the bulk rubber mechanical characterization was performed on a different kind of reference than the one used for manufacturing the RCAIT specimen. Therefore, while the overall methodology is valid, only qualitative and phenomenological comparison can be proposed here.

6.3.1 Rubber softening behaviour

An hyperelastic Exp-Ln [Khajehsaeid et al., 2013] is used to describe the hyperelastic response of the material as observed during monotonous loading test. The pseudo-elastic model of [Ogden and Roxburgh, 1999] is used for the hysteresis. The material parameters are identified on a cyclic uniaxial tension test presented in figure 1.3. Before identification, the residual strain observed at each cycle is shifted to 1, similar to the method in [Ogden and Roxburgh, 1999]. The identified values are resumed in table 6.1. The comparison between the simulation and experimental results is presented in figure 6.5.

A	a	b	r	m	β
1.14 MPa	-0.96	-0.91	1.73	0.63	0.10

Table 6.1: Parameters of the Exp-Ln strain potential (A, a, b) and the pseudo-elastic model (r,m,β).

The RCAIT configuration is also used to validate the model, by performing cyclic inflation test of the pre-crack rubber envelope to observe the hysteresis response. Figure 6.6 compares the experiments and the analytical model. The experiments are performed under constant flow rate condition up to maximum pressure then the pressure

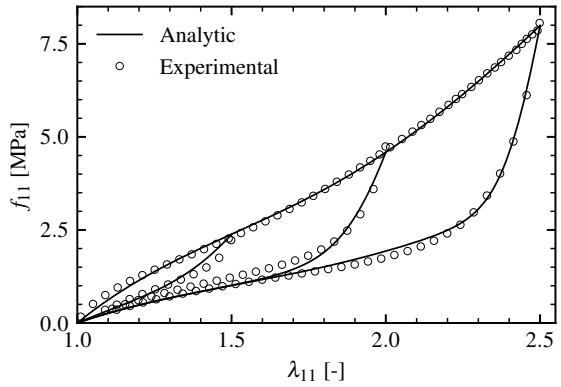

Figure 6.5: Comparison of experiment and model on cyclic loading in uniaxial tension at $\dot{\varepsilon} = 0.1\,\mathrm{s}^{-1}$.

is decreased to 0 bar. One sample is used for one cycle to avoid the marker's degradation and ensure reliable monitoring of the longitudinal stretch λ_z. The analytical model uses the same equation as presented in section 1.4.1, with the addition of the pseudo-elastic model during the stress computation. The η factor is simply applied to the deviatoric stress computation, knowing the maximum strain energy experienced locally by a material point W_{max} and the strain energy at the first loading W. As the stretch and strain energy varies along the radius, W_{max} and η varies also along the radius. The resulting model predicts correctly the cyclic inflation of a thick rubber tube with a radial distribution of softening in figure 6.6. The difference in the first loading path can be explained by the use of a limited set of data to identify the behaviour with respect to the complexity of the multiaxial loading conditions during the RCAIT. The discrepancy may also be attributed to the rate dependent behaviour which is not considered here at this step. The tube inflation has a radial-dependent stretch rate, with the highest rate on the inner radius, while the tension test is conducted at a constant stretch rate.

Despite, a very simple model is used here, the main features of the cyclic inflation curve are reproduced and satisfactory quantitative agreement is found.

6.3.2 Numerical computation of the softening

Finite element model

The diametrical compression test produces a complex stress and strain fields distribution in the specimen cross section. Therefore, the softening is also rather heteroge-

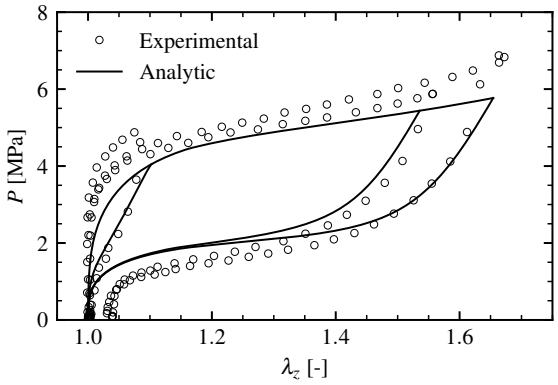

Figure 6.6: Comparison of experiment and model pressure-axial elongation response on cyclic inflation in on a thick rubber tube at $Q = 1\,\mathrm{mL/min}$.

neous. To estimate the softening created by cyclic compression, a 3D finite element analysis is proposed, considering the Exp-Ln potential [Khajehsaeid et al., 2013] and pseudo-elastic softening [Ogden and Roxburgh, 1999] to represent the material behaviour. The cord is modelled with a rigid solid, and the envelope is adhering to the cord surface through a kinematic coupling. The two compression plates are rigid and apply the load on the sample using surface contact condition (with Coulomb's friction $\mu = 0.3$). To ease the formulation of boundary condition, the cord is fixed in space ($\vec{U} = \vec{0}$) with rotation allowed only around the axial direction of the sample to model the rotation of the sample between successive compression. Thus, both the bottom and top plates move to produce a symmetrical loading. The maximum cyclic force and the compressed length of the specimen are representative of the experiments. The envelope is meshed with quadratic interpolation, full integration, and hybrid pressure-formulation elements.

The loading procedure is defined so as to specimen axis of symmetry are respected at each step. Then a good reproduction of the experiment by following the compression step in a specific order to guarantee symmetry of the specimen. The compression axis is first set to 0° then 90°, and then at -45° and +45°. Else, a succession of compression from -45°, 0°, +45°, and 90° creates some angular asymmetry of compliance, that would induce more shear strain in the envelop and less control over the softening field.

Numerical results

The resulting map of dissipated energy is presented in figure 6.7. The repartition of the softening is increasingly homogenous after each rotation and compression step.

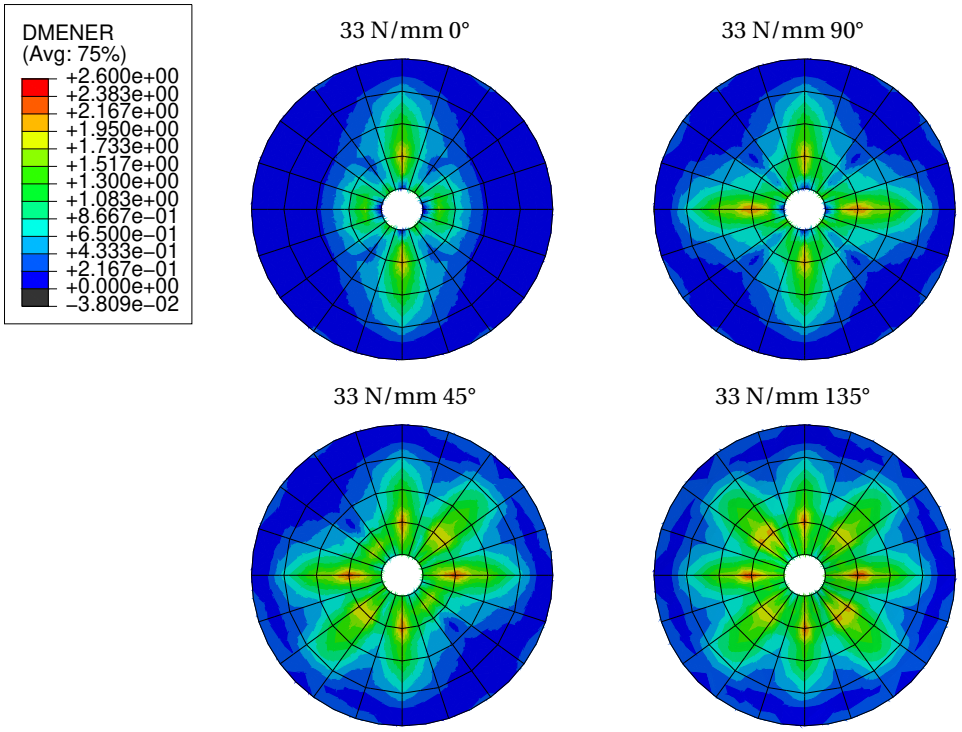

Figure 6.7: Mapping of the dissipated energy by softening $\phi(\eta_{max})$ (mJ/mm^3) on a section of the sample at the end of each compression step.

The distribution of damage is constant along the specimen cord, as illustrated in figure 6.8. The green surface corresponds to a level of damage density of 1 mJ/mm^3, encapsulating the major part of the damage by softening distributed in the sample.

Strain energy post-processing

The TRIM model assume axisymmetric distribution. Then, it is not capable to represent the effect of such complex radial and circumferential softening distribution. To reuse the results of the numerical compression, the output of interest is the maximum strain energy density W_{max}. The energy dissipated by damage $\phi(\eta_{max})$ is not directly imputable in our analytical model. As a first approach, the W_{max} fields in the rubber envelope are reduced first along the axial direction in the homogeneously softened region, resulting in the figure 6.9. Then to obtain an equivalent axisymmetric representation of the softening effect due to application of compressive steps, the angular mean of $W_{max}(x,y)$ fields reduce the distribution to solely radial $W_{max}(r)$, illustrated in figure 6.10. The angular standard deviation is a result of the compression procedure only along 4 directions. Adding other directions could improve the conformity of

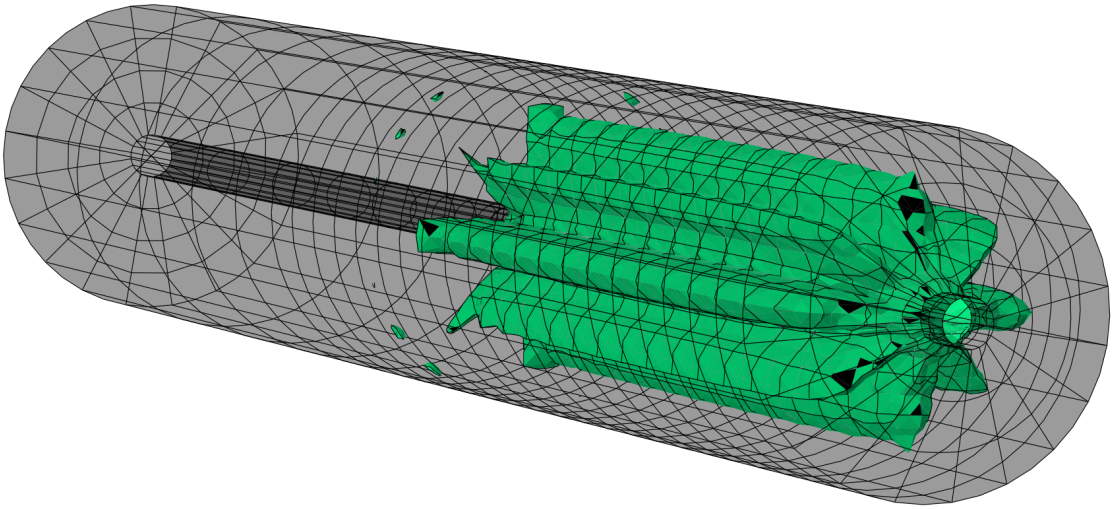

Figure 6.8: Surface contour at 1 mJ/mm^3 of the dissipated energy by softening $\phi(\eta_{max})$ after a cyclic compression level of 33 N/mm (specimen exterior surface in transparent black).

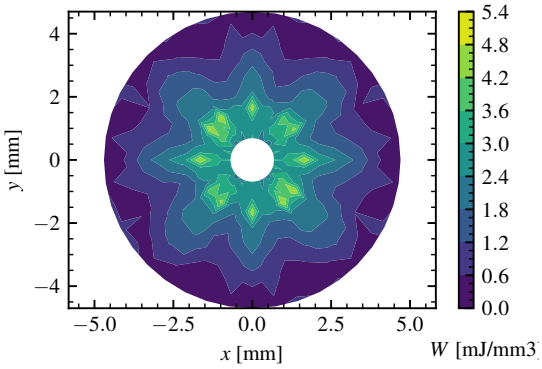

Figure 6.9: 2D variation of W_{max} in homogenous region for a compression at 33 N/mm.

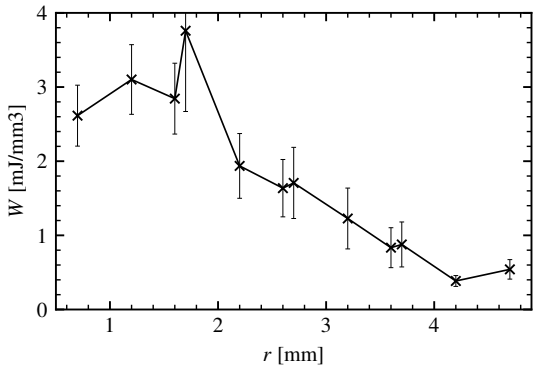

Figure 6.10: Radial variation of W_{max} for a compression at 33 N/mm.

the W_{max} field to an axisymmetric hypothesis. Nonetheless, the standard deviation is small compared to the mean and will give sufficient information on the softening for the energy balance analysis.

6.3.3 Energy balance analysis

The softening of the rubber leads to less stored energy in the envelope when inflated. The correct strain energy of the softened section is computed with the thick rubber tube inflation presented in section 1.4.1 with the [Ogden and Roxburgh, 1999] model.

Then, the energy balance analysis is applied to a pre-softened section of rubber and leads to the equation 6.1.

$$\delta W_{ext}(\lambda_z, \lambda_r, P_{int}) = \delta \tilde{E}(I_1, I_2, \eta) + \delta D \tag{6.1}$$

The softened stored energy $\delta \tilde{E}$ corresponds to the loading of a pre-softened section of rubber envelop. The relation between the virgin strain potential and the softened strain potential is given by :

$$\tilde{W}(I_1, I_2, \eta) = \eta W(I_1, I_2) + \phi(\eta) \tag{6.2}$$

Hence, the softened stored energy can be expressed from the strain energy density W and the energy density lost by the pre-loading ϕ, both varying along the radius r. The rest of the energy balance analysis then follow the classical approach.

$$\delta \tilde{E} = 2\pi \int_{r_{int}}^{r_{ext}} \tilde{W}(r) r \mathrm{d}r \delta a = 2\pi \int_{r_{int}}^{r_{ext}} \left[\eta(r) W(r) + \phi(\eta, r, \eta_{max})\right] r \mathrm{d}r \delta a \tag{6.3}$$

Applying the softening computed by the FE model gives the evolution of the SERR on a pre-softened sample in figure 6.11. For a similar G_C, the model predicts a lower critical pressure P_C to propagation on a softened sample, reproducing correctly the tendency observed during experiments.

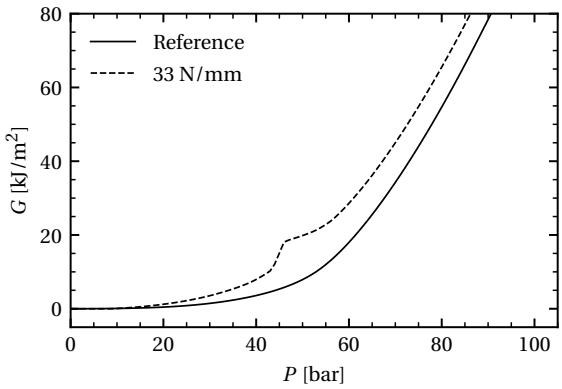

Figure 6.11: Variation of the strain energy release rate with inflation pressure for a reference and a softened condition.

6.4 Conclusion

A novel method is proposed to study the effect of pre-softening on the global strain energy release rate of an interface between an elastomeric matrix and a fiber reinforcement. The engineering implication of the presented results to elastomer fiber

reinforcement composites is a reduction of the adherence between components after an out-plane loading. For instance, [Valantin et al., 2015] reports a decrease of peel strength between rubber and polyamide reinforcement after a fatigue loading representative of a transmission belt application (out-of-plane loading of a rubber-polyamide fiber ply and bending). The sharp evolution between the virgin specimen (3.2 N/mm) and a specimen with 2 million cycles (2.8 N/mm) could be explained, based on the present study, solely by the rubber matrix softening.

After, this preliminary work evidence of pre-softening effect has been observed and qualitative agreement between experimental data and simple hybrid numerical / semi analytical model has been obtained. More samples will now be tested to consolidate the results. Higher compression forces will be applied to reach a strain energy level higher than during the RCAIT to test the modeling. The computation methods of the softening will be improved, with a finer geometry discretization and a numerical 3D tube inflation for comparison. As for most modeling of elastomer deformation with finite elements, mesh convergence proved to be difficult.

7 Slow crack effect

7.1 Experimental bench

A creep test bench was partially constructed during the previous thesis of [Kane, 2020] (RCAIT confinements, large hydraulic circuit, structure). Basically, during the creep test, a constant inflation pressure is obtained inside the RCAIT specimen by replacing the high pressure syringe and tensile testing machine with hydraulic accumulator. To complete the development of the system, additional valve and sensors were added for controlling and monitoring the experiment. A data acquisition system were also developed and installed to monitor the pressure and crack propagation in individual specimens. The setup consists of 9 parallel lines. Each line comprises a RCAIT, a hydraulic accumulator, a pressure sensor, and a camera (Fig. 7.1). A manually operated test pump (VIRAX® 262005 – 100 bar – 10 l) pressurizes the accumulators. The accumulators are each settled at different pressures.

Figure 7.1: Creep crack growth bench.

A LabView program developed for the bench records data during the test, with a

variable acquisition frequency per test line. The minimum frequency corresponds to the inverse of the number of active cameras. This limitation arises from the USB port multiplier to which the cameras are connected, acting as a multiplexer. The cameras are then used in photo mode rather than continuous video. However, considering the targeted solicitation times, the acquisition frequency limit poses no problem. The systems are independent, and the acquisition of an individual line stops automatically. Acquisition stops when the pressure drops below a certain threshold. Pressurized water escapes during total sample failure and then flows through the hoses to the test pump reservoir.

For now on, the ambient temperature follows day/night variations and is not controlled. A first improvement step will be the addition of heating around the RCAIT devices. A liquid for injection as neutral as possible (mineral or natural-based oil) can also be used.

7.2 First results

In figure 7.2, a first test campaign of subcritical slow rate crack propagation experiment is presented. A small incertitude at the end of the test is caused by the acquisition frequency. The time to the total fracture (propagation equal to 50 mm) of the specimen appears to increase with the decreased imposed inflation pressure. The pressure evolution appears non-linear and tends toward an asymptote.

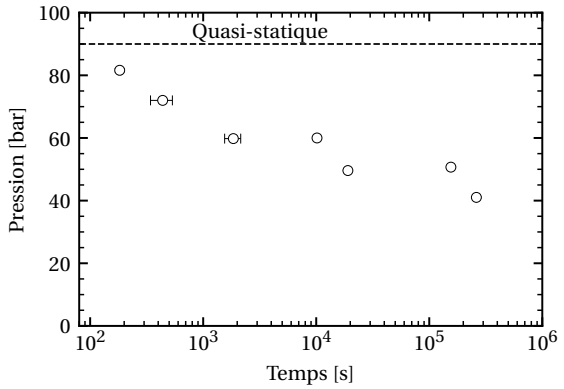

Figure 7.2: Time to final crack propagation (crack length = 50 mm) for a given imposed inflation pressure.

The analytical method gives the SERR for the corresponding pressure and the results are reported in Fig. 7.3. The crack velocity corresponds to the time to complete

fracture and the total adhesive length. The SERR increases with the crack velocity with a power law.

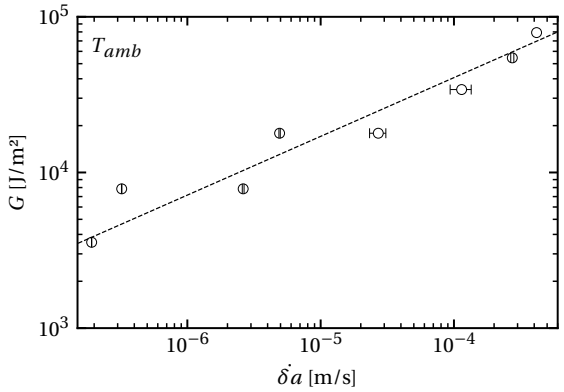

Figure 7.3: Strain energy release rate depending on crack velocity.

Conclusion

The present work improves and develops different methodologies around the RCAIT. The method to measure the global strain energy release rate is more robust with the improved metrology and the possible detrimental effect of confinement tube / specimen friction have been evaluated. The analytical hypothesis are evaluated and validated using a more complete finite element simulation procedure. The major dissipation source of an interface crack growth between a filled elastomer and rigid substrates is now possible to be evaluated with analytical and experimental developments. The interface loading conditions can be adjusted by applying combined axial loading and internal pressure loading conditions. Even if a precise evaluation of mode mixity conditions is difficult to achieve from experimental and theoretical point of view, a first failure envelope of G_C with the mode mixity is measured. The Mullins dissipation can be partially inhibited by a pre-softening procedure and the global dissipation during crack growth decrease. The relation between viscous dissipation and crack velocity can be evaluated with the creep fracture bench. G_C at low crack velocity is reported 10 times lower than during the quasi-static tests, revealing the role of viscous dissipation. The present work has a broader ambition than the rubber-cord industrial applications and try to contribute to the general field of the adherence of elastomer.

Perspectives of the RCAIT

The development of the marker tracking technique is not sufficient to characterize the process zone as discussed in chapter 3. A RCAIT conducted under a X-ray scan could give further information on the crack tip opening shape. Those information could confirm the numerical results of the blunted crack tip. Unlike the pure shear fracture test, the strain-stress field around the crack tip is not observable and the technique pro-

posed by [Roucou et al., 2020] does not apply to the RCAIT configuration. An experimental solution to this problem could be the addition of metallic tracers (steel or brass to ensure adhesion) in the rubber envelope coupled with an x-ray tomography observation during the RCAIT, giving the full strain tensor inside the envelope.

With the new improvements of the test and robust methodology, further studies can now focus on the application of RCAIT to ageing. Thanks to the use of a pressurized fluid to propagate the crack, a corrosive fluid could be introduced locally at the crack tip to evaluate a possible corrosion assisted crack growth, especially with the creep bench. Else, with a neutral injection fluid, the diffusion of water can be studied by submerging the sample in water (similarly to a water lubrication condition presented in chapter 4). The water will diffuse trough the rubber envelop to the interface in same time as the slow crack growth to estimate the coupling between diffusion and fracture. The system will provide a small-scale experiment, representative of the load and environment found in rubber-cord composites application.

Perspectives on the dissipations study

The method presented in chapter 6 uses an isotropic Mullins model [Ogden and Roxburgh, 1999] while diametrical compression can induce anisotropy in the $\vec{r}\vec{\theta}$ plane and RCAIT shows the strong rotation of the shear elongation λ_{rz} around the crack (see figure 3.14). Hence, the Mullins dissipation is not spent by the compression test and the Mullins dissipation by shear could remain available for dissipation during crack growth. Furthermore, the softening is supposed symmetric with the model of [Ogden and Roxburgh, 1999] while the softening appears only in tension in rubber [Machado et al., 2012]. Extending the steady-state crack growth model of [Qi et al., 2018] to an anisotropy-induced and asymmetric Mullins dissipation model could solve this open question. The successive rotation and compression of the sample to introduce softening is not ideal. The introduced softening field in the rubber envelope does not respect an axisymmetric distribution. An experimental device designed specifically for the application could alleviate this softening distribution issue. For instance, a system where the sample is compressed between three rolls (positioned at 120° from each other with their axis of revolution parallel to the specimen's cord) could apply the load on the sample and allow the sample rotation by rotating synchronously the 3 rolls. A second method could employ a torsion load (i.e. fixed cord and a rotation applied on

the outer surface of the envelope) to soften the rubber. Note that applying shear (i.e. pulling out the cord while blocking the outer surface of the envelope) will induce a non-homogenous softening along the cord axis[1]. Nonetheless, the successive compression method is sufficient to demonstrate the pre-softening effect on rubber adherence.

In the slow crack growth experiments in chapter 7, the decrease of G with the decrease of crack velocity is typical of visco-elastic crack growth [Hui et al., 2022]. On the Mullins dissipation, the time-scale of the experiment could involve a partial recovery of softening [Mullins, 1948, Denora and Marano, 2024]. Hence, treating the Mullins dissipation as a long-term viscosity corresponds with the visco-elastic framework, with at least two characteristic relaxation times. The experiments were carried out with pressurized deionized water and the inflation circuit is in stainless steel. This configuration could promote cathodic delamination [Liechti et al., 1989, Hamade et al., 2007]. An experimental solution to deconvoluate the visco-elastic variation of G and the possible corrosion-induced decrease of G would be to use a mineral oil as pressurized fluid. The oil will act as an insulator between the cord and the inflation circuit.

The role of Mullins dissipation recovery on creep crack growth could be evaluated by combining the pre-softening and the creep fracture. A sample should be pre-softened with the method described in chapter 6, then set under a constant G in the creep fracture bench presented in chapter 7. Then, the crack velocity should either stay constant (as a non-softened specimen) or vary. The variation will indicate a recovery of the dissipation spent during the pre-softening and characterize the recovery time scale in a single experiment. Furthermore combining the softening with the mixed-mode setup or modifying the creep bench for mixed-mode loading could provide further information on the dissipation mechanisms coupling.

Further work to separate the viscous and Mullins dissipation during crack growth should first build a behavior law more advanced than those used in the present study and second build a crack growth numerical model. The CZM proves to be computationally inefficient on the RCAIT. As mentioned in section 3.4.1, the crack propagation over 1 mm takes approximately 3 days on the computing cluster. The identified reason is the large deformation at the crack tip leading to elements with poor aspect ratio. This issue prevents the addition of dissipative behavior in the rubber constitutive law, a similar conclusion to the work of [Elzière, 2016] on visco-hyperelastic material

[1] As demonstrated by a shear lag model, the strain localizes at the crack tip between the cord and the envelope.

combined with CZM. A more efficient approach could be the steady-state crack growth framework [Dean and Hutchinson, 1980, Landis et al., 2000], recently used by [Fourton, 2019] for an adhesion case.

The total partition between dissipation, only with the proposed experiments, may not be possible because of the dependency of one on another. The multiplicative dependence of the global G on G_0 and G_D is a known result in the literature [Qi et al., 2018, de Gennes, 1996] for a single dissipation mechanism G_D outside the fracture dissipation G_0. In the case of two (or more) dissipation mechanisms, a possible multiplicative interdependence between a Mullins dissipation G_M and a viscous dissipation G_V could lead to a complex dependence between the global G and interfacial G_0.

Bibliography

[Akiba and Hashim, 1997] Akiba, M. and Hashim, A. S. (1997). Vulcanization and crosslinking in elastomers. *Progress in Polymer Science*, 22(3):475–521. Number: 3. (Cited on page 4)

[Alfano, 2006] Alfano, G. (2006). On the influence of the shape of the interface law on the application of cohesive-zone models. *Composites Science and Technology*, 66(6):723–730. Advances in statics and dynamics of delamination. (Cited on page 13)

[Anthony et al., 1942] Anthony, R. L., Caston, R. H., and Guth, E. (1942). Equations of state for natural and synthetic rubber-like materials. I. Unaccelerated natural soft rubber. *The Journal of Physical Chemistry*, 46(8):826–840. (Cited on page 5)

[ASTM D1781, 2012] ASTM D1781 (2012). Standard Test Method for Climbing Drum Peel for Adhesives. Issue: D1781-98. (Cited on pages 21, 34)

[ASTM D1871, 2014] ASTM D1871 (2014). Standard Test Method for Adhesion Between Tire Bead Wire and Rubber. Issue: D1871-04(2014). (Cited on pages 24, 34, 53)

[ASTM D1876, 2015] ASTM D1876 (2015). Standard Test Method for Peel Resistance of Adhesives (T-Peel Test). Issue: D1876-08(2015)e1. (Cited on page 21)

[ASTM D2229, 2014] ASTM D2229 (2014). Standard Test Method for Adhesion Between Steel Tire Cords and Rubber. Issue: D2229-10(2014). (Cited on pages 24, 34)

[ASTM D3330, 2018] ASTM D3330 (2018). Standard Test Method for Peel Adhesion of Pressure-Sensitive Tape. Issue: D3330M-04(2018). (Cited on pages 21, 22)

[ASTM D429, 2014] ASTM D429 (2014). Standard Test Methods for Rubber Property—Adhesion to Rigid Substrates. D429-14e1. (Cited on page 34)

[ASTM D4776, 2004] ASTM D4776 (2004). Standard Test Method for Adhesion of Tire Cords and Other Reinforcing Cords to Rubber Compounds by H-Test Procedure. Issue: D4776-04e1. (Cited on page 24)

[Barenblatt, 1962] Barenblatt, G. (1962). The mathematical theory of equilibrium cracks in brittle fracture. volume 7 of *Advances in Applied Mechanics*, pages 55–129. Elsevier. (Cited on page 13)

[Bartlett et al., 2023] Bartlett, M. D., Case, S. W., Kinloch, A. J., and Dillard, D. A. (2023). Peel tests for quantifying adhesion and toughness: A review. *Progress in Materials Science*, 137:101086. (Cited on pages 21, 22, 25, 26, 117, 120)

[Berry and Yang, 1996] Berry, D. T. and Yang, H. T. Y. (1996). Formulation and Experimental Verification of a Pneumatic Finite Element. *International Journal for Numerical Methods in Engineering*, 39(7):1097–1114. (Cited on page 64)

[Beter et al., 2020] Beter, J., Schrittesser, B., Meier, G., Fuchs, P. F., and Pinter, G. (2020). Influence of Fiber Orientation and Adhesion Properties On Tailored Fiber-reinforced Elastomers. *Appl Compos Mater*, 27(3):149–164. (Cited on page 100)

[Bonneric et al., 2019] Bonneric, M., Aubin, V., and Durville, D. (2019). Finite element simulation of a steel cable - rubber composite under bending loading: Influence of rubber penetration on the stress distribution in wires. *International Journal of Solids and Structures*, 160:158–167. (Cited on pages 100, 101)

[Bouasse and Carrière, 1903] Bouasse, H. and Carrière, Z. (1903). Sur les courbes de traction du caoutchouc vulcanisé. *Annales de la Faculté des sciences de l'Université de Toulouse pour les sciences mathématiques et les sciences physiques*, 5(3):257–283. Number: 3. (Cited on page 6)

[Brown, 2018] Brown, R. (2018). *Physical Test Methods for Elastomers*. Springer International Publishing. (Cited on page 78)

[Brown, 1996] Brown, R. P. (1996). *Adhesion, corrosion and staining*, pages 299–316. Springer Netherlands, Dordrecht. (Cited on page 53)

[Burlion et al., 2001] Burlion, N., Pijaudier-Cabot, G., and Dahan, N. (2001). Experimental analysis of compaction of concrete and mortar. *International Journal for Numerical and Analytical Methods in Geomechanics*, 25(15):1467–1486. (Cited on page 80)

[Cantournet et al., 2009] Cantournet, S., Desmorat, R., and Besson, J. (2009). Mullins effect and cyclic stress softening of filled elastomers by internal sliding and friction thermodynamics model. *International Journal of Solids and Structures*, 46(11):2255–2264. (Cited on page 11)

[Cao et al., 2016] Cao, Z., Tao, L., Akinwande, D., Huang, R., and Liechti, K. M. (2016). Mixed-mode traction-separation relations between graphene and copper by blister tests. *International Journal of Solids and Structures*, 84:147–159. (Cited on page 16)

[Chandra et al., 1996] Chandra, A. K., Mukhopadhyay, R., and Bhowmick, A. K. (1996). Studies of dynamic adhesion between steel cord and rubber using a new testing method. *Polymer Testing*, 15(1):13–34. Number: 1. (Cited on page 24)

[Chang and Peng, 1992] Chang, W. V. and Peng, S. H. (1992). Nonlinear elastic analysis of adhesive blister test. *Int J Fract*, 53(1):77–89. Number: 1. (Cited on page 26)

[Chang et al., 1989] Chang, Y.-S., Lai, Y.-H., and Dillard, D. A. (1989). The Constrained Blister—A Nearly Constant Strain Energy Release Rate Test for Adhesives. *The Journal of Adhesion*, 27(4):197–211. (Cited on pages 26, 34, 53, 78, 79)

[Chukwudozie et al., 2019] Chukwudozie, C., Bourdin, B., and Yoshioka, K. (2019). A variational phase-field model for hydraulic fracturing in porous media. *Computer Methods in Applied Mechanics and Engineering*, 347:957–982. (Cited on page 54)

[Clough et al., 2016] Clough, J. M., Creton, C., Craig, S. L., and Sijbesma, R. P. (2016). Covalent bond scission in the mullins effect of a filled elastomer: Real-time visualization with mechanoluminescence. *Advanced Functional Materials*, 26(48):9063–9074. (Cited on page 6)

[Cook et al., 1997] Cook, J. W., Edge, S., and Packham, D. E. (1997). The adhesion of natural rubber to steel and the use of the peel test to study its nature. *International Journal of Adhesion and Adhesives*, 17(4):333–337. Number: 4. (Cited on pages 15, 22, 23, 34, 118)

[Coran, 2003] Coran, A. Y. (2003). Chemistry of the vulcanization and protection of elastomers: A review of the achievements. *Journal of Applied Polymer Science*, 87(1):24–30. (Cited on pages 4, 5)

[Corbel and Jumel, 2023] Corbel, P.-Y. and Jumel, J. (2023). Simulation of fluid driven crack propagation along metal/elastomer interface - Application to the numerical analysis of the rubber cord adhesion inflation test. *Mechanics of Materials*, 185:104774. (Cited on pages 93, 97)

[Corbel et al., 2022] Corbel, P.-Y., Jumel, J., Kane, K., and Mbiakop-Ngassa, A. (2022). Refined crack propagation methodology and energy balance analysis in the Rubber Cord Adhesion Inflation Test. *International Journal of Adhesion and Adhesives*, 119:103243. (Cited on pages 53, 54, 58, 81, 82, 83, 88, 101, 104, 105, 108)

[Creton and Ciccotti, 2016] Creton, C. and Ciccotti, M. (2016). Fracture and adhesion of soft materials: A review. *Reports on progress in physics. Physical Society (Great Britain)*, 79:046601. (Cited on page 12)

[Crowther, 2001] Crowther, B. G. (2001). *Handbook of Rubber Bonding*. iSmithers Rapra Publishing. Google-Books-ID: 0TTdMT508PcC. (Cited on pages 7, 78, 80, 100)

[Dannenberg, 1975] Dannenberg, E. M. (1975). The Effects of Surface Chemical Interactions on the Properties of Filler-Reinforced Rubbers. *Rubber Chemistry and Technology*, 48(3):410–444. (Cited on pages 5, 6)

[Dannenberg, 1961] Dannenberg, H. (1961). Measurement of adhesion by a blister method. *Journal of Applied Polymer Science*, 5(14):125–134. (Cited on pages 26, 34, 35, 53, 79, 100, 120)

[de Gennes, 1979] de Gennes, P. G. (1979). *Scaling Concepts in Polymer Physics*. Cornell University Press. (Cited on page 5)

[de Gennes, 1996] de Gennes, P. G. (1996). Soft Adhesives. *Langmuir*, 12(19):4497–4500. Number: 19 Publisher: American Chemical Society. (Cited on pages 13, 14, 16, 137)

[Dean and Hutchinson, 1980] Dean, R. H. and Hutchinson, J. W. (1980). Quasi-Static Steady Crack Growth in Small-Scale Yielding. In *Fracture Mechanics*, pages 383–405. ASTM International. (Cited on page 137)

[Denora and Marano, 2024] Denora, I. and Marano, C. (2024). Stretch-induced softening in filled elastomers: A review on mullins effect related anisotropy and thermally induced recovery. *Polymer Testing*, 133:108399. (Cited on pages 6, 136)

[Devalba et al., 2018] Devalba, D. S., Thomas, A. G., and Busfield, J. J. C. (2018). Adhesive friction behavior of rough rubber surfaces sliding against smooth rigid surfaces. *Rubber Chemistry and Technology*, 91(3):621–632. (Cited on pages 79, 96)

[Diani et al., 2015] Diani, J., Brieu, M., Batzler, K., and Zerlauth, P. (2015). Effect of the Mullins softening on mode I fracture of carbon-black filled rubbers. *Int J Fract*, 194(1):11–18. Number: 1. (Cited on pages 11, 13, 120)

[Diani et al., 2009] Diani, J., Fayolle, B., and Gilormini, P. (2009). A review on the Mullins effect. *European Polymer Journal*, 45(3):601–612. Number: 3. (Cited on pages 6, 10, 14)

[Dong et al., 2023] Dong, H., Moyle, N., Wu, H., Khripin, C. Y., Hui, C.-Y., and Jagota, A. (2023). The transition from Elasto-Hydrodynamic to Mixed Regimes in Lubricated Friction of Soft Solid Surfaces. *Advanced Materials*, n/a(n/a):2211044. (Cited on pages 79, 97)

[Dorfmann and Ogden, 2004] Dorfmann, A. and Ogden, R. W. (2004). A constitutive model for the Mullins effect with permanent set in particle-reinforced rubber. *International Journal of Solids and Structures*, 41(7):1855–1878. Number: 7. (Cited on page 11)

[Dugdale, 1960] Dugdale, D. S. (1960). Yielding of steel sheets containing slits. *Journal of the Mechanics and Physics of Solids*, 8(2):100–104. Number: 2. (Cited on page 13)

[Ellul and Emerson, 1988] Ellul, M. D. and Emerson, R. J. (1988). A New Pull-Out Test for Tire Cord Adhesion—Part I. Hot Bonding. *Rubber Chemistry and Technology*, 61(2):293–308. (Cited on pages 24, 25, 53)

[Elzière, 2016] Elzière, P. (2016). *Laminated glass : dynamic rupture of adhesion*. phdthesis, Université Pierre et Marie Curie - Paris VI. (Cited on pages 16, 136)

[Fielding-Russell et al., 1979] Fielding-Russell, G. S., Nicholson, D. W., and Livingston, D. I. (1979). Physical Factors in Cord-to-Rubber Adhesion by a New Tire Cord Adhesion Test. *Tire Reinforcement and Tire Performance*. Publisher: ASTM International. (Cited on pages 24, 100)

[Fourton, 2019] Fourton, P. (2019). *Mécanismes de résistance à l'impact des vitrages feuilletés – effet des interfaces et de la rhéologie du polymère*. These de doctorat, Paris Sciences et Lettres (ComUE). (Cited on page 137)

[Fraser et al., 2021] Fraser, S., Barberio, C. G., Chaudhry, T., Power, D. M., Tan, S., Lawless, B. M., and Espino, D. M. (2021). The effect of injurious compression on the elastic, hyper-elastic and visco-elastic properties of porcine peripheral nerves. *Journal of the Mechanical Behavior of Biomedical Materials*, 121:104624. (Cited on page 121)

[Gabriel et al., 2016] Gabriel, D., Karbach, A., Drechsler, D., Gutmann, J., Graf, K., and Kheirandish, S. (2016). Bound rubber morphology and loss tangent properties of carbon-black-filled rubber compounds. *Colloid and Polymer Science*, 294. (Cited on page 5)

[Gasser et al., 2005] Gasser, T. C., Ogden, R. W., and Holzapfel, G. A. (2005). Hyperelastic modelling of arterial layers with distributed collagen fibre orientations. *Journal of The Royal Society Interface*, 3(6):15–35. Number: 6 Publisher: Royal Society. (Cited on page 79)

[Gent et al., 1981] Gent, A. N., Fielding-Russell, G. S., Livingston, D. I., and Nicholson, D. W. (1981). Failure of cord-rubber composites by pull-out or transverse fracture. *J Mater Sci*, 16(4):949–956. Number: 4. (Cited on pages 24, 25, 34, 79, 100)

[Gent and Hamed, 1977a] Gent, A. N. and Hamed, G. R. (1977a). Peel mechanics for an elastic-plastic adherend. *Journal of Applied Polymer Science*, 21(10):2817–2831. (Cited on page 22)

[Gent and Hamed, 1977b] Gent, A. N. and Hamed, G. R. (1977b). Peel mechanics of adhesive joints. *Polymer Engineering & Science*, 17(7):462–466. (Cited on page 22)

[Gent and Yeoh, 1982] Gent, A. N. and Yeoh, O. H. (1982). Failure loads for model adhesive joints subjected to tension, compression or torsion. *J Mater Sci*, 17(6):1713–1722. Number: 6. (Cited on pages 24, 53, 101, 120)

[Gilormini and Diani, 2015] Gilormini, P. and Diani, J. (2015). Testing some implementations of a cohesive-zone model at finite strain. *Engineering Fracture Mechanics*, 148:97–109. (Cited on pages 16, 61)

[Gong et al., 1999] Gong, J., Iwasaki, Y., Osada, Y., Kurihara, K., and Hamai, Y. (1999). Friction of Gels. 3. Friction on Solid Surfaces. *J. Phys. Chem. B*, 103(29):6001–6006. Number: 29 Publisher: American Chemical Society. (Cited on page 96)

[Graczykowski and Heinonen, 2007] Graczykowski, C. and Heinonen, J. (2007). Feasibility study of adaptive inflatable structures for protecting wind turbines. *Journal of Structural Mechanics*, 40(2):7–23. Number: 2. (Cited on page 64)

[Griffith and Taylor, 1921] Griffith, A. A. and Taylor, G. I. (1921). The phenomena of rupture and flow in solids. *Philosophical Transactions of the Royal Society of London. Series A, Containing Papers of a Mathematical or Physical Character*, 221(582-593):163–198. Number: 582-593 Publisher: Royal Society. (Cited on pages 11, 13)

[Hamade et al., 2007] Hamade, R. F., Seif, C. Y., and Dillard, D. A. (2007). Cathodic delamination of elastomer-to-metal adhesive joints: Experimental data and empirical modeling. *International Journal of Adhesion and Adhesives*, 27(2):108–121. Number: 2. (Cited on page 136)

[Heidenreich et al., 1968] Heidenreich, R. D., Hess, W. M., and Ban, L. L. (1968). A test object and criteria for high resolution electron microscopy. *Journal of Applied Crystallography*, 1(1):1–19. (Cited on page 5)

[Holzapfel, 2004] Holzapfel, G. (2004). Comparison of a Multi-Layer Structural Model for Arterial Walls With a Fung-Type Model, and Issues of Material Stability. *Journal of Biomechanical Engineering*, 126:264. (Cited on page 17)

[Holzapfel, 2000] Holzapfel, G. A. (2000). *Nonlinear solid mechanic*. Jhon Wiley and Sons Ltd. (Cited on page 8)

[Holzapfel et al., 2001] Holzapfel, G. A., Gasser, T. C., and Ogden, R. W. (2001). A new Constitutive Framework for Arterial Wall Mechanics and a Comparative Study of Material Models. In Cowin, S. C. and Humphrey, J. D., editors, *Cardiovascular Soft Tissue Mechanics*, pages 1–48. Springer Netherlands, Dordrecht. (Cited on pages 17, 18, 90, 107)

[Huang et al., 2023] Huang, J., Li, D., Peng, Z., Bo, Z., and Chen, S. (2023). A new method based on the shear lag model for accurate determination of ice adhesion shear strength on solid surface. *Science China Technological Sciences*, 66. (Cited on page 79)

[Hui et al., 2022] Hui, C.-Y., Zhu, B., and Long, R. (2022). Steady state crack growth in viscoelastic solids: A comparative study. *Journal of the Mechanics and Physics of Solids*, 159:104748. (Cited on pages 14, 136)

[James et al., 2020] James, J. D., Ludwick, J. M., Wheeler, M. L., and Oyen, M. L. (2020). Compressive failure of hydrogel spheres. *Journal of Materials Research*, 35(10):1227–1235. (Cited on page 120)

[Jamshidi et al., 2005] Jamshidi, M., Afshar, F., Mohammadi, N., and Pourmahdian, S. (2005). Study on cord/rubber interface at elevated temperatures by H-pull test method. *Applied Surface Science*, 249(1):208–215. Number: 1. (Cited on pages 24, 25)

[Jensen, 1991] Jensen, H. M. (1991). The blister test for interface toughness measurement. *Engineering Fracture Mechanics*, 40(3):475–486. Number: 3. (Cited on page 26)

[Jensen, 1998] Jensen, H. M. (1998). Analysis of mode mixity in blister tests. *International Journal of Fracture*, 94(1):79. Number: 1. (Cited on page 26)

[Jiang and Penn, 1992] Jiang, K. and Penn, L. (1992). Improved analysis and experimental evaluation of the single filament pull-out test. *Composites Science and Technology*, 45(2):89–103. (Cited on page 79)

[Jin and Arson, 2020] Jin, W. and Arson, C. (2020). Fluid-driven transition from damage to fracture in anisotropic porous media: a multi-scale xfem approach. *Acta Geotechnica*, 15:1–32. (Cited on page 54)

[Kane, 2020] Kane, K. (2020). *Durability of new metal/rubber assemblies*. phdthesis, Université de Bordeaux. (Cited on pages 1, 3, 26, 27, 29, 131)

[Kane et al., 2019] Kane, K., Jumel, J., Lallet, F., Mbiakop-Ngassa, A., Vacherand, J.-M., and Shanahan, M. (2019). A novel inflation adhesion test for elastomeric matrix /

steel cord. *International Journal of Solids and Structures*, 160:40–50. (Cited on pages 17, 29, 31, 34, 38, 40, 46, 53, 56, 70, 78, 79, 80, 101, 106, 120)

[Kane et al., 2020] Kane, K., Jumel, J., Lallet, F., Mbiakop-Ngassa, A., Vacherand, J.-M., and Shanahan, M. (2020). Experimental study of the rubber cord adhesion inflation test. *Engineering Fracture Mechanics*, 224:106783. (Cited on pages 31, 34, 38)

[Kane et al., 2021] Kane, K., Jumel, J., Mbiakop-Ngassa, A., Lallet, F., Vacherand, J.-M., and Shanahan, M. E. (2021). Rubber cord adhesion inflation test: Effect of constitutive rubber model on evaluation of G. *Engineering Fracture Mechanics*, 244:107547. (Cited on pages 10, 19, 29, 31, 34, 38, 48, 49, 54, 56, 69, 87, 109)

[Khajehsaeid et al., 2013] Khajehsaeid, H., Arghavani, J., and Naghdabadi, R. (2013). A hyperelastic constitutive model for rubber-like materials. *European Journal of Mechanics - A/Solids*, 38:144–151. (Cited on pages 10, 42, 58, 87, 108, 124, 126)

[Kim et al., 2019] Kim, S., Park, H., Moon, B., Sung, K., Koo, J.-M., and Seok, C.-S. (2019). The prediction methodology for tire's high speed durability regulation test using a finite element method. *International Journal of Fatigue*, 118:77–86. (Cited on page 4)

[Knauss, 1973] Knauss, W. G. (1973). *On the Steady Propagation of a Crack in a Viscoelastic Sheet: Experiments and Analysis*, pages 501–541. Springer US, Boston, MA. (Cited on pages 12, 13)

[Krishnan and Hui, 2009] Krishnan, V. R. and Hui, C. Y. (2009). Finite strain stress fields near the tip of an interface crack between a soft incompressible elastic material and a rigid substrate. *Eur. Phys. J. E*, 29(1):61–72. Number: 1. (Cited on pages 60, 115, 118)

[Kroon, 2011] Kroon, M. (2011). Steady-state crack growth in rubber-like solids. *Int J Fract*, 169(1):49–60. Number: 1. (Cited on page 14)

[Lake, 2003] Lake, G. J. (2003). Fracture Mechanics and its Application to Failure in Rubber Articles. *Rubber Chemistry and Technology*, 76(3):567–591. (Cited on page 53)

[Landis et al., 2000] Landis, C. M., Pardoen, T., and Hutchinson, J. W. (2000). Crack velocity dependent toughness in rate dependent materials. *Mechanics of Materials*, 32(11):663–678. Number: 11. (Cited on page 137)

[Lechtenboehmer et al., 1990] Lechtenboehmer, A., Moneypenny, H. G., and Mersch, F. (1990). A Review of Polymer Interfaces in Tyre Technology. *Brit. Poly. J.*, 22(4):265–301. Number: 4. (Cited on page 53)

[Lemaitre et al., 2020] Lemaitre, J., Chaboche, J.-L., Benallal, A., and Desmorat, R. (2020). *Mécanique des matériaux solides*. sciences sup physique. Dunod, Paris, 3e édition edition. (Cited on pages 8, 9, 13)

[Lengyel et al., 2014] Lengyel, T. H., Long, R., and Schiavone, P. (2014). Effect of interfacial slippage on the near-tip fields of an interface crack between a soft elastomer and a rigid substrate. *Proc. R. Soc. A.*, 470(2170). Number: 2170. (Cited on page 60)

[Liechti et al., 1989] Liechti, K. M., Becker, E., Lin, C., and Miller, T. (1989). A fracture analysis of cathodic delamination in rubber to metal bonds. *International Journal of Fracture*, 39:217–234. (Cited on pages 15, 136)

[Liechti and Wu, 2001] Liechti, K. M. and Wu, J.-D. (2001). Mixed-mode, time-dependent rubber/metal debonding. *Journal of the Mechanics and Physics of Solids*, 49(5):1039–1072. Number: 5. (Cited on pages 15, 16, 59, 60, 62, 113)

[Long and Hui, 2016] Long, R. and Hui, C.-Y. (2016). Fracture toughness of hydrogels: measurement and interpretation. *Soft Matter*, 12:8069–8086. (Cited on page 14)

[Luo et al., 2023] Luo, G., Guo, J., Zhang, C., and Yang, X. (2023). Life prediction of cord/rubber laminates under multiaxial fatigue. *International Journal of Fatigue*, 174:107733. (Cited on page 100)

[Machado et al., 2012] Machado, G., Chagnon, G., and Favier, D. (2012). Induced anisotropy by the Mullins effect in filled silicone rubber. *Mechanics of Materials*, 50:70–80. (Cited on pages 6, 11, 135)

[Machado et al., 2014] Machado, G., Chagnon, G., and Favier, D. (2014). Theory and identification of a constitutive model of induced anisotropy by the Mullins effect. *Journal of the Mechanics and Physics of Solids*, 63:29–39. (Cited on page 11)

[Mai et al., 2021] Mai, T.-T., Okuno, K., Tsunoda, K., and Urayama, K. (2021). Anisotropic stress-softening effect on fast dynamic crack in filler-reinforced elastomers. *Mechanics of Materials*, 155:103786. (Cited on page 13)

[Marckmann and Verron, 2006] Marckmann, G. and Verron, E. (2006). Comparison of Hyperelastic Models for Rubber-Like Materials. *Rubber Chemistry and Technology*, 79:835–858. (Cited on page 9)

[Meng and Chang, 2020] Meng, Q. and Chang, M. (2020). Interfacial crack propagation between a rigid fiber and a hyperelastic elastomer: Experiments and modeling. *International Journal of Solids and Structures*, 188-189:141–154. (Cited on pages 16, 24, 25, 60, 62, 100)

[Meyer and Ferri, 1935] Meyer, K. H. and Ferri, C. (1935). Sur l'élasticité du caoutchouc. *Helvetica Chimica Acta*, 18(1):570–589. (Cited on page 5)

[Mills et al., 2009] Mills, N. J., Stämpfli, R., Marone, F., and Brühwiler, P. A. (2009). Finite element micromechanics model of impact compression of closed-cell polymer foams. *International Journal of Solids and Structures*, 46(3):677–697. Number: 3. (Cited on page 64)

[Mukherjee et al., 2016] Mukherjee, B., Dillard, D. A., Moore, R. B., and Batra, R. C. (2016). Debonding of confined elastomeric layer using cohesive zone model. *International Journal of Adhesion and Adhesives*, 66:114–127. (Cited on pages 16, 60, 62)

[Mullins, 1948] Mullins, L. (1948). Effect of Stretching on the Properties of Rubber. *Rubber Chemistry and Technology*, 21(2):281–300. Number: 2. (Cited on pages 6, 136)

[Mullins, 1969] Mullins, L. (1969). Softening of Rubber by Deformation. *Rubber Chemistry and Technology*, 42(1):339–362. Number: 1. (Cited on page 76)

[Neggers et al., 2015] Neggers, J., Hoefnagels, J. P. M., van der Sluis, O., Sedaghat, O., and Geers, M. G. D. (2015). Analysis of the dissipative mechanisms in metal–elastomer interfaces. *Engineering Fracture Mechanics*, 149:412–424. (Cited on pages 15, 16, 22, 59)

[Nicholson et al., 1978] Nicholson, D. W., Livingston, D. I., and Fielding-Russell, G. S. (1978). A New Tire Cord Adhesion Test. *Tire Science and Technology*, 6(2):114–124. Number: 2 Publisher: Allen Press. (Cited on pages 53, 78, 100)

[Ogden and Roxburgh, 1999] Ogden, R. W. and Roxburgh, D. G. (1999). A pseudo–elastic model for the Mullins effect in filled rubber. *Proc. R. Soc. Lond. A*, 455(1988):2861–2877. Number: 1988. (Cited on pages 10, 11, 14, 124, 126, 128, 135)

[Ozawa and Mase, 2016] Ozawa, K. and Mase, K. (2016). Evidence for chemical bond formation at rubber–brass interface: Photoelectron spectroscopy study of bonding interaction between copper sulfide and model molecules of natural rubber. *Surface Science*, 654:14–19. (Cited on page 7)

[Pandey et al., 2020] Pandey, V., Fleury, A., Villey, R., Creton, C., and Ciccotti, M. (2020). Linking peel and tack performances of pressure sensitive adhesives. *Soft Matter*, 16:3267–3275. (Cited on page 16)

[Patil et al., 2014] Patil, A., Nordmark, A., and Eriksson, A. (2014). Free and constrained inflation of a pre-stretched cylindrical membrane. *Proceedings of the Royal Society A: Mathematical, Physical and Engineering Sciences*, 470(2169):20140282. (Cited on page 79)

[Paul et al., 2018] Paul, B., Faivre, M., Massin, P., Giot, R., Colombo, D., Golfier, F., and Martin, A. (2018). 3D coupled HM–XFEM modeling with cohesive zone model and applications to non planar hydraulic fracture propagation and multiple hydraulic fractures interference. *Computer Methods in Applied Mechanics and Engineering*, 342:321–353. (Cited on page 54)

[Persson et al., 2005] Persson, B., Albohr, O., Heinrich, G., and Ueba, H. (2005). Crack propagation in rubber-like materials. *Journal of Physics: Condensed Matter*, 17:R1071. (Cited on page 12)

[Pupurs and Varna, 2017] Pupurs, A. and Varna, J. (2017). Steady-state energy release rate for fiber/matrix interface debond growth in unidirectional composites. *International Journal of Damage Mechanics*, 26(4):560–587. (Cited on pages 101, 106)

[Qi et al., 2018] Qi, Y., Caillard, J., and Long, R. (2018). Fracture toughness of soft materials with rate-independent hysteresis. *Journal of the Mechanics and Physics of Solids*, 118:341–364. (Cited on pages 10, 11, 13, 14, 120, 135, 137)

[Qi et al., 2024] Qi, Y., Li, X., Venkata, S. P., Yang, X., Sun, T. L., Hui, C.-Y., Gong, J. P., and Long, R. (2024). Mapping deformation and dissipation during fracture of soft viscoelastic solid. *Journal of the Mechanics and Physics of Solids*, 186:105595. (Cited on page 12)

[Rao et al., 2004] Rao, S., Daniel, I. M., and Gdoutos, E. E. (2004). Mechanical Properties and Failure Behavior of Cord/Rubber Composites. *Applied Composite Materials*, 11(6):353–375. Number: 6. (Cited on page 100)

[Rey et al., 2014] Rey, T., Razan, F., Robin, E., Faure, S., Le Cam, J. B., Chagnon, G., Girard, A., and Favier, D. (2014). Mechanical characterization and comparison of different NiTi/silicone rubber interfaces. *International Journal of Adhesion and Adhesives*, 48:67–74. (Cited on page 24)

[Rivlin and Rideal, 1948] Rivlin, R. S. and Rideal, E. K. (1948). Large elastic deformations of isotropic materials iv. further developments of the general theory. *Philosophical Transactions of the Royal Society of London. Series A, Mathematical and Physical Sciences*, 241(835):379–397. (Cited on page 9)

[Rivlin and Thomas, 1953] Rivlin, R. S. and Thomas, A. G. (1953). Rupture of rubber. I. Characteristic energy for tearing. *Journal of Polymer Science*, 10(3):291–318. (Cited on pages 12, 22)

[Roucou, 2020] Roucou, D. (2020). *Caractérisation et modélisation du comportement à la déchirure de matériaux élastomères endommagés par chargements multiaxiaux*. These de doctorat, Centrale Lille Institut. (Cited on page 13)

[Roucou et al., 2020] Roucou, D., Diani, J., Brieu, M., and Colombo, D. (2020). Experimental identification of fracture toughness of a carbon black-filled styrene butadiene rubber undergoing energy dissipation by Mullins softening. *Mechanics of Materials*, 151:103645. (Cited on pages 13, 135)

[Rumpel and Schweizerhof, 2004] Rumpel, T. and Schweizerhof, K. (2004). Hydrostatic Fluid Loading in Non-Linear Finite Element Analysis. *International Journal for Numerical Methods in Engineering*, 59:849–870. (Cited on page 64)

[Sarkar and Bhowmick, 2018] Sarkar, P. and Bhowmick, A. K. (2018). Sustainable rubbers and rubber additives. *Journal of Applied Polymer Science*, 135(24):45701. (Cited on pages 4, 53)

[Sauer, 2011] Sauer, R. A. (2011). The Peeling Behavior of Thin Films with Finite Bending Stiffness and the Implications on Gecko Adhesion. *The Journal of Adhesion*, 87(7-8):624–643. (Cited on page 22)

[Schmidt et al., 2010] Schmidt, T., André, M., and Poll, G. (2010). A transient 2D-finite-element approach for the simulation of mixed lubrication effects of reciprocating hydraulic rod seals. *Tribology International*, 43(10):1775–1785. Number: 10. (Cited on page 97)

[Schulze-Bauer et al., 2002] Schulze-Bauer, C. A. J., Regitnig, P., and Holzapfel, G. A. (2002). Mechanics of the human femoral adventitia including the high-pressure response. *American Journal of Physiology-Heart and Circulatory Physiology*, 282(6):H2427–H2440. Number: 6 Publisher: American Physiological Society. (Cited on page 17)

[Shima et al., 1993] Shima, S., Tatara, Y., Iio, M., Shu, C., and Lucero, J. (1993). Large deformations of a rubber sphere under diametral compression : Part 2 : Experiments on many rubber materials and comparisons of theories with experiments. *JSME international journal. Ser. A, Mechanics and material engineering*, 36:197–205. (Cited on page 120)

[Skala, 1970] Skala, D. P. (1970). Modified Equations of Rubber Elasticity Applied to the Inflation Mechanics of a Thick-Walled Rubber Cylinder. *Rubber Chemistry and Technology*, 43(4):745–757. Number: 4. (Cited on pages 17, 19, 29, 40, 86, 107)

[Slootman et al., 2020] Slootman, J., Waltz, V., Yeh, C. J., Baumann, C., Göstl, R., Comtet, J., and Creton, C. (2020). Quantifying Rate- and Temperature-Dependent Molecular Damage in Elastomer Fracture. *Phys. Rev. X*, 10(4):041045. Number: 4 Publisher: American Physical Society. (Cited on page 13)

[Su et al., 2021] Su, B., Liu, S., Zhang, P., Wu, J., and Wang, Y. (2021). Mechanical properties and failure mechanism of overlap structure for cord-rubber composite. *Composite Structures*, 274:114350. (Cited on page 100)

[Takenaka, 2012] Takenaka, M. (2012). Analysis of structures of rubber-filler systems with combined scattering methods. *Polymer Journal*, 45. (Cited on pages 5, 6)

[Talamini et al., 2018] Talamini, B., Mao, Y., and Anand, L. (2018). Progressive damage and rupture in polymers. *Journal of the Mechanics and Physics of Solids*, 111:434–457. (Cited on page 13)

[Torggler et al., 2023] Torggler, J., Dutzler, A., Oberdorfer, B., Faethe, T., Müller, H., Buzzi, C., and Leitner, M. (2023). Investigating Damage Mechanisms in Cord-Rubber Composite Air Spring Bellows of Rail Vehicles and Representative Specimen Design. *Appl Compos Mater*, 30(6):1979–1999. Number: 6. (Cited on pages 3, 4)

[Toulemonde et al., 2018] Toulemonde, P.-A., Diani, J., Gilormini, P., Desgardin, N., and Nevière, R. (2018). Propellant cohesive fracture during the peel test of a propellant/liner structure. *The Journal of Adhesion*, 94(8):657–666. Number: 8. (Cited on page 22)

[Treloar, 1975] Treloar, L. (1975). *The physics of rubber elasticity*. Oxford Classic Texts in the Physical Sciences. (Cited on pages 4, 5)

[Treloar, 1943] Treloar, L. R. G. (1943). The elasticity of a network of long-chain molecules—ii. *Trans. Faraday Soc.*, 39:241–246. (Cited on page 10)

[Tuononen, 2016] Tuononen, A. J. (2016). Onset of frictional sliding of rubber–glass contact under dry and lubricated conditions. *Sci Rep*, 6(1):27951. (Cited on pages 79, 96)

[Valantin, 2014] Valantin, C. (2014). *Compréhension des mécanismes d'endommagement de l'interface textile-caoutchouc*. PhD thesis, INSA Centre Val de Loire. (Cited on page 3)

[Valantin et al., 2015] Valantin, C., Lacroix, F., Deffarges, M.-P., Morcel, J., and Aït Hocine, N. (2015). Interfacial damage on fatigue-loaded textile–rubber composites. *Journal of Applied Polymer Science*, 132(4). (Cited on page 130)

[van den Bosch et al., 2008] van den Bosch, M., Schreurs, P., Geers, M., and van Maris, M. (2008). Interfacial characterization of pre-strained polymer coated steel by a numerical–experimental approach. *Mechanics of Materials*, 40(4):302–317. (Cited on page 16)

[van der Walt et al., 2014] van der Walt, S., Schönberger, J. L., Nunez-Iglesias, J., Boulogne, F., Warner, J. D., Yager, N., Gouillart, E., Yu, T., and the scikit-image con-

tributors (2014). scikit-image: image processing in Python. *PeerJ*, 2:e453. (Cited on page 39)

[van Ooij, 1977] van Ooij, W. J. (1977). The role of XPS in the study and understanding of rubber-to-metal bonding. *Surface Science*, 68:1–9. (Cited on pages 38, 53)

[van Ooij, 1979] van Ooij, W. J. (1979). Fundamental Aspects of Rubber Adhesion to Brass-Plated Steel Tire Cords. *Rubber Chemistry and Technology*, 52(3):605–675. Number: 3. (Cited on pages 80, 102)

[van Ooij, 1984] van Ooij, W. J. (1984). Mechanism and Theories of Rubber Adhesion to Steel Tire Cords—An Overview. *Rubber Chemistry and Technology*, 57(3):421–456. Number: 3. (Cited on pages 7, 8, 80, 102)

[van Ooij et al., 2009] van Ooij, W. J., Harakuni, P. B., and Buytaert, G. (2009). Adhesion of Steel Tire Cord to Rubber. *Rubber Chemistry and Technology*, 82(3):315–339. Number: 3. (Cited on pages 7, 80)

[Vilgis et al., 2009] Vilgis, T. A., Heinrich, G., and Klüppel, M. (2009). *Reinforcement of Polymer Nano-Composites: Theory, Experiments and Applications*. Cambridge University Press, Cambridge. (Cited on pages 4, 5)

[Williams, 1997] Williams, J. (1997). Energy Release Rates for the Peeling of Flexible Membranes and the Analysis of Blister Tests. *International Journal of Fracture*, 87(3):265–288. Number: 3. (Cited on pages 26, 34, 35)

[Wu et al., 2021] Wu, H., Jagota, A., and Hui, C.-Y. (2021). Lubricated Sliding of a Rigid Cylinder on a Viscoelastic Half Space. *Tribol Lett*, 70(1):1. Number: 1. (Cited on page 96)

[Xiang et al., 2022] Xiang, F., Schneider, K., Schwartzkopf, M., and Heinrich, G. (2022). Competition between strain-induced crystallization and cavitation at the crack tip of unfilled and carbon black-filled natural rubber. *Macromolecules*, 55:10682–10693. (Cited on page 13)

[Xu et al., 2013] Xu, F., ichi Yoshimura, K., and Mizuta, H. (2013). Experimental study on friction properties of rubber material: Influence of surface roughness on sliding friction. *Procedia Engineering*, 68:19–23. (Cited on page 96)

[Yang et al., 2020] Yang, T., Liechti, K. M., and Huang, R. (2020). A multiscale cohesive zone model for rate-dependent fracture of interfaces. *Journal of the Mechanics and Physics of Solids*, 145:104142. (Cited on page 16)

[Zhang et al., 2015] Zhang, T., Lin, S., Yuk, H., and Zhao, X. (2015). Predicting fracture energies and crack-tip fields of soft tough materials. *Extreme Mechanics Letters*, 4:1–8. (Cited on page 14)

[Zhao et al., 2019] Zhao, B., Zhang, B., and Zhang, K. (2019). Modelling three-dimensional soft elastohydrodynamic lubrication contact of heterogeneous materials. *Tribology International*, 129:377–389. (Cited on page 97)

[Öngün et al., 2008] Öngün, Y., André, M., Bartel, D., and Deters, L. (2008). An axisymmetric hydrodynamic interface element for finite-element computations of mixed lubrication in rubber seals. *Proceedings of the Institution of Mechanical Engineers, Part J: Journal of Engineering Tribology*, 222(3):471–481. Number: 3. (Cited on page 97)

COLLEGES SCIENCES
BRETAGNE POUR L'INGENIEUR
LOIRE ET LE NUMERIQUE

ENSTA BRETAGNE

Titre : Rupture d'interface rigide-élastomère sous chargement complexe

Mots clés : Pneu, Caoutchouc, Mécanique de la rupture, Adhesion

Résumé : Les élastomères armés de fibres textiles ou de fils métalliques se retrouvent dans de nombreuses applications industrielles (pneus, courroies d'entraînement, bandes de convoyage, tuyaux, ressorts pneumatiques). L'adhésion du renfort à la matrice élastomère doit être assurée pour garantir l'intégrité structurelle du produit sous divers chargements mécaniques. Une caractérisation fiable de la résistance à la fissuration de l'interface est donc nécessaire, ce qui motive le développement de nouveaux essais mécaniques. Dans un premier temps, un dispositif expérimental de fissuration entre un fil métallique et un caoutchouc naturel chargé de noir de carbone est utilisé pour caractériser la dissipation d'énergie lors de la rupture interfaciale. L'essai, issu d'une précédente thèse, est tout d'abord amélioré et la méthodologie expérimentale consolidée. Des modélisations analytiques et numériques permettent de valider la cinématique de l'essai, les conditions expérimentales de lubrification et le calcul de l'énergie d'adhésion. Dans un second temps, l'essai est décliné selon trois méthodes permettant de caractériser l'adhésion du renfort à la matrice sous d'autres chargements. Ainsi, il apparaît que la mixité du chargement en pointe de fissure, la vitesse de propagation ou la pré-accommodation du caoutchouc influent sur l'énergie globale dissipée pendant la rupture de l'interface. Ces nouvelles méthodes offrent alors une caractérisation de l'adhésion dans des conditions plus proche des applications industrielles.

Title : Failure of rigid-elastomer interface under complex loading

Keywords : Tyre, Rubber, Fracture mechanic, Adhesion

Abstract : Elastomers reinforced by textile fibers or metallic wires are common in numerous industrial applications (tires, driving belts, conveying belts, and pneumatic springs). The adhesion between the reinforcement and the elastomer matrix must be ensured to guarantee the structural integrity of the product under various mechanical loads. A reliable characterization of the crack propagation resistance of the interface is thus necessary, motivating the development of new mechanical tests. Firstly, an experimental setup of crack propagation between a metal wire and a natural black carbon rubber is used to charactérize the dissipated energy during the interfacial fracture. The test, developed from a precedent thesis, is first improved and the experimental methodology is updated. Analytical and numerical models allow the validation of the test kinematics, experimental conditions of lubrication, and the computation of the adhesion energy. Secondly, the test is derived using three methods, permitting the characterization of the adhesion between the reinforcement and the matrix under other loadings. Hence, the crack mode mixity, the crack propagation velocity, or the matrix pre-softening alters the global dissipation during the interface fracture. Those new methods offer an adhesion characterization in closer conditions to the industrial applications.